

DISSERTATION IN ASTRONOMY

SUBMITTED TO THE

COMBINED FACULTIES OF THE NATURAL SCIENCES AND MATHEMATICS

OF THE RUPERTO-CAROLA-UNIVERSITY OF HEIDELBERG, GERMANY

FOR THE DEGREE OF

DOCTOR OF NATURAL SCIENCES

PUT FORWARD BY

CAMILLA PENZO, M.Sc.

BORN IN PONTE DELL'OLIO, PC, ITALY

ORAL EXAMINATION: 7 JULY 2015



---

# Galaxy and Structure Formation in Dynamical and Coupled Dark Energy

Camilla Penzo

Max-Planck-Institut für Astronomie

---

Referees: Dr. Andrea V. Macciò  
Prof. Dr. Björn M. Schäfer



# Galaxy and Structure Formation in Dynamical and Coupled Dark Energy

## Abstract:

In this thesis I study the effects of different Dark Energy models on galaxy formation via numerical simulations. I investigate systems around and below Milky-Way masses and describe the effects of dark energy at galactic and sub-galactic scales. Firstly, I analyze high-resolution hydrodynamical simulations of three disc galaxies in dynamical dark energy models. While overall stellar feedback remains the driving mechanisms in shaping galaxies, the effect of the dark energy parametrization plays a larger role than previously thought. Secondly, I broaden the galaxy sample by simulating a 80 Mpc/h side cube of our universe using the same dynamical dark energy models. I show that resolution is a crucial ingredient so that baryonic feedback mechanisms can enhance differences between cosmological models. Thirdly, I investigate the effects of dynamical dark energy on dwarf mass scales. I find that there is more variation from object to object (due to the stochasticity of star formation at these scales) than between the same object in different cosmological models, which makes it hard for observations to disentangle different dark energy scenarios. In the second part of this thesis I investigate the effects of coupled dark energy models on galactic and sub-galactic scales via dark matter only high-resolution simulations. I find that coupled models decrease concentrations of (Milky-Way-like) parent haloes and also reduce the number of subhaloes orbiting around them. This improves the agreement with observations and, hence, makes these cosmologies attractive alternatives to a cosmological constant.

## Galaxienentstehung und Strukturbildung in dynamischen und gekoppelten Dunkle Energiemodellen

### Abstract:

In meiner Arbeit untersuche ich die Effekte verschiedener Modelle für die Dunkle Energie auf die Galaxienentstehung mit Hilfe numerischer Simulationen. Ich untersuche Systeme mit Massen ähnlich oder kleiner der der Milchstraße und beschreibe die Auswirkungen der Dunklen Energie auf galaktischen und subgalaktischen Skalen. Zunächst untersuche ich hochauflösende hydrodynamische Simulationen von drei Scheibengalaxien in dynamischen Dunklen Energiemodellen. Während die thermische und kinetische Rückkopplung von Sternen bei der Gestaltung der Galaxien weiterhin eine dominante Rolle spielt, wirkt sich die Parametrisierung der Dunklen Energie stärker aus als bisher angenommen. Als nächstes erweitere ich die Galaxienprobe durch Simulation der gleichen dynamischen Dunklen Energiemodelle in einem Würfel mit 80 Mpc/h Seitenlänge. Dabei zeige ich, dass die Auflösung ein entscheidender Faktor für die baryonischen Rückkopplung ist und dass sie die Unterschiede zwischen kosmologischen Modellen sichtbar machen kann. Drittens habe ich die Auswirkungen von dynamischer Dunkler Energie auf Zwerggalaxien untersucht. In diesen Skalen erzeugt die stochastische Sternentstehung eine solch große Varianz von einem Objekt zum nächsten, dass die Unterschiede zwischen verschiedenen kosmologischen Modellen nicht sichtbar sind. In Beobachtungen ist es also schwer, zwischen verschiedenen Dunklen Energieszenarien zu unterscheiden. Im zweiten Teil dieser Arbeit benutze ich hochauflösende Simulationen mit reiner Dunkler Materie, um den Einfluss von gekoppelter Dunkler Energie auf galaktischen und subgalaktischen Skalen zu untersuchen. Die gekoppelten Modelle verringern die Konzentration von - milchstraßenähnlichen - Halos und reduzieren die Anzahl der Satellitenhalos. Dadurch verbessert sich die Übereinstimmung mit Beobachtungen, was diese Kosmologien zu attraktiven Alternativen gegenüber jenen mit einer kosmologischen Konstante macht.

# Contents

<b>Introduction</b>	<b>13</b>
<b>1 Cosmological Models</b>	<b>15</b>
1.1 Cosmological Assumptions and Equations . . . . .	15
1.2 An Expanding universe and the Cosmological Constant . . . . .	16
1.3 The $\Lambda$ CDM Model . . . . .	17
1.3.1 Baryons . . . . .	18
1.3.2 Radiation . . . . .	19
1.3.3 Dark Matter . . . . .	20
1.3.4 Problems of a Cosmological Constant . . . . .	20
1.4 Dark Energy . . . . .	21
1.4.1 Dynamical Dark Energy . . . . .	21
1.4.2 Coupled Dark Energy . . . . .	23
<b>2 Galaxy Formation and Evolution</b>	<b>27</b>
2.1 Linear Structure Formation . . . . .	27
2.1.1 Remarks on Linear Evolution and Dark Energy . . . . .	29
2.2 Non-Linear Structure Formation . . . . .	32
2.2.1 Spherical Collapse . . . . .	32
2.2.2 Press-Schechter Mass Function . . . . .	33
2.2.3 The Zel'dovich Approximation . . . . .	34
2.3 N-Body Simulations of the Large-Scale Structure of the universe	34
2.3.1 Particle-Particle Method . . . . .	35
2.3.2 Particle-Mesh Method . . . . .	36
2.3.3 Tree Algorithms . . . . .	36
2.3.4 Halo mass Function . . . . .	36
2.3.5 Radial Density Profiles . . . . .	37
2.4 Hydrodynamical Processes in Galaxy Formation . . . . .	37
2.4.1 Accreting Gas and Cooling Process . . . . .	38
2.4.2 Star Formation and Feedback Mechanisms . . . . .	39
2.5 Hydrodynamics . . . . .	40
2.5.1 SPH Method . . . . .	40

<b>3</b>	<b>Numerical Methods</b>	<b>43</b>
3.1	Generating Initial Conditions . . . . .	43
3.1.1	GRAFIC2-DE . . . . .	44
3.2	N-body and SPH Solvers . . . . .	45
3.2.1	GASOLINE-DE . . . . .	45
3.2.2	GADGET2-CDE . . . . .	47
<b>4</b>	<b>Galaxy Formation in Dynamical Dark Energy</b>	<b>51</b>
4.1	Models . . . . .	51
4.2	Disc Galaxies simulations in Dynamical Dark Energy . . . . .	53
4.2.1	Introduction . . . . .	53
4.2.2	Results and Discussion . . . . .	55
4.2.3	Conclusions on Disc Galaxies simulations in Dynamical Dark Energy . . . . .	67
4.3	Hydrodynamical Cosmological Volumes in Dynamical Dark Energy . . . . .	68
4.3.1	Introduction . . . . .	68
4.3.2	Numerical and Cosmological Settings . . . . .	69
4.3.3	Results and Discussion . . . . .	70
4.3.4	Conclusions on Hydrodynamical Cosmological Volumes in Dynamical Dark Energy . . . . .	77
4.4	Dwarf Galaxies Simulations in Dynamical Dark Energy and $\Lambda$ CDM . . . . .	78
4.4.1	Introduction . . . . .	78
4.4.2	Results and Discussion . . . . .	80
4.4.3	Remarks . . . . .	83
4.4.4	$\Lambda$ CDM Follow-Up . . . . .	83
4.4.5	Conclusions on Dwarf Galaxies Simulations in Dynamical Dark Energy and $\Lambda$ CDM . . . . .	86
<b>5</b>	<b>Halo and Subhalo properties in Coupled Dark energy</b>	<b>89</b>
5.1	Details on the Cosmological Models . . . . .	91
5.2	Numerical Set-Up . . . . .	91
5.3	Results on Milky-Way size Halo simulations . . . . .	95
5.3.1	Host Halos Properties . . . . .	95
5.3.2	Subhalos . . . . .	100
5.4	Zooming-in on a dwarf halo . . . . .	105
5.5	Conclusions . . . . .	108
<b>6</b>	<b>Summary and Conclusions</b>	<b>111</b>
	<b>Bibliography</b>	<b>119</b>

# List of Figures

1.1	CMB temperature map from Planck Collaboration et al. (2015).	19
2.1	Examples of power spectra in dynamical dark energy models and $\Lambda$ CDM.	30
2.2	Dark matter large-scale structure from Springel et al. (2006).	35
3.1	Example of mesh refinement.	45
3.2	Fiducial galaxy and its rotation curves when varying feedback recipes from Stinson et al. (2013b).	47
3.3	Dark matter large scale structure in $\Lambda$ CDM and two coupled dark energy models from Baldi (2012b).	49
4.1	Our choices for dynamical dark energy models plotted over the $2\sigma$ contours from WMAP7.	52
4.2	Evolution of $H(a)$ and $D_+(a)$ .	53
4.3	Dark matter density profiles of $\text{gal}\alpha$ in all five cosmological models in a dark matter only and hydrodynamical simulation.	56
4.4	Galaxy sample in the stellar-halo mass plane.	57
4.5	Evolutions of the stellar-halo mass relation.	58
4.6	Evolution of the dark matter and gas mass.	59
4.7	Star formation histories.	59
4.8	Ratios of $\text{SFR}/\text{SFR}_\Lambda$ .	60
4.9	Rotation curves.	61
4.10	Comparison rotation curves in dark matter only and hydrodynamical simulations.	62
4.11	Evolution of the mean metallicity in “bulge”, “disc” and “halo”.	63
4.12	Evolution of cool gas in “bulge”, “disc” and “halo”.	65
4.13	Feedback–Dark Energy degeneracy: evolution of stellar-halo mass relation.	66
4.14	Ratios of the halo mass functions with $\Lambda$ CDM for the LR volume.	71
4.15	Ratios of the halo mass functions with $\Lambda$ CDM for the HR volume.	71

4.16	Ratios of the stellar mass functions with $\Lambda$ CDM for the LR volume. . . . .	72
4.17	Ratios of the stellar mass functions with $\Lambda$ CDM for the HR volume. . . . .	73
4.18	Ratio of the mean stellar mass to $\Lambda$ CDM as function of halo mass for the LR volume. . . . .	74
4.19	Ratio of the mean stellar mass to $\Lambda$ CDM as function of halo mass for the HR volume. . . . .	74
4.20	Ratio of the mean stellar mass to $\Lambda$ CDM as function of redshift for the single-galaxy simulations. . . . .	75
4.21	Evolution of the stellar-halo mass relation for $\text{gal}\beta$ and stellar mass functions for the HR volume. . . . .	76
4.22	Evolutions of $w \equiv p/\rho$ for our choices of dynamical dark energy models and for the early dark energy models used in Fontanot et al. (2012). . . . .	77
4.23	Stellar-halo mass relation for our dwarf galaxies in dynamical dark energy models. . . . .	81
4.24	SFRs for our dwarf sample. . . . .	82
4.25	Stellar-halo mass relation for our 22 dwarf galaxies in $\Lambda$ CDM cosmology. . . . .	84
4.26	Star Formation Rates (SFR) of the 15 dwarf galaxies that succeeded in forming stars in our $\Lambda$ CDM sample. . . . .	85
4.27	SFRs and density profiles for four dwarf galaxies from our sample with comparable masses. . . . .	86
4.28	Dark matter mass evolution within 2 and 4 kpc from the center for three dwarf galaxies from our sample with comparable masses. . . . .	87
4.29	Dark matter density and gas temperature maps for one of the two dwarf galaxies in the sub-sample experiencing a major merger. . . . .	87
5.1	$D_+$ and mass functions of the chosen coupled dark energy models. . . . .	92
5.2	Density maps for all simulated halos. . . . .	94
5.3	Parent halos density profiles. . . . .	95
5.4	Parent halos rotation curves. . . . .	97
5.5	Evolution of the NFW scale radius. . . . .	97
5.6	Parent halos accretion histories. . . . .	98
5.7	Fit to the accretion history of $\text{halo}\beta$ . . . . .	99
5.8	Cumulative number of subhalos as function of their mass. . . . .	100
5.9	Cumulative number of subhalos as function of distance from the parent halo. . . . .	101
5.10	Differential number of subhalos as function of distance from the parent halo. . . . .	102

5.11 Differential number of subhalos within  $3R_{200}$  of the parent halo. 103  
5.12 Rotation curves of subhalos. . . . . 106  
5.13 Density maps of dwarf halos. . . . . 107  
5.14 Profiles and rotation curves for dwarf halos. . . . . 107  
5.15 Accretion histories for dwarf halos. . . . . 108



# Introduction

Since the first Type Ia Supernova data were published (Riess et al., 1998; Perlmutter et al., 1999), it has been clear that our universe is expanding with a positive acceleration. On one hand, this led to a general acceptance of a Cosmological Constant as the repulsive force driving the expansion of our universe, on the other, it triggered the search for alternative theories leading to Modified Gravity and to Dark Energy.

Nowadays numerous cosmological models that depart from the standard paradigm have been proposed, many of those triggered by the long-discussed problems of coincidence and fine-tuning (Wetterich, 1988). Whether or not these problems are illdefined, some alternative theories can be as viable as the standard paradigm, and they need to be tested against observational constraints, at and beyond linear level.

Given the wide spectrum of observational data that is available, our most powerful approach to constrain a given cosmological model is to broaden the scales at which we test the model with data. Comparisons to observations on cosmologically large scales need to be complementary to those on the highly non-linear end of the power spectrum, down to galactic and sub-galactic scales. At such small scales models that depart from the standard  $\Lambda$ CDM paradigm are, at the time being, scarcely investigated.

To make predictions at highly non-linear scales we need to employ high resolution numerical simulations. Additionally, the effects of baryonic feedback processes are known to strongly affect galactic and sub-galactic scales and, for this, they ought to be taken into account. Nevertheless, modeling hydrodynamical processes is a very challenging task and understanding their role in shaping differences among cosmologies is crucial to make use of the very high resolution data coming from the next generation of galaxy surveys.

My work concentrates on exploring structure formation at galactic and sub-galactic scales in two of the most popular alternatives to the  $\Lambda$ CDM model, dynamical dark energy and coupled dark energy, and is organized as follows. In Chapter 1 I outline the basic features of the standard cosmological model to then describe the models behind dynamical dark energy and coupled dark energy. In Chapter 2 I describe the basis of the theory of structure formation at linear and non-linear level. In Chapter 3 I explain the numerical methods that will be used throughout this thesis. In Chapter 4

I show our results on galaxy formation in dynamical dark energy. We start with single-object hydrodynamical simulations of disc galaxies, to then extend the project to hydrodynamical simulations of a cosmological volume of the universe; I end the Chapter by describing our work in exploring smaller scales with hydrodynamical simulations of dwarf galaxies. In Chapter 5 I outline our study on halo formation and evolution in coupled dark energy. We performed single-object high dark matter only simulations of Milky Way haloes and a dwarf halo, and we study the effects on the coupling between dark matter and dark energy on halo concentration and number of subhaloes. Finally, in Chapter 6 I summarize our work and draw conclusions.

# Chapter 1

## Cosmological Models

### 1.1 Cosmological Assumptions and Equations

Einstein's theory of gravitation and its cosmological implications ([Einstein, 1917](#)) represent the guiding principles for modern theoretical cosmology. In the theory of General Relativity the geometry of the space-time is included in the *metric tensor*  $g_{\mu\nu}$ , while the matter content of the universe is expressed by the *energy-momentum tensor*  $T_{\mu\nu}$  and they are related by Einstein's field equations

$$G_{\mu\nu} \equiv R_{\mu\nu} - \frac{1}{2}g_{\mu\nu}R = \frac{8\pi G}{c^4}T_{\mu\nu}, \quad (1.1)$$

where  $G$  is Newton's gravitational constant,  $c$  is the speed of light in vacuum,  $G_{\mu\nu}$  is the Einstein tensor,  $R$  and  $R_{\mu\nu}$  are the Ricci scalar and Ricci tensor and are defined as follows:

$$R = g^{\mu\nu}R_{\mu\nu}, \quad (1.2)$$

$$R_{\mu\nu} = \frac{\partial\Gamma_{\mu\nu}^{\lambda}}{\partial x^{\lambda}} - \frac{\partial\Gamma_{\mu\lambda}^{\nu}}{\partial x^{\nu}} + \Gamma_{\mu\nu}^{\lambda}\Gamma_{\lambda\delta}^{\delta} - \Gamma_{\mu\lambda}^{\delta}\Gamma_{\nu\delta}^{\lambda}, \quad (1.3)$$

where

$$\Gamma_{\mu\nu}^{\lambda} = \frac{1}{2}g^{\lambda\tau}(g_{\tau\mu,\nu} + g_{\tau\nu,\mu} - g_{\mu\mu,\tau}), \quad (1.4)$$

are the *Christoffel symbols* (see e.g. [Landau and Lifshitz 1976](#); [Riotta 2010](#)).

There exists no general solutions to Eq. (1.1), thus Einstein and others realized that, in order to apply the field equations to the description of the universe, simplifying assumptions were needed. Firstly, space was assumed to be spatially homogeneous and isotropic on sufficiently large scales (Cosmological Principle), which meant that our universe should look the same at each point and in all directions. From only geometric considerations, the most generic space-time metric for a homogeneous and isotropic universe

---

takes the following form and is referred to as Friedman-Lemaître-Robertson-Walker metric (Friedmann, 1922; Lemaître, 1927; Robertson, 1935):

$$ds^2 = -c^2 dt^2 + a(t)^2 \left[ \frac{dr^2}{1 - kr^2} + r^2(d\theta^2 + \sin^2 \theta d\phi^2) \right], \quad (1.5)$$

where  $t$  is physical time,  $r$ ,  $\theta$  and  $\phi$  are the co-moving spherical coordinates,  $a(t)$  is the scale factor which describes the expansion or contraction of the universe and  $k$  represents the spacial curvature, which is  $k = 0$  in the case of a flat universe,  $k = \pm 1$  for a positive or negative curvature.

Secondly, the various matter-energy components are assumed to be well described by a continuous fluid, to which spacial comoving coordinates are assigned. When assuming a perfect fluid, the energy-momentum tensor becomes

$$T_{\mu\nu} = (p + \rho c^2)u_\mu u_\nu - pg_{\mu\nu}, \quad (1.6)$$

where  $p$  is the pressure,  $\rho c^2$  is the energy density and  $u_\mu$  is the fluid four-velocity.

Inserting the FLRW metric of Eq. (1.5) into Einstein's field equations, Eq. (1.1), gives non-null identities only in the cases of the time-time and space-space components, which respectively are:

$$\frac{\ddot{a}}{a} = -\frac{4\pi G}{3} \left( \rho + 3\frac{p}{c^2} \right), \quad (1.7)$$

$$a\ddot{a} + 2\dot{a}^2 + 2kc^2 = 4\pi G \left( \rho - \frac{p}{c^2} \right) a^2, \quad (1.8)$$

which lead to

$$\dot{a}^2 + kc^2 = \frac{8\pi G}{3} \rho a^2. \quad (1.9)$$

Eq. (1.7) and Eq. (1.9) are commonly known as *Friedmann equations*.

## 1.2 An Expanding universe and the Cosmological Constant

The theory of General Relativity was given form at the beginning of the 1900s and at that time the scientific community thought to be certain about living in a static universe. Einstein realized that only a fluid with negative density or negative pressure would allow a static solution, in fact, from Eq. (1.9),  $\ddot{a} > 0$  if  $w < 1/3$ . Such fluid did not seem a reasonable assumption to make, so the simplest way out of the problem was to introduce a constant term in the field equations, the Cosmological Constant  $\Lambda$ . Eq. (1.1) then became

$$R_{\mu\nu} - \frac{1}{2}g_{\mu\nu}R - \Lambda g_{\mu\nu} = \frac{8\pi G}{c^4}T_{\mu\nu}. \quad (1.10)$$

Around the same years, observational astronomy was making huge steps forward. Larger telescopes were built and this allowed to increase the precision on spectra measurements. In 1929, Hubble discovered a number of objects that not only were distant and not part of the Milky Way, but were also moving away from us. Furthermore, he discovered that their receding speed was proportional to their distance (Hubble, 1929), which is today known as *Hubble Law*:

$$v = H_0 d, \quad (1.11)$$

where  $v$  and  $d$  are the receding velocity and the distance of the object and  $H_0$  is the Hubble constant.

Consequently to the discovery of the expansion of the universe, there was no more need to force the theory to predict a static solution, and the motivation behind the cosmological constant dropped. On the contrary of what Einstein believed, the interest around the cosmological constant did not drop as well. In fact  $\Lambda$  was reintroduced to justify the *accelerated* expansion of our universe and has been one of the most active research topics since then.

### 1.3 The $\Lambda$ CDM Model

Nowadays the most widely accepted description for our universe is given by the Lambda Cold Dark Matter ( $\Lambda$ CDM) model. It describes a *flat* universe composed of baryonic and dark matter, radiation and a cosmological constant, and it is in astonishing agreement with observational constraints (Tegmark et al., 2006; Jones et al., 2009; Alam et al., 2015).

The evolution of the  $i$ -th component is often described by the density parameter  $\Omega_i \equiv \rho_i/\rho_{\text{crit}}$ , where  $\rho_{\text{crit}} = 3H^2/(8\pi G)$  is the critical density and  $H \equiv \dot{a}/a$  the Hubble function. As a consequence, Eq. (1.9) can be rewritten as:

$$H(a)^2 = H_0^2 [\Omega_b(a) + \Omega_{\text{DM}}(a) + \Omega_{\text{rad}}(a) + \Omega_\Lambda(a)], \quad (1.12)$$

where the various  $\Omega$ 's stand for baryons, dark matter, radiation and cosmological constant contributions and a flat universe has been assumed (see e.g. Coles and Lucchin 2002 for details). The behavior of the components of the universe as functions of the scale factor determine the evolutionary history of the universe and depend on their specific equations of state, i.e.  $p = w\rho c^2$ , with  $0 \leq w \leq 1$ .

**Dust:** The case  $w = 0$  represents dust, or pressureless matter, i.e. the typical thermal pressure of particles is much less than their rest mass, which is a good approximation for a non-relativistic fluid. Both baryonic and dark matter belong to this case.

**Radiative fluid:** a fluid composed of non-degenerate, relativistic particles in thermal equilibrium has  $w = 1/3$ . Photons obey to this equation of state.

---

**Cosmological Constant:** By definition, it has a constant density  $\rho_\Lambda$ , with equation of state  $w = -1$

The adiabatic expansion of the universe, can be written as

$$\dot{\rho} + 3 \left( \rho + \frac{p}{c^2} \right) \frac{\dot{a}}{a} = 0, \quad (1.13)$$

which is known as *continuity equation*. Using the equations of state for respectively for baryonic and dark matter, radiation and cosmological constant,  $w = 0, 1/3, -1$ , we obtain the scaling of density with the expansion factor:

$$\rho_b a^3 = \rho_{b_0} a_0^3, \quad \rho_{DM} a^3 = \rho_{DM_0} a_0^3, \quad \rho_{rad} a^4 = \rho_{rad_0} a_0^4, \quad \rho_\Lambda = \text{const}. \quad (1.14)$$

With today's scale factor  $a_0 = 1$ , we can then rewrite Eq. (1.12) as

$$H(a)^2 = H_0^2 [\Omega_{b_0} a^{-3} + \Omega_{DM_0} a^{-3} + \Omega_{rad_0} a^{-4} + \Omega_\Lambda]. \quad (1.15)$$

From Eq. (1.15), it is clear that the expansion rate of the universe is determined by the energy density and the equation of state of its constituents and that, in order to determine the expansion history, we must measure the values of the cosmological parameters today and the Hubble constant. The most recent values for these quantities are ([Planck Collaboration et al., 2015](#)):

$$H_0 = 67.8 \text{ km/s/Mpc}, \quad (1.16)$$

$$\Omega_{b_0} = 0.0490, \quad (1.17)$$

$$\Omega_{DM_0} = 0.2685, \quad (1.18)$$

$$\Omega_{rad_0} = 8.5 \times 10^{-5}, \quad (1.19)$$

$$\Omega_\Lambda = 0.6824. \quad (1.20)$$

### 1.3.1 Baryons

One of the puzzling questions that astronomers were trying to answer in the first decades of the XX century was why our universe is mainly composed of only hydrogen and helium and what produced the remaining heavier elements. In the 1940s, astronomers were debating whether heavier elements could come directly from the synthesized primordial hydrogen. [Gamow \(1946\)](#) and [Alpher et al. \(1948\)](#) suggested that the universe in the past was much hotter and denser, but they showed that the amount of heavier elements present today could not come from what was then referred to as Big Bang Nucleosynthesis (BBN) alone. Today we know that they indeed come from star cores and supernovae explosions. From BBN we can have accurate estimates of the amount of baryons present in the universe, which today accounts for about 5% of the total energy content.

### 1.3.2 Radiation

After having accepted that there must have been an epoch where the universe was extremely hot and dense, [Alpher and Herman \(1948\)](#) realized that the expansion of the universe had to be accounted for. Furthermore, they realized that in such conditions the universe had to be dominated by radiation which was in thermal equilibrium with matter. While the universe was expanding it was also cooling down, which led to a decrease in the temperature until protons and electrons could recombine to form atoms. After what we refer to as “recombination”, photons stopped interacting with atoms, maintained their temperature and freely propagated through the universe. Thus, Alpher and collaborators predicted the existence of an isotropic thermal radiation background that propagated till today and they estimated its temperature to be around a few degrees Kelvin. The discovery of the relic radiation was firstly made by Penzias and Wilson ([Penzias and Wilson, 1965](#)) and then confirmed by [Roll and Wilkinson \(1966\)](#). They had found a constant, isotropic, unpolarized excess in temperature with a black body spectrum, what was then called Cosmic Microwave Background (CMB) radiation, which convinced the community of the validity of the Big Bang Theory. Today we know that there also exists a relic radiation of neutrinos, which are nearly as numerous as CMB photons and were highly relativistic in the early universe. Finally, also stars emit radiation, but compared to photons and neutrinos, radiation from stars is completely negligible. [Fig. 1.1](#) shows the latest CMB temperature map from [Planck Collaboration et al. \(2015\)](#).

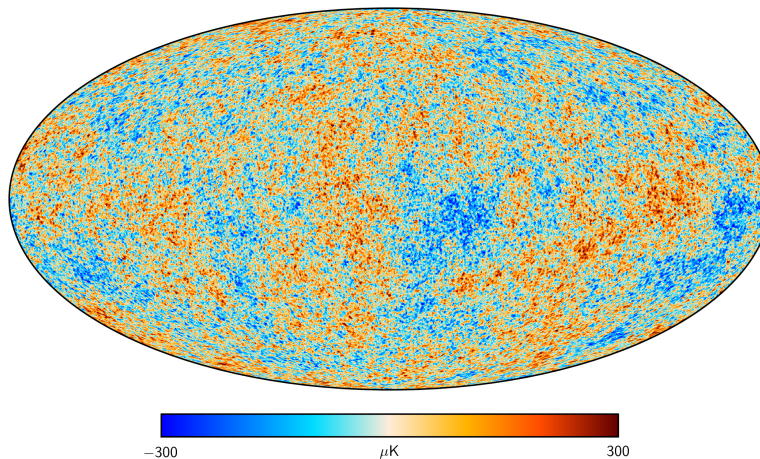


Figure 1.1: CMB temperature anisotropies from [Planck Collaboration et al. \(2015\)](#).

---

### 1.3.3 Dark Matter

For many years it was believed that the total matter in galaxies was nothing more than what can be seen, until Zwicky realized that there must have been some “missing” mass in Coma Cluster. Visible matter was rotating way faster than it ever could have been if the total mass accounted for was only stars and gas. He estimated that there had to be 400 times more mass than what we could see (Zwicky, 1933). Rubin et al. (1980) showed that NGC3115 rotation curve (i.e. rotational velocity as a function of the distance from the galactic center) did not have the expected Keplerian  $\sqrt{d}$  fall, but instead appeared to be constant to large radii. The only explanation was that the luminous mass was not all the mass that there was to account for, but instead in the outskirts there had to be some *dark mass*. Today we know that dark matter seems to interact only gravitationally and, despite the fact that it accounts for more than 20% of the energy content of the universe, no dark matter particle has yet been detected.

### 1.3.4 Problems of a Cosmological Constant

Even long before the introduction of the cosmological constant, particle physicists realized that vacuum energy should be an underlying background energy that must exist throughout space. Once  $\Lambda$  was re-introduced to explain the late-time accelerated expansion of the universe, the most straightforward explanation was to associate the cosmological constant with the vacuum energy density. By summing up the zero-point energy contributions, the estimate for the vacuum energy density is (see e.g. Amendola and Tsujikawa, 2010):

$$\rho_{\text{vac}} = 10^{74} \text{GeV}^4, \quad (1.21)$$

where natural units are used ( $\hbar = c = 1$ ). On the other hand, the observed value for the cosmological constant energy density is:

$$\rho_{\Lambda} = 10^{-47} \text{GeV}^4. \quad (1.22)$$

On top of this, Amendola and Tsujikawa point out that if there were such a vacuum energy density in the past, this would have triggered an eternal state of cosmic acceleration, which in turn would of course not agree with the existence of a radiation dominated nor with a matter dominated era, both being big successes of the  $\Lambda$ CDM paradigm. The inconsistency between the theoretical  $\rho_{\text{vac}}$  and the observationally measured  $\rho_{\Lambda}$  gave rise to *fine-tuning* objections on the cosmological constant.

As showed in Eq. (1.14), matter density is proportional to the cubic of the scale factor, while the energy density of the cosmological constant is constant by definition. After the universe was coming out of its matter dominated era, the contribution of the cosmological constant started taking over. This happened around redshift  $z \sim 1$ , which compared to the entire history of

the universe, could appear to be suspiciously close to today. The fact that we happen to live right about when the epoch of cosmic acceleration started has been referred to as the *coincidence problem*.

Whether these two discussed issues are truly a problem for the introduction of a cosmological constant in the model or not, in the last decades they have surely motivated cosmologists to come up with alternative theories to explain the late-time accelerated expansion.

## 1.4 Dark Energy

A cosmological constant does provide an explanation for the late-time accelerated expansion, but it is far from being the only possible explanation. Also motivated by the fundamental problems in assuming the existence of a cosmological constant, in the last decades cosmologists came up with alternative theories. In this work we will only summarize two of the many models available in literature, dynamical dark energy and coupled dark energy. For clarity, we will assume  $c = 1$ .

### 1.4.1 Dynamical Dark Energy

From Eq. (1.9), it can be concluded that in order to give rise to the cosmic acceleration a fluid with equation of state that satisfies  $w_{\text{DE}} < -1/3$  (assuming a positive density) needs to be introduced. By integrating the continuity equation (1.13), one obtains the general evolution of the dark energy density as function of redshift:

$$\rho_{\text{DE}}(z) = \rho_{\text{DE}}(0) \exp \left[ \int_0^z \frac{3[1 + w_{\text{DE}}(\tilde{z})]}{1 + \tilde{z}} d\tilde{z} \right], \quad (1.23)$$

where we have made use of  $H = \dot{a}/a$  and  $z = 1/a - 1$ . Eq. (1.23) gives in turn the evolution for the density parameter  $\Omega_{\text{DE}}(z)$  which then enters in the Friedmann equation (1.15). Unlike the constant  $w = -1$  equation of state for the cosmological constant, in the case of dynamical dark energy (or quintessence) the equation of state dynamically changes with time. To do so, a scalar field  $\phi$  with a self-interacting potential  $V(\phi)$  is introduced. The scalar field only interacts through gravity, thus the standard Lagrangian becomes

$$\mathcal{L} = \frac{1}{16\pi G} R - \frac{1}{2} g^{\mu\nu} \partial_\mu \phi \partial_\nu \phi - V(\phi) + \mathcal{L}_{\text{m+r}}, \quad (1.24)$$

where  $R$  is the Ricci scalar and  $\mathcal{L}_{\text{m+r}}$  is the lagrangian for the matter and radiation components. The energy-momentum tensor for the scalar field is

$$T_{\mu\nu}^{(\phi)} = - \frac{2}{\sqrt{-g}} \frac{\delta[-\frac{1}{2}\sqrt{-g}g^{\mu\nu}\partial_\mu\phi\partial_\nu\phi - \sqrt{-g}V(\phi)]}{\delta g^{\mu\nu}} \quad (1.25)$$

$$= \partial_\mu \phi \partial_\nu \phi - g_{\mu\nu} \left[ \frac{1}{2} g^{\alpha\beta} \partial_\alpha \phi \partial_\beta \phi - V(\phi) \right], \quad (1.26)$$

---

where  $g \equiv \det(g^{\mu\nu})$ . Using a FLRW metric, we can find pressure and energy density of the scalar field to obtain its equation of state parameter

$$w_\phi \equiv \frac{p_\phi}{\rho_\phi} = \frac{\frac{1}{2}\dot{\phi}^2 - V(\phi)}{\frac{1}{2}\dot{\phi}^2 + V(\phi)}. \quad (1.27)$$

We then can rewrite Friedmann equations as

$$H^2 = \frac{8\pi G}{3} \left[ \frac{1}{2}\dot{\phi}^2 + V(\phi) + \rho_m + \rho_{\text{rad}} \right], \quad (1.28)$$

$$\dot{H} = -\frac{8\pi G}{2} \left( \dot{\phi}^2 + \rho_m + \rho_{\text{rad}} + p_m + p_{\text{rad}} \right). \quad (1.29)$$

Furthermore, the variation of the action with respect to the scalar field holds an extra equation compared to the  $\Lambda$ CDM case

$$\ddot{\phi} + 3H\dot{\phi} + V' = 0, \quad (1.30)$$

where  $V' \equiv dV/d\phi$ . The scalar field needs to satisfy the condition  $w_\phi < -1/3$ . Thus, from Eq. (1.27) we obtain that  $\dot{\phi}^2 < V(\phi)$ , which means that the potential needs to be flat enough so that the scalar field can slowly move along the potential. Additionally, under the condition  $H^2 \ll V''$ , the kinetic term becomes negligible compared to the potential and the dark energy behavior approaches the false vacuum (i.e.  $w = -1$ ).

The behavior of such field strongly depends on the form of the potential. In the following we list some of the most popular choices that can be found in literature:

- a.  $V(\phi) = \frac{M^{4+\alpha}}{\phi^n}$ , with  $\alpha > 0$  (Ratra and Peebles, 1988)
- b.  $V(\phi) = M^4 e^{-\lambda\phi}$ , with  $\lambda > 0$  (Ferreira and Joyce, 1998; Ratra and Peebles, 1988)
- c.  $V(\phi) = \frac{M^{4+\alpha}}{\phi^n} e^{4\pi G\phi^2}$ , with  $\alpha > 0$  (Brax and Martin, 1999)
- d.  $V(\phi) = V_0 + M^{4-\alpha}\phi^\alpha$ , with  $\alpha > 0$  (Linde, 1987)

In this work we will only focus on a potential of the (c) form, called SUGRA (SUper GRAvity) potential. And more details on the specifics used will be given in Section 4.1.

The interesting feature of adopting a scalar field with a potential to describe dark energy is that they can exhibit *tracking solutions*. These are trajectories in the phase space that “attract” other trajectories and ensure that, independently of the chosen initial conditions for the field, the behavior is going to converge towards  $w_{\text{DE}} \simeq -1$  today. With this feature, a dynamical scalar field responsible dark energy has been claimed to improve the fine-tuning behind the introduction of a cosmological constant.

## Parametrization

The model for quintessence that we have briefly outlined is completely self-consistent, one can start from the Lagrangian for a specific field and work out the guiding equations for its linear evolution. Leaving aside the theoretical model, being of course the only physical motivated route towards a complete theory, what affects structure formation is the evolution of the linear background, given that the field for dark energy does not cluster or interacts with any component other than gravity. For this reason, often parametrizations of the background quantities are used (e.g.  $w \equiv p/\rho$ ), not accounting for the physically complete model that may stand behind. In this work we will use the so-called CPL parametrization (Chevallier and Polarski 2001 and Linder 2003),

$$w(a) \equiv w_0 + (1 - a)w_a, \quad (1.31)$$

with  $a$  scale factor and  $w_0$  and  $w_a$  constant values.

To be noted that the parametrization becomes necessary when trying to use the observed luminosity distance  $d_L(z)$  to infer  $H(z)$ , and therefore obtain  $w(z)$  (Amendola and Tsujikawa, 2010). In the case of dark energy, the reconstruction of the scalar field potential is also possible. The luminosity distance is defined as

$$d_L \equiv \left( \frac{L}{4\pi F} \right)^{\frac{1}{2}}, \quad (1.32)$$

where  $L$  is the source absolute luminosity and  $F$  is its observed flux. Furthermore,

$$d_L = \frac{c(1+z)}{H_0} \sinh \left( H_0 \int_0^z \frac{d\tilde{z}}{H(\tilde{z})} \right). \quad (1.33)$$

Given that we have measurements of the luminosity distance only at discrete redshifts values. The direct differentiation of  $d_L$  with respect to the redshift is not possible unless a parametrization is used. Different authors have chosen to parametrize either  $d_L(z)$ ,  $H(z)$  or  $w_{DE}(z)$ .

### 1.4.2 Coupled Dark Energy

The *coincidence problem* is one of the puzzling points of the  $\Lambda$ CDM model (see Section 1.3.4). On the other hand, by introducing an interaction between dark matter and dark energy (Amendola, 2000), the fact that their contributions are of the same order round about today would not come as a surprise. Indeed, the background evolution of constant coupling models is characterized by a regime during matter domination where the two interacting fluids share a constant ratio of the total energy content of the universe. This regime is fueled by the energy transfer from the dark matter particles to the dark energy scalar field. The fact that dark matter and dark energy density evolutions are strongly coupled in turn alleviates the *coincidence* problem (Mangano et al., 2003; Matarrese et al., 2003).

---

The Lagrangian is the following (Amendola, 2000),

$$\mathcal{L} = \frac{1}{16\pi G}R - \frac{1}{2}\partial^\mu\partial_\mu\phi - V(\phi) - m(\phi)\bar{\psi}\psi + \mathcal{L}_{kin}[\psi] + \mathcal{L}_{\text{bar+rad}} \quad (1.34)$$

where the mass  $m(\phi)$  of the dark matter field  $\psi$  is a function of the dark energy scalar field  $\phi$ , which has a potential  $V(\phi)$ ,  $\mathcal{L}_{kin}[\psi]$  accounts for possible terms describing the dark matter Lagrangian and  $\mathcal{L}_{\text{bar+rad}}$  groups the terms describing baryons and radiation. The dark energy model is as described in the previous Section, i.e. a dynamical scalar field  $\phi$  rolling down its potential  $V(\phi)$ , thus its energy density and pressure are

$$\rho_\phi = \frac{1}{2}g^{\mu\nu}\partial_\mu\phi\partial_\nu\phi + V(\phi), \quad (1.35)$$

$$p_\phi = \frac{1}{2}g^{\mu\nu}\partial_\mu\phi\partial_\nu\phi - V(\phi). \quad (1.36)$$

The interaction appears as a source term in the conservation equations for the single species

$$\nabla_\mu T_\nu^{\mu(\phi)} = +Q(\phi)T^{(\text{DM})}\nabla_\nu\phi, \quad (1.37)$$

$$\nabla_\mu T_\nu^{\mu(\text{DM})} = -Q(\phi)T^{(\text{DM})}\nabla_\nu\phi, \quad (1.38)$$

$$\nabla_\mu T_\nu^{\mu(\text{bar})} = 0, \quad (1.39)$$

$$\nabla_\mu T_\nu^{\mu(\text{rad})} = 0. \quad (1.40)$$

where  $T_\nu^\mu$  is the energy-stress tensor,  $Q$  is a function of  $\phi$  and represents the coupling strength and  $T$  is the trace of  $T_\nu^\mu$ . In this way, the conservation of the total stress-energy tensor is not violated. When assuming a FLRW metric, the continuity equations become

$$\ddot{\phi} + 3H\dot{\phi} + V' = +Q(\phi)\rho_{\text{DM}}, \quad (1.41)$$

$$\dot{\rho}_{\text{DM}} + 3H\rho_{\text{DM}} = -Q(\phi)\rho_{\text{DM}}\dot{\phi}, \quad (1.42)$$

$$\dot{\rho}_{\text{bar}} + 3H\rho_{\text{bar}} = 0, \quad (1.43)$$

$$\dot{\rho}_{\text{rad}} + 4H\rho_{\text{rad}} = 0. \quad (1.44)$$

where dots are time derivative and the prime is a derivative with respect to  $\phi$ . Using the notation from Amendola (2000), a coupling function  $\beta_c$  can be defined

$$\beta_c(\phi) \equiv \sqrt{\frac{3}{2}}M_{\text{Pl}}Q(\phi), \quad (1.45)$$

where  $M_{\text{Pl}} = 1/\sqrt{8\pi G}$  is the reduced Planck mass. Additionally, by integrating Eq. (1.42) and using Eq. (1.45), we find

$$\rho_{\text{DM}}(a) = \rho_{\text{DM}0}a^{-3} \exp\left(-\sqrt{\frac{2}{3M_{\text{Pl}}^2}}\int_{\phi_0}^{\phi}\beta_c(\tilde{\phi})d\tilde{\phi}\right), \quad (1.46)$$

where  $\rho_{\text{DM}_0}$  and  $\phi_0$  are today's values and  $a_0$  is taken to be unity. Assuming that particles are neither created or destroyed, their number density must be conserved. Thus, the mass of coupled particles must vary in time by following the variation of the scalar field

$$m_{\text{DM}}(a) = m_{\text{DM}_0} \exp \left( -\sqrt{\frac{2}{3M_{\text{Pl}}^2}} \int_{\phi_0}^{\phi} \beta_c(\tilde{\phi}) d\tilde{\phi} \right), \quad (1.47)$$

where  $m_{\text{DM}_0}$  is the dark matter particle mass today. In this thesis, the choice of the self-interacting potential will be limited to an exponential potential of the form

$$V(\phi) \propto e^{-\alpha\phi} \quad (1.48)$$

with  $\alpha = 0.1$  ([Amendola, 2000](#); [Macciò et al., 2004](#); [Baldi et al., 2010](#)).



## Chapter 2

# Galaxy Formation and Evolution

How the universe transitioned from a nearly homogeneous state to the formation of galaxies is referred to as structure formation. In the previous Chapter we saw that baryonic matter only accounts for about 15% of the total amount of matter. As a first approximation, baryonic matter can be neglected to focus on the collapse of large-scale structures. Then, we focus on baryonic processes involved in the formation of galaxies to describe smaller scale effects of structure formation.

One of the landmarks of the standard model for the structure formation is undoubtedly Jean's gravitational instability theory ([Jeans, 1902](#)). He realized that even when starting with an homogeneous and isotropic fluid, perturbations in density and velocity can form and these may evolve with time. The collapse of density perturbations is the result of an interplay between the smoothing effect of pressure and the collapse under the fluid self-gravity. When the effect of pressure is much smaller than the effect of gravity, the density perturbation will continue to grow by accreting surrounding mass. Eventually, this will become a gravitationally bound object. At the time [Jeans](#) demonstrated his criterion, the expansion of the universe was not known, but nonetheless we still use his adapted theory today.

### 2.1 Linear Structure Formation

As long as we measure the density distribution on sufficiently large scales, the assumptions of homogeneity and isotropy are correct. On the other hand, when looking at smaller and smaller scales our universe is extremely clumpy due to the clustering of matter. In the standard Big Bang model the universe started by being extremely hot, small and dense, and while expanding, it cooled down. The theory of Inflation was introduced to justify the fact that far apart patches of sky have the same CMB temperature, while they

---

should not have been in causal contact at recombination. The assumption is that only  $10^{-36}$  seconds after the Big Bang a scalar field (inflaton) drove an extremely fast accelerated expansion that was able to stretch space, so that regions that were firstly close to each other ended up being not anymore in causal contact when inflation ended,  $10^{-32}$  seconds after the Big Bang. Not only inflation stretched and flattened space, but it also laid the seeds for structure formation. In fact, quantum fluctuations in the hot and dense plasma were now enlarged and spread in space and seeded density perturbations in the homogeneous fluid. Measurements of density perturbations suggest that they are Gaussian distributed and, as predicted from the theory of Inflation (e.g. [Mukhanov 2005](#)), they have almost the same power at all scales. This translates into having a primordial power spectrum of the form

$$P_p(k) \propto k^n \quad (2.1)$$

with  $n = 0.965$  from the latest measurements ([Planck Collaboration et al., 2015](#)). Note that  $n \sim 1$  was a prediction of Inflation, and it would have been exactly  $n = 1$  in the asymptotic case of inflation lasting forever. We can quantify density perturbations by introducing the parameter  $\delta$ , defined by

$$\rho(\vec{x}, t) = \bar{\rho}(t)[1 + \delta(\vec{x}, t)] \quad (2.2)$$

where  $\bar{\rho}$  is the mean density.

The statistical description of density perturbations turns out to be more conveniently done in Fourier space. The Fourier expansion of the density perturbation is

$$\rho(\vec{x}, t) = \int \frac{d^3k}{(2\pi)^3} \delta_k(\vec{k}, t) e^{i\vec{k}\cdot\vec{x}} \quad (2.3)$$

where  $\vec{k}$  is the wave-number. We define linear regime the case in which  $\delta(\vec{x}, t) \ll 1$ , which is satisfied for redshifts  $z \lesssim 100$ . In this regime, the Fourier modes  $\delta_k(\vec{k}, t)$  can be treated as they evolved independently from one another. The evolution of each mode in Fourier space is governed by the following differential equation

$$\ddot{\delta}_k + 2H\dot{\delta}_k + \left[ \frac{c_s^2 k^2}{a^2} - 4\pi G\bar{\rho} \right] \delta_k = 0 \quad (2.4)$$

where  $H \equiv \dot{a}/a$  is the Hubble function and  $c_s$  the sound speed. The behavior of perturbations can be described using the Jeans length,

$$\lambda_J = \frac{2\pi a}{k_J} = c_s \sqrt{\frac{\pi}{G\bar{\rho}}}. \quad (2.5)$$

Perturbations on scales  $\lambda \ll \lambda_J$  are sound waves (i.e. the pressure contribution is much larger than gravity contribution), while on scales  $\lambda \gg \lambda_J$  gravity

dominates. In a flat, matter-dominated universe the growing solution for the density perturbations is

$$\delta = \text{const}_1 t^{2/3} + \text{const}_2 t^{-1} \quad (2.6)$$

where the dependance on time of the scale factor  $a \propto t^{2/3}$  in a matter-dominated universe has been used. Note how inefficient structure formation is once the expansion of the universe is taken into account, given that in the static case the growing solution describes an exponentially fast perturbation growth. In Eq. (2.4), the interplay between pressure and gravity is clearly shown. Furthermore, given that dark matter does not interact with radiation, dark matter perturbations could start growing undisturbed even before recombination. This process helped to speed up structure formation; in fact, by the time baryons were decoupled and free to collapse, they could fall into dark matter potential wells that already had already started to form. On the other hand, radiation and relativistic particles can also dissipate perturbations in baryonic density. The sum of all these effects shapes the Gaussian power spectrum coming from Inflation into the power spectrum at a given scale factor  $P(k, a)$ , these effects can be included in a function depending only on the wave number and on the scale factor, the *transfer function*  $T(k, a)$ .

$$P(k, a) = P_p(k) T(k, a)^2, \quad (2.7)$$

where  $P_p(k)$  is the primordial power spectrum at the end of inflation. The numerical implementation of all processes shaping transfer functions can be found in the scientific community. For this work, we will use an extended version of the code CAMB (Lewis and Bridle, 2002), modified to be suitable for dynamical dark energy cosmologies. The scenario that finally emerges is what is referred to as "bottom-up", since small linear scale structures form first and with time merge into more massive clustering. As we pointed out already, when density perturbations are small enough ( $\delta(\vec{k}) \ll 1$ ), we can treat structure formation with a linear approximation where each Fourier mode evolves independently from the others. Thus, the power spectrum scales as (see e.g. Coles and Lucchin, 2002):

$$P(k, a) = P(k, a_1) \frac{D_+^2(k, a)}{D_+^2(k, a_1)} = P_p(k) T(k, a)^2 \frac{D_+^2(a)}{D_+^2(a_1)} \quad (2.8)$$

where  $D_+^2(k, a) = D_+^2(a)$  when adopting the linear approximation (i.e. scales larger than the Jeans length) and  $D_+^2(a)$  is actually the growing mode of the density perturbations  $\delta$ .

### 2.1.1 Remarks on Linear Evolution and Dark Energy

#### Dynamical Dark Energy

By changing the evolution of the equation of state parameter for dark energy  $w \equiv p/\rho$ , see Eq. (1.27) and (1.31), the Hubble function in Eq. (1.28) will vary

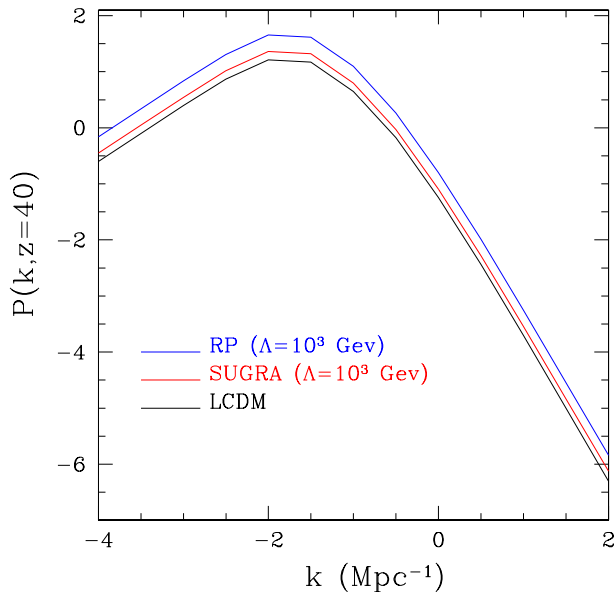


Figure 2.1: Power spectra for  $\Lambda$ CDM and dynamical dark energy models (SUGRA and RP) at  $z=40$ .

compared to the  $\Lambda$ CDM case. In turn, the evolution of density perturbations driven by Eq. (2.4) will be altered. Dark energy is not directly affecting the clustering but contributes to changing the expansion of the universe. The consequence is that structures in dynamical dark energy models will start forming at different times compared to  $\Lambda$ CDM, and, given a dynamical dark energy model, the choice of normalization will determine whether structure formation will be anticipated or delayed. Figure 2.1 shows power spectra for RP and SUGRA dark energy models (Macciò, 2004) for  $z = 40$ , chosen to have the same  $\sigma_8$  at  $z = 0$ . Structures in these dark energy models are more evolved compared to the  $\Lambda$ CDM case. It is possible to construct dynamical dark energy models so that, at a given redshift, structure will be less evolved compared to  $\Lambda$ CDM. We will further comment on dynamical dark energy structure formation times in Section 4.1, addressing the specific models used in this work.

### Coupled Dark Energy

While in the case of dynamical dark energy the effects on perturbation growth are only due to changes in the background expansion, in the case of coupled dark energy the change in the background is summed to the effects of the interaction between the two dark fluids. Consequently, Eq. (2.4)

becomes

$$\ddot{\delta}_c + (2H - \beta_c \dot{\phi}) \dot{\delta}_c - \frac{3}{2} H^2 [(1 + 2\beta_c^2) \Omega_c \delta_c + \Omega_b \delta_b] = 0, \quad (2.9)$$

where  $\Omega_c$  and  $\Omega_b$  are respectively the density parameters  $\Omega_i \equiv \rho_i / \rho_{\text{crit}}$  for cold dark matter and baryons, and  $\rho_{\text{crit}} = 8\pi G / 3H_0^2$  (Amendola, 2000, 2004a; Macciò et al., 2004; Pettorino and Baccigalupi, 2008). Two extra terms appear in Eq. (2.9) compared to the  $\Lambda$ CDM case, a friction term  $-\beta_c \dot{\phi} \dot{\delta}_c$  and the factor  $(1 + 2\beta_c^2)$  responsible for the enhancement of the gravitational force acting on cold dark matter particles, which is known as “fifth force”. In other words, an effective gravitational constant can be defined,

$$G_{\text{eff}} \equiv G[1 + 2\beta_c(\phi)^2], \quad (2.10)$$

with  $G$  Newtonian gravitational constant. As pointed out in Baldi 2011a, in the linear regime both these extra terms produce an acceleration of growth of cold dark matter density perturbations. On the other hand, when considering the non-linear effects, the friction term is responsible for lowering the concentration of dark matter haloes. This aspect will be further explored in Section 5.3.1.

The appearance of extra terms becomes clear when calculating the acceleration felt by the  $i$ -th dark matter particle in a coupled dark energy cosmology for the limit of a light scalar field (Baldi et al., 2010):

$$\dot{v}_i = \beta_c(\phi) \dot{\phi} \bar{v}_i + G_{\text{eff}} \sum_{j \neq i} \frac{m_j \bar{r}_{ij}}{|\bar{r}_{ij}|^3}, \quad (2.11)$$

where  $\bar{r}_{ij}$  is the distance between the  $i$ -th and  $j$ -th particles and  $\bar{v}_i$  and  $m_j$  are the velocity and the mass of the  $i$ -th and  $j$ -th particles. In this work, the coupling function is assumed to be in an exponential form (Amendola, 2004a; Baldi, 2011a)

$$\beta_c(\phi) \equiv \beta_0 e^{\beta_1 \phi}, \quad (2.12)$$

where  $\beta_0$  is today’s value. In this work we will study both the case of a constant coupling  $\beta_1 = 0$  and the case of a growing coupling  $\beta_1 > 0$ . Our specific choices will be outlined in Section 5.1.

Concluding, the main effects of introducing a coupling between dark matter and dark energy are: (i) dark matter particles masses change with time, while baryonic masses stay constant, (ii) the gravitational strength felt by dark matter particles is stronger than in Newtonian dynamics, (iii) an extra friction term appears, which has the consequence of increasing gravitational collapse on the linear level, but we will show that on the non-linear level will be helpful in lowering halo concentrations and decreasing the number and concentrations of subhaloes (see Chapter 5).

---

## 2.2 Non-Linear Structure Formation

The success of linear theory is undoubtedly significant, but once density perturbations become  $\delta \sim 1$ , the linear approximation inevitably breaks down. In fact, at few kpc away from the center of a luminous galaxy, the density is around  $10^5$  times larger than the critical density  $\rho_c$ . Thus, to properly investigate galaxy formation, we need to be able to follow the behavior of highly non-linear density fluctuations.

### 2.2.1 Spherical Collapse

In a three-dimensional distribution of density perturbations, we choose one of them and describe its collapse (Binney and Tremaine, 1987). We assume that the background model is described by a flat FLRW metric and that the universe is dark matter dominated. Most structures indeed form between radiation-matter equality ( $z_{rm} \simeq 3100$ ) and matter-dark energy equality ( $z_{m\Lambda} \simeq 0.5$ ). Additionally, the density perturbation  $\delta_i \ll 1$  at some initial time  $t_i$  is assumed to be spherically symmetric with radius  $r_i$ .

Matter around the perturbation feels the gravitational attraction of the interior mass  $M$ , which can be calculated given the dependence of matter density on the scale factor in Eq. (1.14). The total mass in the sphere  $M$  is obtained and the evolution of the perturbation radius  $r(t)$  can be calculated using Newton's law

$$\frac{d^2r(t)}{dt^2} = -\frac{GM}{r(t)^2}. \quad (2.13)$$

By solving the second order acceleration differential equation, the turn-around radius can be obtained, radius at which expansion stops and the collapse starts. The overdensity at turn-around is  $\delta_t = 4.55$ .

In reality density perturbations are not spherically symmetric nor isolated and the collapse process is much more complex. Dark matter overdensities finally will collapse into an ellipsoid configuration referred to as *halo*. Through collapse, mixing and relaxation processes, haloes reach their virial equilibrium at about the same time that the toy model collapses into a singular density at  $r = 0$ . Using the virial theorem, one finds that the halo density is about 200 times the background density. This density ratio derived from the spherical collapse model is widely used in cosmology for characterizing dark matter haloes and their formation and we will make use of it in Chapter 4 and 5 to define haloes virial radii.

Thus, overdensities that will turn into haloes can be identified by a threshold set by a critical overdensity  $\delta_c$ . In fact, they can be traced to regions where the density at one point in time  $t_i$  exceeded  $\delta_c$ . By using the turn-around time, one can obtain

$$\delta_c(t_i, t) = 1.686(t_i/t)^{2/3}, \quad (2.14)$$

where  $t$  is the collapse time.

### 2.2.2 Press-Schechter Mass Function

In the same way that over-dense perturbations continue to become more and more massive by attracting dark matter mass, under-dense regions (voids) become emptier and emptier. Voids grow in size with time and merge into bigger voids, forcing matter into the high density walls around them (sheets). While the collapse continues, the chance of sheets crossing each other increases, and, when this happens, a high density filament is produced. Mass tends to move along the filaments towards their intersections (nodes). These are the high density regions where galaxy clusters will form.

Structure formation is *hierarchical*, meaning that smaller objects form first and merge into bigger systems. Galaxies form in the centre of virialized haloes and are heavily influenced by halo merging. Mergers between haloes of comparable mass are referred to as *major mergers*, while those between different mass haloes are said to be *minor mergers*. As a result of the specific merger history, a *parent halo* may contain smaller haloes (*subhaloes*) orbiting around it.

In this picture, at any given redshifts, haloes with a wide range of masses are present. A very powerful information is their distribution as a function of mass, i.e. the number density of haloes at given redshift within the mass range  $M$  and  $M + dM$ , the *mass function*.

Press and Schechter (1974) suggested that the probability of finding the density contrast at or above the linear density contrast for spherical collapse,  $\delta_c$ , is equal to the fraction of the cosmic volume filled with haloes of mass  $M$ . They derived the comoving number density of haloes with masses between  $M$  and  $M + dM$ , (see e.g. Bartelmann 2012)

$$N(M, a)dM = \frac{1}{\sqrt{\pi}} \frac{\rho_m \delta_c}{D_+(a)} \frac{d \ln \sigma_R}{dM} \exp\left(-\frac{\delta_c^2}{2 \sigma_R^2 D_+^2(a)}\right) \frac{dM}{M} \quad (2.15)$$

with  $\sigma_R(a) = \sigma_R D_+(a)$  being the Gaussian variance of the density contrast distribution at a given scale factor with characteristic scale  $R = [3M/(4\pi\rho_m)]^{1/3}$ , which is defined as

$$\sigma_R(a)^2 = \frac{1}{(2\pi)^3} \int d^3k P(k, a) W^2(kR) \quad (2.16)$$

with  $P(k, a)$  power spectrum for density perturbations and  $W^2(kR)$  a filter function on the scale  $R$ . Thus, the mass function at a given scale factor is defined by (i) the primordial power spectrum normalization and (ii) the transfer function  $T(k, a)$ , see Eq. (2.1) and (2.7). The normalization length scale is commonly chosen to be 8 Mpc/h and the variance at this scale is referred to as  $\sigma_8$ .

---

Despite its simple starting assumptions, the Press-Schechter mass function describes remarkably well the mass distribution of dark matter haloes in cosmological simulations and its use can be extended to dynamical dark energy models by evaluating the corresponding transfer functions. For what concerns coupled dark energy models, Eq. (2.13) is no longer valid, thus a revised spherical collapse and consequent Press-Schechter function would need to be calculated.

### 2.2.3 The Zel’dovich Approximation

A kinematical treatment to follow the evolution of density perturbations further into the non-linear regime was put forward in Zel’dovich (1970).

The basic idea underlying the Zel’dovich approximation is assuming that particles will move forward in the direction of their initial displacement. In co-moving coordinates Zel’dovich’s equation is

$$\vec{x}(t) = \vec{x}_{\text{ini}} - D_+(t) \frac{\vec{\nabla}^2 \Phi_{\text{ini}}}{4\pi G \rho_{\text{ini}}} \quad (2.17)$$

where  $\Phi_{\text{ini}}$  and  $\rho_{\text{ini}}$  are the gravitational potential and the density at the initial displacement  $\vec{x}_{\text{ini}}$ . This approximation is accurate until particle trajectories cross and their mapping is no longer unique (shell-crossing). Eq. (2.17) is widely used to determine particle displacements in initial conditions for numerical simulations. In Section 3.1 we further explain its application.

## 2.3 N-Body Simulations of the Large-Scale Structure of the universe

Non-linear analytic methods are extremely useful to bring insights in the physical processes involved in structure formation, but often are not accurate enough to compare their predictions to observations due to the highly complex behavior of fluctuations once they enter the fully non-linear regime. Thus, numerical simulations must enter into the picture. Typically, a volume of the universe is represented by a density distribution discretized by point-like particles that interact with each other gravitationally. The volume is characterized by periodic boundary conditions to mimic large scale structures. Dark matter only (or N-body) simulations of the large scale structures (e.g. Springel et al. 2006) are in excellent agreement with observations (e.g. Alam et al. 2015), which implies that on large scales baryonic matter traces the dark matter distribution. Figure 2.2 shows the large-scale dark matter distribution at different redshifts from the Millenium simulation (Springel et al., 2006).

A large quantity of information can be derived from N-body simulations, such as dynamics of mergers between galaxies (Toomre and Toomre, 1972),

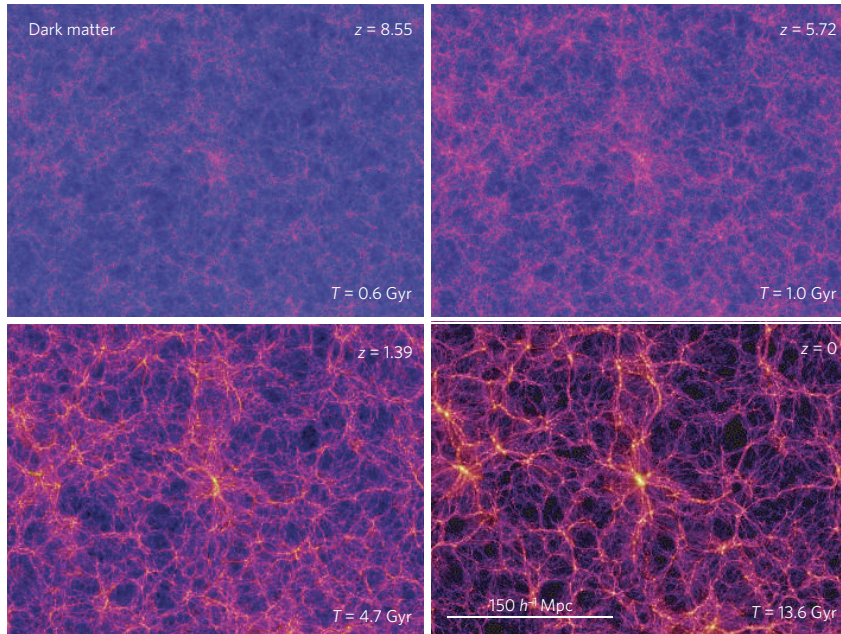


Figure 2.2: Time evolution of the cosmic large-scale structure obtained from cosmological dark matter only simulation of the  $\Lambda$ CDM model. Credit to [Springel et al. \(2006\)](#).

global properties of dark matter haloes, mass and angular momentum distribution ([Barnes and Efstathiou, 1987](#)), merger histories ([Lacey and Cole, 1993](#)) and density profiles of dark matter ([Navarro et al., 1997](#)). Various numerical algorithms are available to describe the gravitational interactions between a large number of particles. In the following we firstly describe the most commonly known algorithms and then we summarize results from numerical simulations that will be significant for the next chapters.

### 2.3.1 Particle-Particle Method

The simplest algorithm to solve the gravitational interactions between  $N$  particles directly sums the  $(N - 1)$  Newton force contributions. This calculation is often called *particle-particle* (PP) computation ([Gould et al., 1988](#)). By discretizing time, one calculates the acceleration at a given time-step and uses it to update velocities and positions at the following time-step. On top of being very computationally expensive, the method also suffers from a divergence, given that the gravitational force scales as  $1/r$ . This problem is solved assuming that particles are not point-masses but extended spherical objects with size of the order of the gravitational softening length  $\epsilon$ , which is equivalent to assuming the following formulation for the Newtonian force

---

on the  $i$ -th particle:

$$\vec{F}_i = -G \sum_{i \neq j} \frac{m_i m_j (\vec{x}_j - \vec{x}_i)}{(\epsilon^2 + |\vec{x}_i - \vec{x}_j|^2)^{3/2}}, \quad (2.18)$$

where  $m$  and  $\vec{x}$  are mass and position of  $i$ -th and  $j$ -th particles. As a consequence, the distribution of matter can only be trusted at scales  $\gtrsim \epsilon$  and  $\epsilon$  is often quoted as the spacial resolution of the simulation. The calculation tends to be very slow since the method requires  $N(N-1)/2$  evaluations of Eq. (2.18) for each time-step.

### 2.3.2 Particle-Mesh Method

In order to improve the efficiency of the PP-method, [Bertschinger and Gelb \(1991\)](#) suggested the *particle-mesh* scheme. Forces are calculated on a regular grid to which mass points are assigned and the potential is calculated using the Fast Fourier Transform (FFT) method. The big advantage is that the computational cost of the method becomes proportional to  $N \log N$ . The downside of this technique is the poor resolution on small physical scales due to the finite size of the grid. To solve this issue, hybrid PP-PM methods have been developed ([Brandt and Lubrecht, 1990](#)). The PM part computes the long range forces which are slowly varying and the PP part computes the short range forces between close particles.

### 2.3.3 Tree Algorithms

The technique was firstly proposed by [Appel \(1985\)](#) and its basic idea consists of grouping particles so that distant particle clumps can be treated as one single massive particle, lowering the total number of calculations. The grouping is performed with a hierarchical subdivision procedure, which consists in dividing cells that contain more than one particle in sub-cells which in turn will be subdivided until only one particle is found in the cell. In this way the fine grid is created to compute small-range forces. With this optimization the computational cost can be reduced to  $N \log N$ .

### 2.3.4 Halo mass Function

From the Press-Schechter theory briefly delineated in Section 2.2.2, one can obtain a prediction from the number density of parent haloes as a function of mass which can be compared with N-body simulations. [Jenkins et al. \(2001\)](#) show that the simulated mass function is almost independent of epoch, of cosmological parameters and of the initial power spectrum when expressed in appropriate variables, exactly as predicted by the Press-Schechter model. On the other hand, the model predicts a mass function shape that differs from their numerical results, overestimating the abundance of less massive

haloes and underestimating that of massive systems. [Sheth et al. \(2001\)](#) generalize the spherical-collapse model to the case of collapsing ellipsoidal bodies and showed that their prediction is in much better agreement with numerical simulations.

### 2.3.5 Radial Density Profiles

In numerical simulations dark matter haloes seem to follow remarkably well a universal mass density profile that can be described by two power laws,

$$\rho(r) = \frac{\rho_c}{(r/r_s)^\alpha (1 + r/r_s)^{\beta-\alpha}}, \quad (2.19)$$

with  $\beta \simeq 3$  and  $1 \lesssim \alpha \lesssim 1.5$ . Eq. (2.19) with the choice of  $\alpha = 1$  and  $\beta = 3$  is known as the Navarro Frank and White (NFW) profile ([Navarro et al., 1995](#)), with  $\rho_c$  critical density and  $r_s$  scale radius. Haloes in collisionless simulations seem to settle to this profile regardless the cosmological parameters and the power spectrum ([Navarro et al., 1996](#)). This is also the case for dark matter haloes in dynamical dark energy ([Klypin et al., 2003](#)) and coupled dark energy ([Baldi et al., 2010](#)). Though, the origin of the universality of the profile is not yet well understood. [Navarro et al. \(1995\)](#) and [Moore et al. \(1999, 2004\)](#) show that simulations of halo virialization tend to produce profiles with  $\alpha \simeq 1$  and it can be shown that haloes that arises from merging many small haloes will acquire the density profile of their progenitors [Binney and Tremaine \(1987\)](#). Thus, the universality of the NFW profile may start from the virialization of the first haloes and survive the consecutive mergers.

## 2.4 Hydrodynamical Processes in Galaxy Formation

Over the last decades, the astronomical community has come to the conclusion that galaxies are only the visible part of much more massive systems composed mainly of dark matter; furthermore these dark matter haloes are embedded in a uniform distribution of dark energy. The way dark matter and dark energy behave and their properties build up the cosmological model, which in turn provides the starting conditions and the evolutionary guidelines to the formation of structures. Despite our incomplete understanding of the dark sector, we are nonetheless able to build up a coherent picture for the evolution of galaxies by modeling baryonic processes into numerical simulations to finally test predictions from simulations with observations. In fact, all the observational evidence that we have gathered on the universe comes from emissions from baryonic matter. For this reason, in the following Section we will summarize the behavior of baryons while the formation of structures took place.

---

### 2.4.1 Accreting Gas and Cooling Process

As described in Section 1.3.1, prior to decoupling ( $z \simeq 1100$ ) baryons were coupled to photons and their density perturbations were being wiped out by the radiation pressure contribution. On the other hand, being dark matter decoupled from photons at all times, its perturbations were growing undisturbedly and after decoupling baryons fell into the already existing dark matter potential wells. Given that the ratio of baryonic to dark matter mass is quite small, the gravitational consequences of the collapse due to baryons from the decoupling to  $z \simeq 30$  was not significant (e.g. Binney and Tremaine, 1987), while on the contrary, from  $z \simeq 30$  onwards, the role of baryons was crucial in the collapse process due to their ability of radiating away energy gained from the gravitational sinking. The atomic gas was heated by collisions between the newly formed hydrogen and helium atoms and emitted photons and free electrons. Consequently, hydrogen molecules started to be formed thanks to the presence of free electrons. By radiating photons from the excited atoms and molecules, the gas was able to lose its acquired gravitational energy and sank into the halo center. Thus, baryon density in the inner regions increased dramatically until the gas became optically thick to photons. Photons were now confined and started heating the gas. Increasing the temperature allowed the central regions to reach a dynamical equilibrium and star formation could begin. Around  $z \simeq 20$  the first stars were formed which in turn re-emitted ionizing photons in the universe, and by  $z \simeq 6$  the whole universe was once more filled with ionized gas (reionization epoch) with temperature  $T \simeq 10^4 K$ . Only haloes that at reionization were massive enough were able to form stars. In fact, the thermal velocity for hydrogen at a temperature of  $10^4 K$  is about 10 km/s, which had to be less than the halo escape velocity in order for the gas to stay in the halo and form stars. Furthermore, in small haloes gas could not cool below the UV background temperature. As a consequence, only haloes more massive than around  $10^8 M_\odot$  were able to start forming stars. This is a crucial point for the evolution of dwarf galaxies (see Section 4.4).

The cooling time for gas is

$$t_{\text{cool}} \propto \frac{T}{\dot{E}}, \quad (2.20)$$

where  $T$  is the temperature and  $\dot{E}$  the rate per particle at which gas radiates.  $\dot{E}$  is proportional to the gas density, which implies that the cooling time is shorter in the dense inner halo regions. The cooling time has to be compared to the free fall time of a system with density  $\rho$ , namely the time it takes the system to collapse,

$$t_{\text{ff}} \propto \frac{1}{\sqrt{G\rho}}. \quad (2.21)$$

Rees and Ostriker (1977) studied the gas cooling process at the epoch when

the gas has stopped expanding with the background universe but has not yet fragmented into stars; they defined two distinct cases. (i)  $t_{\text{cool}} > t_{\text{ff}}$ , gas cooling is a slow process and the system has the time to react and adjust, so that the hydrostatic equilibrium is restored. (ii)  $t_{\text{cool}} < t_{\text{ff}}$ , the gas cooling is too fast for the system to react accordingly and it falls out of hydrostatical equilibrium; as a consequence, star formation is extremely efficient. Case (ii) applies for galaxies whose halo mass is  $\lesssim 10^{12} M_{\odot}$ .

### 2.4.2 Star Formation and Feedback Mechanisms

When gas cools, it can reach the center and form stars. Thus, a zero-*th* order approximation sets the star formation rate density being proportional to the gas density through the inverse of the free-fall time

$$\frac{d\rho_{\text{star}}}{dt} \propto \frac{\rho_{\text{gas}}}{t_{\text{ff}}}. \quad (2.22)$$

Taking the  $t_{\text{ff}}$  from Eq. (2.21) with  $\rho = \rho_{\text{gas}}$ , one obtains

$$\frac{d\rho_{\text{star}}}{dt} \propto \rho_{\text{gas}}^{3/2}. \quad (2.23)$$

Observationally, the proportionality between star formation rate surface density and gas surface density  $\Sigma_{\text{SFR}} \propto (\Sigma_{\text{gas}})^n$  was firstly found by Schmidt (1959). Schmidt used measurements of the solar neighborhood and found  $n \simeq 2$ . More recently Kennicutt (1998) used observations from around a hundred nearby galaxies finding  $n \simeq 1.4$ .

On the other hand, only a small fraction of the cold molecular gas ( $T \simeq 20\text{K}$ ) is transformed into stars, while its majority is blown away into the inter stellar medium (Krumholz and Tan, 2007). This re-injection of energy in the inter stellar medium is referred to as *stellar feedback* and acts towards suppressing star formation. Larson (1974) showed that due to supernova explosions the interstellar gas is heated and driven out of the galaxy in a galactic wind. The gas loss is significant, especially in smaller galaxies. Supernovae can be held responsible for two different types of feedback: firstly, as mentioned by Larson, the gas is given momentum from the explosion and can be expelled from the galaxy (kinetic feedback). Secondly, supernovae can heat the surrounding gas to temperatures  $T \simeq 10^6\text{K}$  which can produce velocities that are greater than the galaxy escape velocity (Dekel and Silk, 1986). The pressure of the surrounding heated gas can drive gas bulk motions which can drive out of the galaxy much more gas in forms of galactic outflows (thermal feedback).

Furthermore, a second class of feedback mechanisms is associated with the presence of an active black hole in the center of the galaxy (active galactic nucleus) and it is as well believed to be able to suppress star formation in galaxies (Springel et al., 2005; Di Matteo et al., 2005; Croton et al., 2006).

---

## 2.5 Hydrodynamics

Since gas can cool and be heated, treating its hydrodynamics is a much more complicated task than the gravity only case. While gravity is a long range force, baryonic processes mostly act on scales  $\lesssim 1$  Mpc, which makes their implementation crucial to understand the formation of galaxies. Currently available hydrodynamical codes can be grouped in three types: Eulerian grid-based hydrodynamics, Lagrangian Smoothed Particles Hydrodynamics (SPH) and the more recent moving mesh hydrodynamics. Differences lie in the choices of discretization and reference systems. Eulerian grid-based methods (Stone and Norman, 1992; Cen, 1992; Teyssier, 2002) build a space grid and solve the equations of motion in the reference frame of a static observer. Lagrangian SPH codes (Lucy, 1977; Gingold and Monaghan, 1977; Monaghan, 1992; Wadsley et al., 2004; Springel, 2005) describe the density field with a finite number of point masses and solve the equations of motion in the reference frame of each fluid element. Moving mesh hydrodynamics codes have a unstructured space grid that moves along with the fluid elements.

In the limit of an inviscid and non-conducting gas, the following set of equations describes the hydrodynamics of the system

$$\frac{D\rho}{Dt} = -\rho\vec{\nabla}\cdot\vec{u}, \quad (2.24)$$

$$\rho\frac{D\vec{u}}{Dt} = -\vec{\nabla}p - \rho\vec{\nabla}\Phi, \quad (2.25)$$

$$\rho\frac{D\epsilon}{Dt} = -p\vec{\nabla}\cdot\vec{u} - \Lambda(\epsilon, \rho), \quad (2.26)$$

where  $\vec{u} \equiv \langle \vec{v} \rangle$  is the mean fluid velocity at  $(\vec{x}, t)$ ,  $D/Dt \equiv \partial/\partial t + \vec{u}\cdot\vec{\nabla}$ ,  $\rho$ ,  $p$ ,  $\Phi$  and  $\epsilon$  are density, pressure, gravitational potential and internal energy per unit mass and  $\Lambda(\epsilon, \rho)$  is the cooling function, which denotes radiative cooling and other photon emission processes. With the addition of the equation of state  $\epsilon = 1/(\gamma - 1)p/\rho$ , the system completely describes the dynamics of a perfect gas.

In this work we study the formation of galactic structures in dynamical and coupled dark energy. To do so, we will use two SPH codes, GASOLINE (Wadsley et al., 2004) and GADGET2 (Springel, 2005). In the next Section we will briefly summarize details regarding SPH codes.

### 2.5.1 SPH Method

Analogously to N-body collisionless simulations, SPH codes discretize a continuous fluid with a finite number of particles. A position  $\vec{r}_i$ , velocity  $\vec{v}_i$ , density  $\rho_i$  and internal energy  $\epsilon_i$  are assigned to each particle. All hydrodynamic quantities are then replaced by their smoothed estimates, i.e. local

averages from kernel interpolations. Given a scalar field  $f$ , its smoothed field  $\langle f \rangle$  is

$$\langle f(\vec{r}) \rangle = \int d^3u f(\vec{u}) W(\vec{r} - \vec{u}, h), \quad (2.27)$$

where  $h$  is the smoothing length and  $W(\vec{r} - \vec{u}, h)$  smoothing kernel, which satisfies

$$\lim_{h \rightarrow 0} \langle f(\vec{r}) \rangle = f(\vec{r}). \quad (2.28)$$

An often used choice for the kernel can be found in [Hernquist and Katz \(1989\)](#). When the number of particles is large enough, the continuous form for  $\langle f(\vec{r}) \rangle$  can be discretized by

$$\langle f(\vec{r}) \rangle = \sum_{j=1}^N \frac{m_j}{\rho_j} f(\vec{r}_j) W(\vec{r} - \vec{r}_j, h). \quad (2.29)$$

[Springel \(2010\)](#) shows that this approximation is accurate if the number of neighbors used for the smoothing is  $N \approx 33$ . Thus, ignoring diffusive and self-gravity terms, the system of equations can be rewritten as

$$\rho_i = \sum_{j=1}^N m_j W(\vec{r}_i - \vec{r}_j, h), \quad (2.30)$$

$$\frac{D\vec{u}_i}{Dt} = - \sum_{j=1}^N m_j \left[ \frac{p_i}{\rho_i^2} + \frac{p_j}{\rho_j^2} \right] \vec{\nabla}_i W(\vec{r}_i - \vec{r}_j, h), \quad (2.31)$$

$$\frac{D\epsilon_i}{Dt} = \frac{p_i}{\rho_i^2} \sum_{j=1}^N m_j (\vec{u}_i - \vec{u}_j) \cdot \vec{\nabla}_i W(\vec{r}_i - \vec{r}_j, h). \quad (2.32)$$

A second possibility to evaluate the hydrodynamical equations is to use an entropy conserving scheme. Based on [Springel and Hernquist \(2002\)](#), in GADGET-2 implementation Eq. (2.32) is exchanged with

$$\epsilon_i = s_i \frac{\rho^{\gamma-1}}{\gamma - 1}, \quad (2.33)$$

where  $s_i$  is the particle entropy.

When shocks are generated, gas can no longer be treated as an inviscid fluid. Since SPH has no explicit treatment of physical viscosity, an artificial viscosity term needs to be introduced to account for dissipation in shocks. This term is responsible for smearing out shocks and for introducing dissipation in regions with strong velocity divergence, and appears in Eq. (2.31)

---

and (2.32) with the following extra terms

$$\left. \frac{D\vec{u}_i}{Dt} \right|_{\text{visc}} = - \sum_{j=1}^N m_j \Pi_{ij} \vec{\nabla}_i W(\vec{r}_i - \vec{r}_j, h), \quad (2.34)$$

$$\left. \frac{D\epsilon_i}{Dt} \right|_{\text{visc}} = \frac{1}{2} \sum_{j=1}^N m_j \Pi_{ij} (\vec{u}_i - \vec{u}_j) \cdot \vec{\nabla}_i W(\vec{r}_i - \vec{r}_j, h), \quad (2.35)$$

where  $\Pi_{ij}$  is the viscous stress tensor. Furthermore, the change in entropy is given by

$$\left. \frac{Ds_i}{Dt} \right|_{\text{visc}} = \frac{1}{2} \frac{\gamma - 1}{\rho_i^{\gamma-1}} \sum_{j=1}^N m_j \Pi_{ij} (\vec{u}_i - \vec{u}_j) \cdot \vec{\nabla}_i W(\vec{r}_i - \vec{r}_j, h). \quad (2.36)$$

To conclude, a recipe for galaxy formation is not an easy task. Limits arise both from our incomplete knowledge of the physics involved, and from the computational limitations of present day machines. In fact, in order to implement at best the baryonic processes involved in galaxy formation, sub-grid models need to be adopted. The various implementations can change significantly depending on the code used, but are nonetheless a key ingredient to model the formation of galaxies. We will describe more in depth the sub-grid model adopted in GASOLINE, and used in this work, in Section 3.2.1.

# Chapter 3

## Numerical Methods

### 3.1 Generating Initial Conditions

After recombination all species are free to collapse and by redshift  $z \sim 100$  (typical starting redshift for numerical simulations) density fluctuations are present in all components. Depending on the details on the inflation theory, initial perturbations might have various distributions. To this day, measurements of the CMB temperature anisotropies hint that initial perturbations were most probably Gaussian, which means that they can be fully described by a power spectrum. Thus, given amplitude and spectrum, which depend on the cosmological model, initial density fluctuations can be generated. [Doroshkevich et al. \(1980\)](#) were the first to use the Zeldovich approximation to set initial conditions for numerical simulations. Here we show the guiding equations ([Klypin, 2000](#))

$$\vec{x} = \vec{q} - \alpha D_+(t) \sum_k \vec{\nabla}_q \Phi(k, \vec{q}), \quad (3.1)$$

$$\vec{p} = -\alpha a^2 \dot{D}_+(t) \sum_k \vec{\nabla}_q \Phi(k, \vec{q}), \quad (3.2)$$

where  $\vec{x}$  and  $\vec{q}$  are the comoving and Lagrangian coordinates,  $\Phi$  the velocity potential, obtained from

$$\Phi(k, \vec{q}) = \sum_k a_k \cos(k \vec{q}) + b_k \sin(k \vec{q}). \quad (3.3)$$

$a_k$  and  $b_k$  are random numbers that depend on the value of the power spectrum at a given wave number, as in

$$a_k = \sqrt{P(k)} \frac{\text{random}(0, 1)}{k^2}, \quad b_k = \sqrt{P(k)} \frac{\text{random}(0, 1)}{k^2}. \quad (3.4)$$

Thus, the power spectrum  $P(k)$  and the value of the parameter  $\alpha$  in Eq. (3.1) define the normalization of the density fluctuations. The box size  $L_{\text{box}}$  and

---

the number of particles  $N$  of the simulations set the grid for the initial conditions. The phase space is thus divided in cubes of size  $2\pi/L_{\text{box}}$ . A realization of the spectrum of perturbations  $a_k$  and  $b_k$  is obtained when choosing two random numbers and the particle displacements and momenta are found using Eq. (3.1).

### 3.1.1 GRAFIC2-DE

The process of generating initial conditions described in the previous Section obtains the same resolution for the full simulation volume  $L_{\text{box}}^3$ . In many cases it can be convenient to set initial conditions such that the highest resolution is achieved only in a portion of the full volume, in order to limit the computational time. This is the case of single-galaxy simulations, in which we are interested in having the highest possible resolution for the particles belonging to the halo and its surroundings, but we are not concerned with the remaining portion of the cosmological volume except for its gravitational contribution which does not vary significantly if the resolution is set to be lower. As a consequence, particles with different masses will compose the cosmological volume; specifically, the least massive particles will build up the halo and the most massive the outskirts of the volume.

The production of such multi-mass initial conditions is achieved in two steps. Firstly, we simulate a low resolution dark matter only box, where all particles have the same mass. We select the halo we want to investigate and we define a volume around it that will have the highest resolution (often called Lagrangian volume); in this work, in most cases we choose a sphere of three times the halo's virial radius. Using the particles identification numbers (IDs), all particles belonging to the sphere are traced back to the redshift at which we want the high resolution simulation to start ( $z = 99$  in this work). The initial conditions generator enlarges the Lagrangian volume to the minimum closed volume, i.e. volume where no sub-volumes with low resolution particles are present. High-frequency harmonics are then added in the high resolution volume and the phase space is divided in smaller boxes, e.g.  $2\pi/L_{\text{box}} \cdot N/2$ . Figure 3.1 shows an example of mass refinement in 2D real space. Three central blocks of particles were chosen for the highest mass resolution. Each block produces  $16^2$  of the smallest particles (16 is referred to as refinement factor  $RF$ ). Adjacent blocks have one step lower resolution and produce  $8^2$  particles each ( $RF = 8$ ). The procedure is repeated recursively producing fewer more massive particles at each level (Klypin, 2000).

For this work we have modified the multi-mass initial condition generator code GRAFIC2 (Bertschinger, 2001). The original code assumes a  $\Lambda$ CDM cosmology, and I and L. Casarini adapted it into GRAFIC2-DE, a code which requires the background cosmology as an input. More in detail, the input needs to provide the evolution as function of the expansion factor for ( $i$ ) density parameters for dark matter, baryons and dark energy (a flat

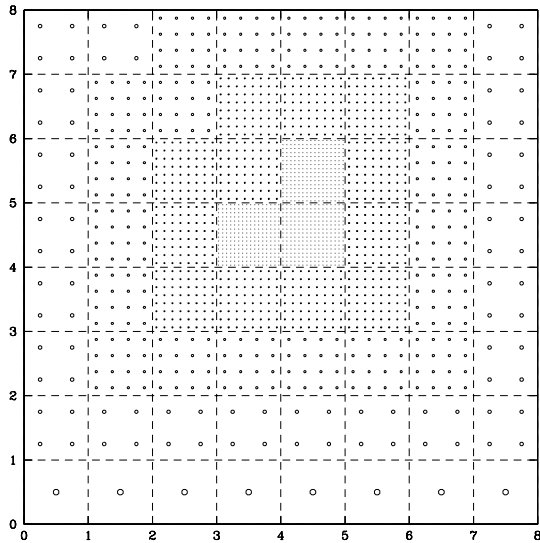


Figure 3.1: An example of mesh with four refinement levels.

universe is assumed), *(ii)* growth factor  $D_+$  and its logarithmic derivative  $f_\Omega \equiv d \ln D_+ / d \ln a$  and furthermore *(iii)* transfer functions for dark matter and baryons. The codes performs an interpolation of the background quantities and is able to produce multi-mass initial conditions for cosmological simulations for a wide range of non- $\Lambda$ CDM cosmologies. I performed a series of tests to ensure that the two codes are equivalent, given the same  $\Lambda$ CDM cosmology. Furthermore, GRAFIC2-DE reproduces expected results for cosmologies previously studied in literature (we used Ratra Peebles dark energy models for testing). GRAFIC2-DE was used to generate initial conditions for all numerical simulations presented in this work.

## 3.2 N-body and SPH Solvers

### 3.2.1 GASOLINE-DE

GASOLINE (Wadsley et al., 2004) is a SPH tree code based on the gravity algorithms of the N-body code PKDGRAV (Stadel, 2001). GASOLINE solves the equations of hydrodynamics and includes radiative cooling. The *gas cooling* used (Shen et al., 2010) includes, photoionization and heating from the Haart & Madau (unpublished) ultraviolet background radiation, Compton cooling, hydrogen and helium metal cooling from 10 to  $10^9$ K.

Gas particles begin *star formation* when they are cool ( $T \leq 1.5 \times 10^4$ K) and dense ( $n \geq 9.3 \text{cm}^3$ ). A sub-set of these particles is then stochastically selected to actually form stars, so that the Kennicutt Schmidt (Schmidt, 1959; Kennicutt, 1998) law is reproduced. The star formation equation used

---

is

$$\frac{\Delta M_*}{\Delta t} = c_* \frac{M_{\text{gas}}}{t_{\text{dyn}}}, \quad (3.5)$$

where  $\Delta M_*$  is the mass of star particle formed,  $\Delta t$  is the time step between star formation events ( $8 \times 10^5 \text{yr}$  in all the simulations described in Section 4.2),  $c_*$  is a constant formation efficiency factor and  $t_{\text{dyn}}$  is the gas dynamical time (Stinson et al., 2013b).

*Supernova (SN) feedback* follows the ‘blastwave model’ (Stinson et al., 2006). At the end of their lives stars more massive than  $8 M_{\odot}$  are assumed to explode as Type II SNe and their lifetimes are based on Raiteri et al. (1996). The energy emitted from explosions is transferred to the surrounding dense gas which would quickly radiate it away. For this reason, cooling is disabled inside the blast region for a period of time following McKee and Ostriker (1977).

For SN II, metals produced in stars are released as the main sequence progenitors die and distributed to the same gas within the blast radius as is the SN energy ejected from SN II (Shen et al., 2010). Iron and oxygen are produced in SN II according to the analytic fits used in Raiteri et al. (1996). In summary, each stellar generation of  $10^4 M_{\odot}$  produces, in a lifetime of a  $1 M_{\odot}$  star, about 49 SN II and 9 SN Ia events. These eject about 600 and  $10 M_{\odot}$  of metal enriched material respectively, which translate into about  $7 M_{\odot}$  of iron and  $48 M_{\odot}$  of oxygen that will impregnate the interstellar medium.

Feedback from SN Ia also follows the model in Raiteri et al. (1996), but in this case radiative cooling was not disabled. Each SN Ia produces  $0.6 M_{\odot}$  of iron and  $0.13 M_{\odot}$  of oxygen (Thielemann et al., 1986) and the metals are ejected into the nearest gas particle for SN Ia.

Finally, the latest addition to the sub-grid hydrodynamical model is *early stellar feedback* (Stinson et al., 2013b), which mimics the radiation energy from young massive stars, and is introduced immediately after stars form. This is motivated by radiation pressure driving winds out of massive star clusters. On the other hand, given the resolution, typically a molecular cloud is described by maximum a few gas particles, which implies that stellar winds cannot be resolved, thus thermal pressure is used instead. Thermal feedback provides pressure support and increases the gas temperature, which in turn decrease star formation.

With the introduction of the early stellar feedback, Stinson et al. (2013b) drastically improved the *over-cooling problem* affecting previous galaxy simulations. In short, simulated disc galaxies were producing too many stars compared to observations and these stars concentrated in the galactic center produced peaked rotation curves, which are not in agreement with observationally measured flat rotation curves. By accounting for the energy emitted in the inter stellar medium by massive stars before they explode as SNe, Stinson et al. simulated realistic disc galaxies (i.e. star formation histories matching observational constraints, flat rotation curves and exponential sur-

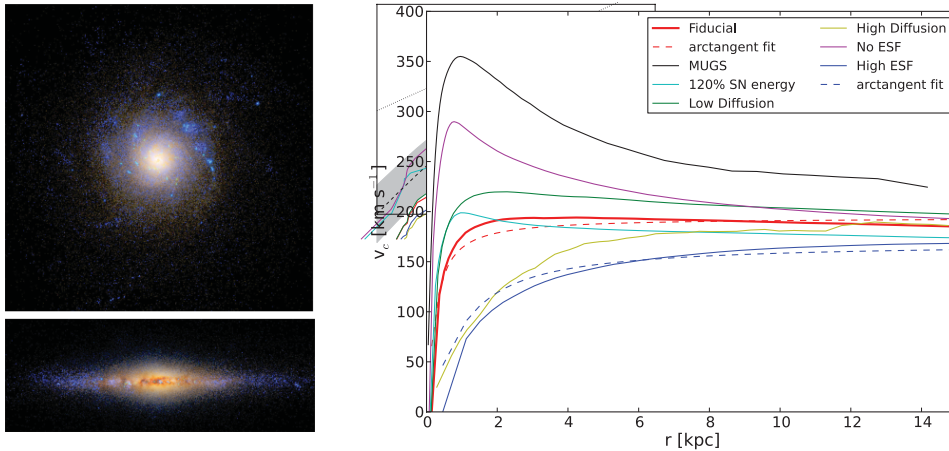


Figure 3.2: Right panel, face-on and edge-on images of the fiducial galaxy at  $z = 0$  from [Stinson et al. \(2013b\)](#). Left panel, Rotation curves of the same galaxies when feedback recipes are varied (Early Stellar Feedback and feedback from SNs).

face density profiles). In Figure 3.2 we show their fiducial galaxy (left panel) and the change in rotation curves when changing feedback recipes.

To be noted that in the last years other groups have succeeded as well in reproducing realistic disc galaxies (see [Robertson et al. 2006](#), [Governato et al. 2007](#), [Agertz et al. 2011](#), [Guedes et al. 2011](#), [Brook et al. 2012](#), [Scannapieco et al. 2012](#), [Marinacci et al. 2013](#)), but all of these works on galaxy formation assumed a  $\Lambda$ CDM model.

Hydrodynamical simulations that will be presented in Section 4.2 extend the work done in [Stinson et al. \(2013b\)](#) to the case of dynamical dark energy. The implementation of the sub-grid feedback model is thus the same as in [Stinson et al. \(2013b\)](#), but the dark energy extension was implemented ([Casarini et al., 2011b](#)). Given that the dark energy field does not interact with any component other than through gravity, for GASOLINE-DE it was sufficient to modify the background evolution in which matter perturbations grow. Thus, the implementation consisted of allowing the code to accept the evolution of the Hubble function  $H \equiv \dot{a}/a$  as an external input, so that its value at each time step could be calculated with an interpolation of the input values.

### 3.2.2 GADGET2-CDE

The coupled dark energy model described in Section 1.4.2 and 2.1.1 was implemented in the N-body code GADGET2 ([Baldi et al., 2010](#)), which we here briefly summarize and refer to as GADGET2-CDE. As pointed out in the model section, the background evolution of constant coupling models is

---

characterized by a regime during matter domination where the two interacting fluids share a constant ratio of the total energy content of the universe. Thus, differently from the  $\Lambda$ CDM case, a non-negligible early dark energy fraction is present during structure formation, which in turn implies a different background evolution compared to the one in a  $\Lambda$ CDM model. As in the previous sections, an interpolation of the Hubble parameter  $H$  allows the code to model the correct expansion history. Furthermore, the same procedure is implemented also for the coupling function for cold dark matter  $\beta_c(\phi)$ , the correction term for dark matter masses  $\Delta m_{\text{DM}}$  and the parameter for the kinetic energy density of the scalar field  $\Omega_{\text{kin}}(\phi)$ . In fact, as showed in Eq. (1.47), dark matter particle masses change with time, thus they need to be corrected at each time step. Eq. (2.11) shows the acceleration felt by a dark matter particle. The extra term depending on the velocity of the particle is not present in  $\Lambda$ CDM and was implemented in terms of the velocity variable  $\vec{p} \equiv a(t)^2 \dot{\vec{x}}$  in the code, with  $\vec{x}$  comoving coordinates

$$\dot{\vec{p}}_i = \frac{1}{a} \left[ \beta_c(\phi) \frac{\dot{\phi}}{M} a \vec{p}_i + \sum_{i \neq j} \frac{\tilde{G}_{ij} m_j \vec{x}_{ij}}{|\vec{x}_{ij}|^3} \right], \quad (3.6)$$

where  $\tilde{G}_{ij}$  is the effective gravitational constant between the  $i$ -th and  $j$ -th particle, which is given in Eq. (2.10) and implemented in the code as

$$\tilde{G}_{ij} = G_{\text{N}} (1 + 2\beta_i \beta_j), \quad (3.7)$$

with  $i$  and  $j$  denoting the particle species (i.e. only DM-DM interaction will give an enhanced gravitational constant) and  $G_{\text{N}}$  is the Newtonian gravitational constant. Finally, also the multipole expansion of the tree algorithm had to be modified. In standard GADGET2 the gravity calculation is either computed on the whole node or the node is once more divided in other eight smaller nodes merely using the opening criterium, which sets the accuracy of approximating a distribution of particles with a more massive particle positioned in the distribution center of mass. In coupled dark energy models not all particles exert the same gravitational pull, thus one massive particle per each particle species in the respective centers of mass has to be accounted for.

GADGET-CDE has been used to investigate the formation of large scale structures and cluster of galaxies in follow up papers, Baldi (2011a,b); Baldi and Pettorino (2011); Baldi (2012a,b). In Figure 3.3 shows the dark matter density distribution in a slice with size  $1000 \times 250$  Mpc/h and thickness 30 Mpc/h from the CoDECS simulations (Baldi, 2012b). EXP003 and SUGRA003 are two coupled dark energy models chosen in his work. Given that all three cosmological models have the same  $\sigma_8$  at  $z = 0$ , there are still differences in the central densities of clusters. Despite the deep study carried out by Baldi et al., no high resolution multi-mass simulations have

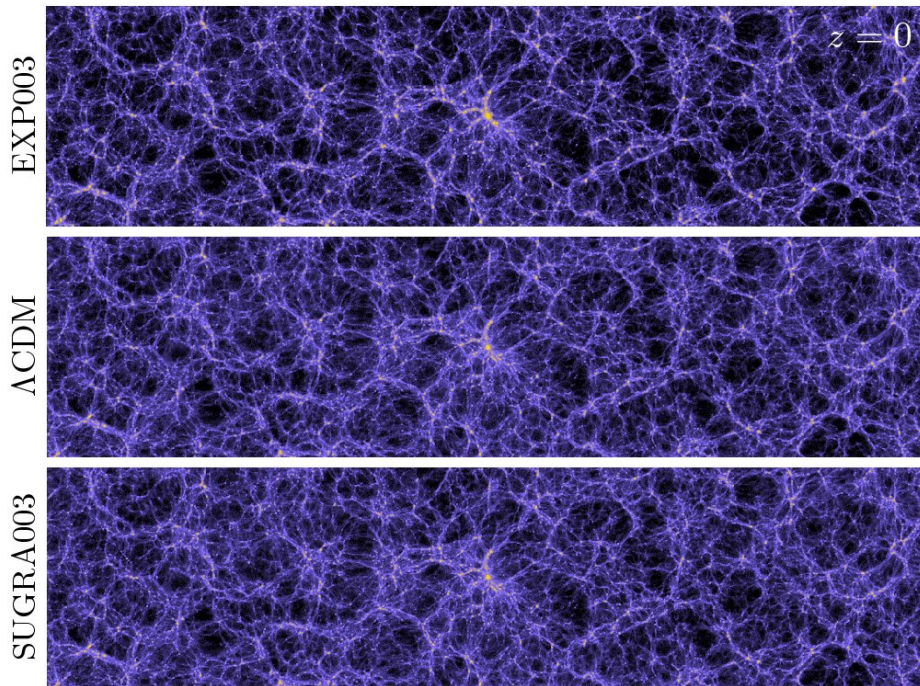


Figure 3.3: Dark matter density distribution in  $\Lambda$ CDM and two coupled dark energy models taken from [Baldi \(2012b\)](#).

been performed before this work. In Chapter 5 we present the first study of coupled dark energy on galactic and sub-galactic scales.

---

## Chapter 4

# Galaxy Formation in Dynamical Dark Energy

In this Chapter we investigate the effects of dynamical dark energy on the formation of galaxies via hydrodynamical numerical simulations. The cosmological model is outlined in Section 1.4.1 and 2.1.1 and more specifics will be given in the following sections.

Section 4.2 reports the results on high-resolution single-object simulations of three disc galaxies from Penzo et al. (2014). Here we study the role of baryons in differentiating dynamical dark energy models. In this work I produced initial conditions, ran the simulations and carried out the analysis with the supervision of A. V. Macciò. In Section 4.3 we performed hydrodynamical simulations of a large volume of the universe ( $L_{\text{box}} = 114$  Mpc). The aim is to test the effects of viable dark energy models across a wide range of galaxy masses, environments and merger histories. This Section is part of a work in preparation that is being carried out in collaboration with L. Casarini and A. Macciò, where L. Casarini performed the simulations and I worked on the analysis with the supervision of A. V. Macciò. To conclude, in Section 4.4 we investigate the effects of dynamical dark energy on satellite dwarf galaxies to then focus on the star formation stochasticity of these small mass systems in a  $\Lambda$ CDM scenario (A. V. Macciò, C. Penzo et al. in preparation).

### 4.1 Models

We choose four dynamical Dark Energy (dDE) models, each of which is consistent with WMAP7 data (Komatsu et al. 2011) at two sigma level, waCDM0, waCDM1, waCDM2 and SUCDM. All the models have at  $z = 0$ :  $\Omega_{b_0} = 0.0458$ ,  $\Omega_{DM_0} = 0.229$ ,  $H_0 = 70.2 \text{ km}^{-1} \text{ s}^{-1} \text{ Mpc}^{-1}$ ,  $\sigma_8 = 0.816$ ,  $n_s = 0.968$ , where these parameters are density parameters for baryons and dark matter, Hubble constant, root mean square of the fluctuation amplitudes and

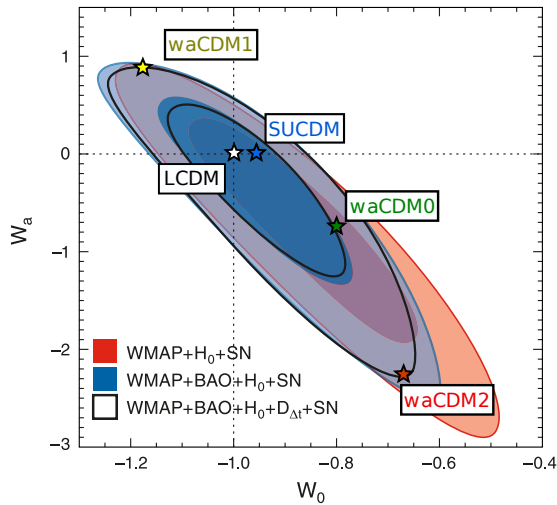


Figure 4.1: Two-sigma contours from WMAP7 in the  $w_a$ - $w_0$  plane from WMAP7. Each cosmological model is represented by a star.

	$w_0$	$w_a$
waCDM0 (green)	-0.8	-0.755
waCDM1 (yellow)	-1.18	0.89
waCDM2 (red)	-0.67	-2.28

Table 4.1: Parameters of the waCDM cosmological models

primeval spectra index. waCDM0, waCDM1 and waCDM2, are based on a linear CPL parametrization of the equation-of-state parameter  $w$  showed in Eq. (1.31). In Table 4.1 we present the values we chose for  $w_0$  and  $w_a$  in each of the three cases. In Figure 4.1 the two-sigma contours from WMAP7 in the  $w_a$ - $w_0$  plane are shown, and each cosmological model is represented by a star. waCDM0 is a model very close to LCDM as shown in Casarini et al. (2009a), while waCDM1 and waCDM2, already studied in Casarini et al. (2011a), are the most distant. Furthermore, we have included a fourth cosmological model, SUCDM, in which dark energy is described by a scalar field with a SUGRA self-interacting potential (see Section 1.4.1), where we chose  $\alpha = 2.9$  and  $M = 10$  GeV in agreement with Alimi et al. (2010). It is important to note that *all* of these models are *viable* models according to WMAP7 data. The blue star representing the SUCDM model is here shown only for comparison, but clearly its position on this plot holds only at  $z = 0$ , since its equation-of-state parameter  $w(a)$  cannot be described by the CPL parametrization.

In order to show how the background evolution changes between cosmological models, Figure 4.2 shows both expansion velocity (left panel) and

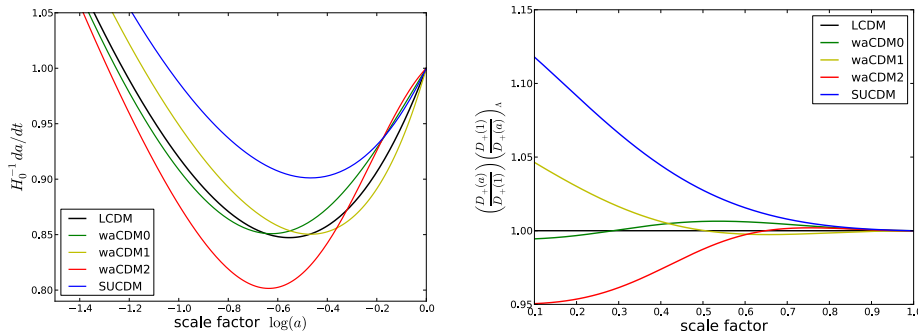


Figure 4.2: The left panel shows universe expansion velocities in units of the Hubble constant as a functions of the scale factor. The right panel shows the ratio of the growth factor at a given scale factor to the growth factor at  $a = 1$  divided by the same ratio for  $\Lambda$ CDM.

growth factor (right panel) as functions of the scale factor for each cosmology. Note that we chose to compare different cosmological models by normalizing them to the same  $\sigma_8$  today. With this choice, a model with a faster cosmic expansion will have to start producing structure earlier than a model with slower expansion. This means that statistically, the SUCDM model (blue lines) will show collapsed structures at an earlier epoch than the waCDM2 model (red lines), in order to compensate for the faster expansion of the universe. The earlier structure formation also leads to earlier accretion of the substructures onto the parent halo. In turn, we expect that earlier accretion will lead to earlier star formation in the simulated galaxies.

## 4.2 Disc Galaxies simulations in Dynamical Dark Energy

### 4.2.1 Introduction

In their pioneering dark-matter-only simulations with a dark energy equation of state evolving with time  $w(z)$ , [Klypin et al. \(2003\)](#) found that the differences between the cosmological models were not significant at  $z=0$  both in the non-linear matter power spectrum and in the halo mass function, although differences between models became significant at higher redshifts with a higher number of clusters for the dark energy models compared to  $\Lambda$ CDM.

Subsequently, multiple groups investigated the properties of dark matter structures in DE cosmologies; see, for instance, [Dolag et al. \(2004\)](#), [Bartelmann et al. \(2005\)](#), [Francis et al. \(2009\)](#), [Grossi and Springel \(2009\)](#). They studied halo concentrations, velocity dispersions, abundance relations and linear density contrast at collapse time in dark energy and early dark energy

---

models. Generally, significant differences between  $\Lambda$ CDM and dark energy cosmologies were found mostly at high redshifts (when the same value for the mean density amplitude  $\sigma_8$  at  $z=0$  was assumed).

Several studies compared the inner structure of haloes simulated in  $\Lambda$ CDM and dark energy cosmologies in collisionless simulations. In all cases, a Navarro-Frenk-White (Navarro et al., 1997) density profile well described the matter distribution. Furthermore, they found higher central concentrations in haloes simulated in a dark energy cosmology compared to those in  $\Lambda$ CDM, due to earlier formation times of haloes (Klypin et al. 2003; Linder and Jenkins 2003; Kuhlen et al. 2005).

It is important to note that, while these studies all considered dark energy cosmologies that featured an earlier collapse time than  $\Lambda$ CDM, it is also possible for dark energy cosmologies to form structure at a later stage than  $\Lambda$ CDM. This happens when the equation-of-state parameter,  $w(a)$ , “crosses over the cosmological constant boundary from below”. In other words,  $w$  can evolve from  $w < -1$  at high redshift to  $w > -1$  at  $z = 0$ . Such models have *less* collapsed structure at high redshift than  $\Lambda$ CDM (see Pace et al. 2012).

While it is useful, and surely computationally much cheaper, to study collisionless simulations of dark energy cosmologies, we can only directly observe baryons. Even though they account for  $\sim \frac{1}{5}$  of the mass density of dark matter in the universe, baryons can have a strong impact on the formation of small scale structures (White, 1976; Gallagher et al., 1984; Zhan and Knox, 2004; Puchwein et al., 2005; Jing et al., 2006; Maio et al., 2006; Rudd et al., 2008; Casarini et al., 2011c; De Boni et al., 2011; van Daalen et al., 2011; Casarini et al., 2012; Fedeli et al., 2012). So far, simulations including dark energy have focused on massive galaxy clusters since cosmology has the largest effect on the formation of the largest structures.

In the last decade different groups have been studying galaxy formation and evolution by performing high resolution hydrodynamical simulations in a cosmological context. Only recently they have succeeded in simulating realistic disc galaxies, e.g. star formation history matching with observational constrains, flat rotation curves, exponential surface density profiles (see Robertson et al. 2006, Governato et al. 2007, Agertz et al. 2011, Guedes et al. 2011, Brook et al. 2012, Scannapieco et al. 2012, Stinson et al. 2013b, Marinacci et al. 2013). In all of these high resolution simulations a  $\Lambda$ CDM cosmology has always been assumed. Recently an attempt to study galaxy formation in different cosmological models has been presented in Fontanot et al. (2012, 2013), where N-body simulations were combined with a Semi Analytical Model (SAM) for galaxy formation. SAMs use merger trees from dark matter only simulations and model the evolution of the baryonic component with approximate, yet physically motivated, analytical prescriptions. While Fontanot et al. (2012, 2013) were able to address the effect of cosmology on global properties of galaxies (e.g. the cosmic star formation), due to SAM’s limitations, they were not able to study the effects of Dark Energy

parametrization on the internal structure of simulated galaxies.

In this chapter we show the first detailed study of the effect of dark energy on galactic scale using high resolution hydrodynamical simulations for three different disc galaxies. Our study is an extension of the MaGICC project (Making Galaxies In a Cosmological Context) and we dubbed it DarkMaGICC. The MaGICC project uses GASOLINE2 (see Section 3.2.1) and has been quite successful in reproducing several properties of observed disc galaxies, including star formation rates and stellar masses (Brook et al. 2012; Stinson et al. 2013b), metals production and distribution (Stinson et al. 2012; Brook et al. 2013b), flat rotation curves and cored profiles (Macciò et al. 2012; Di Cintio et al. 2014) and disc properties as observed in the Milky-Way (Brook et al. 2013a; Stinson et al. 2013a).

We adopted the same set of numerical parameters describing the baryonic physics as in Stinson et al. (2013b), and perform high resolution hydrodynamical simulations with different dark energy backgrounds, to study the impact of dark energy on disc galaxy properties.

## 4.2.2 Results and Discussion

By using GRAFIC2-DE and GASOLINE-DE (see Section 3.1.1 and 3.2.1), we simulated three disc galaxies, gal $\alpha$ , gal $\beta$ , gal $\gamma$ , each of them in all five cosmological models. In Table 4.2 we summarize the main proprieties of the chosen three disc galaxies in  $\Lambda$ CDM, SUCDM and waCDM2 cosmologies. For all three galaxies the softening for gas and dark matter particles are respectively 0.45 and 1 kpc. Note that, for all galaxies, the SUCDM equivalents are always the most massive and, on the other hand, the waCDM2 are always the least massive. Using hydrodynamical and dark matter only simulations, in the next sections we present how gal $\alpha$ , gal $\beta$  and gal $\gamma$  evolved and their  $z = 0$  properties. These include dark matter distribution, gas, star and total halo masses, star formation histories, rotation curves, and the chemical enrichment of the galaxies.

### Stellar and Halo Mass

Figure 4.3 shows dark matter profiles for gal $\alpha$  in simulations with and without baryons for all different cosmological models; gal $\beta$  and gal $\gamma$  show similar results. The five radial density profiles from the dark matter only simulations (left panel) are almost indistinguishable. This confirms previous findings from N-body simulations, which showed that dark matter only simulations on galactic scales weakly depend on the dark energy model. The right panel of Figure 4.3 shows the radial density profiles of dark matter in hydrodynamical simulations. In contrast to the dark matter only simulations, the density profiles start differentiating with respect to the dark energy model used.

	$M_{\text{vir}}$ [ $M_{\odot}$ ]	$M_{\text{DM}}$ [ $M_{\odot}$ ]	$M_{\text{gas}}$ [ $M_{\odot}$ ]	$M_{\star}$ [ $M_{\odot}$ ]
gal $\alpha$				
$\Lambda$ CDM	$7.74 \times 10^{11}$	$6.76 \times 10^{11}$	$5.34 \times 10^{10}$	$4.52 \times 10^{10}$
SUCDM	$8.23 \times 10^{11}$	$7.12 \times 10^{11}$	$5.52 \times 10^{10}$	$5.62 \times 10^{10}$
waCDM2	$7.33 \times 10^{11}$	$6.46 \times 10^{11}$	$5.68 \times 10^{10}$	$3.07 \times 10^{10}$
gal $\beta$				
$\Lambda$ CDM	$5.65 \times 10^{11}$	$4.91 \times 10^{11}$	$3.48 \times 10^{10}$	$3.87 \times 10^{10}$
SUCDM	$5.70 \times 10^{11}$	$4.97 \times 10^{11}$	$2.84 \times 10^{10}$	$4.50 \times 10^{10}$
waCDM2	$5.45 \times 10^{11}$	$4.82 \times 10^{11}$	$3.47 \times 10^{10}$	$2.91 \times 10^{10}$
gal $\gamma$				
$\Lambda$ CDM	$3.44 \times 10^{11}$	$3.09 \times 10^{11}$	$2.76 \times 10^{10}$	$6.68 \times 10^9$
SUCDM	$3.65 \times 10^{11}$	$3.24 \times 10^{11}$	$2.82 \times 10^{10}$	$1.33 \times 10^{10}$
waCDM2	$3.35 \times 10^{11}$	$3.02 \times 10^{11}$	$2.69 \times 10^{10}$	$5.77 \times 10^9$

Table 4.2: Physical properties of the three disc galaxies in  $\Lambda$ CDM, SUCDM and waCDM2. We show virial mass (total mass), dark matter mass, gaseous mass and stellar mass, all calculated within one virial radius.

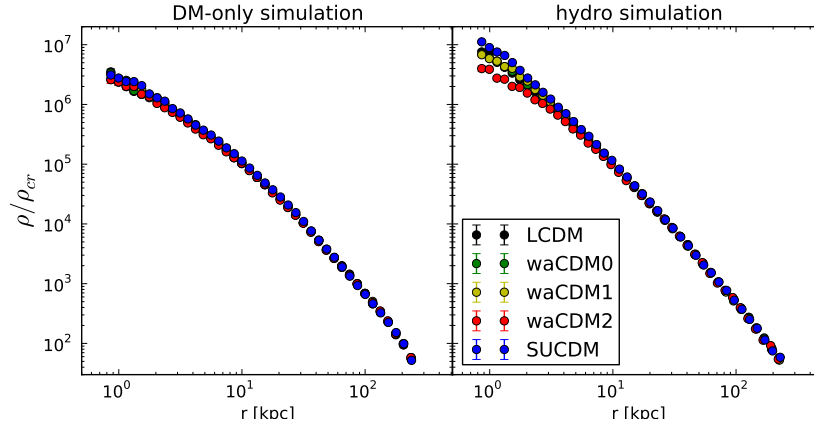


Figure 4.3: Dark matter density profiles of gal $\alpha$  simulated in all five cosmological models, respectively in a dark matter only (left panel) and in a hydrodynamical simulation (right panel). We plot the density in units of critical density, as a function of the distance from the center of mass of the galaxy.

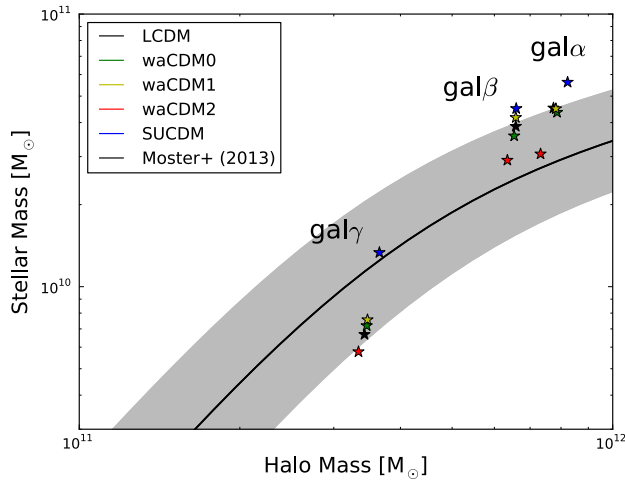


Figure 4.4: Values for stellar mass and halo mass at  $z = 0$ . Each star represents a galaxy in a given cosmological model. The solid black line shows the prediction from observational constraints and the shaded area its  $2\sigma$  errors.

Figure 4.4 sets  $\text{gal}\alpha$ ,  $\text{gal}\beta$  and  $\text{gal}\gamma$  in the abundance matching plot at  $z = 0$ . The abundance matching technique relates the galaxy luminosity function at each epoch of interest to the dark matter halo and subhalo mass function from N-body simulations. Galaxies are ranked by luminosity and haloes by mass and matched one-to-one, so that lower luminosity galaxies are associated with haloes of lower mass, and galaxies above a given luminosity threshold are assigned to haloes above a given mass threshold with the same abundance or number density. Throughout this work we will compare our simulations with the abundance matching predictions from [Moster et al. \(2013\)](#), represented in Figure 4.4 by the black line. The shaded area represents the errors on the prediction. The abundance matching prediction does not vary from  $\Lambda$ CDM to the other cosmologies since it is calculated using the value for  $\sigma_8$  at  $z = 0$ , and all our cosmological models share the same value. While statistical conclusions are not possible because of the limited sample, the three galaxies do show the same trend as a function of cosmology. By simply varying the cosmological model, the change among the three galaxies is of only a few percent in the dark matter mass, while the stellar mass almost doubles. Galaxies simulated in the waCDM2 cosmology (red symbols) always make the least stars at  $z = 0$ , while the galaxies formed in the SUCDM cosmology (blue symbols) always make the most stars. As expected, galaxies formed in a  $\Lambda$ CDM cosmology always lie in the middle. The hierarchy is in agreement with the behaviors of the cosmological background evolutions of these cosmological models (see Figure 4.2 and Section 4.1), since we expect more structures to be formed in a cosmological model that

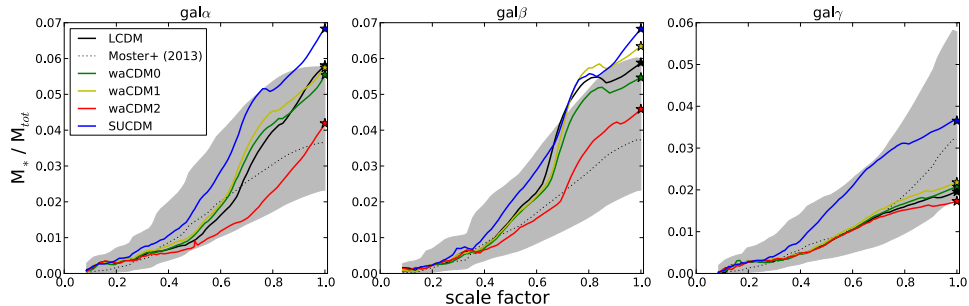


Figure 4.5: Evolutions of the stellar-halo mass relation as a function of scale factor for  $\text{gal}\alpha$ ,  $\text{gal}\beta$  and  $\text{gal}\gamma$ .

begins forming structures earlier.

### Evolution of the stellar-halo mass relation

Figure 4.5 shows how the ratio of stellar mass and total mass evolve with scale factor  $a = 1/(z + 1)$ . Each panel relates to a specific galaxy and the different colors describe each galaxy run in a different cosmology. Again, the black solid line represents the expected evolution for a  $\Lambda$ CDM model using the abundance matching technique. The predicted evolutions do change with the change in cosmology, but they all do not distance themselves significantly from the  $\Lambda$ CDM prediction. Hence, out of clarity, we have only plotted the  $\Lambda$ CDM predicted behavior from abundance matching. As in the  $z = 0$  case, the stellar-halo mass trends for the galaxies simulated in different cosmologies are in agreement with the evolution of their cosmological backgrounds. In the SUGRA cosmology (blue lines), we expect higher density perturbations to compensate for the faster expansion of the universe. These higher density perturbations trigger a more efficient star formation. This is in agreement with previous works on SUCDM cosmology (e.g. Zhan and Knox 2004; Puchwein et al. 2005; Jing et al. 2006; Maio et al. 2006; Rudd et al. 2008; Casarini et al. 2011c; De Boni et al. 2011; van Daalen et al. 2011; Casarini et al. 2012; Fedeli et al. 2012).

On the contrary, the waCDM2 galaxy (red lines) always makes less stars throughout its evolution. The cosmological models waCDM0 and waCDM1 are not far apart from the  $\Lambda$ CDM model, in the  $w_a - w_0$  plane, thus we would expect galaxies that live in those models not to differ greatly from galaxies that live in the  $\Lambda$ CDM universe. This expectation is nicely reproduced for all three haloes.

As shown in Figure 4.5, it is noticeable how both  $\text{gal}\alpha$  and  $\text{gal}\beta$  undergo a significant merger around  $a = 0.8$  which raises their star formation efficiency and increases their dark matter mass. The merger is visible also from the dark matter mass of the haloes as a function of the scale factor. Figure 4.6

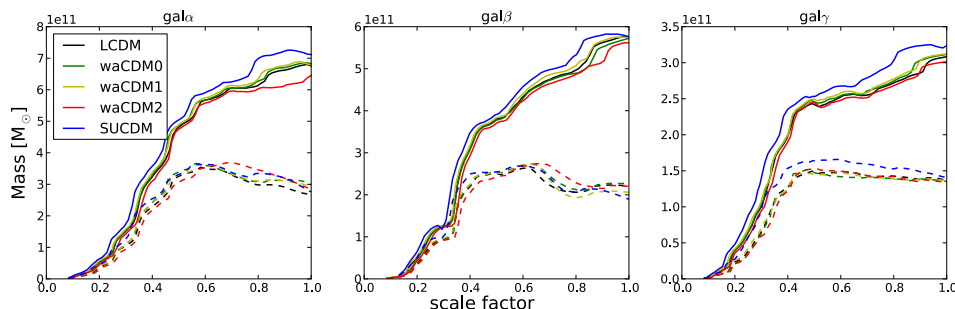


Figure 4.6: Evolution of the dark matter mass (solid lines) and gas mass (dashed lines) for  $\text{gal}\alpha$ ,  $\text{gal}\beta$  and  $\text{gal}\gamma$  in all different cosmological models. For an easier comparison, the gas mass was increased of a factor of five.

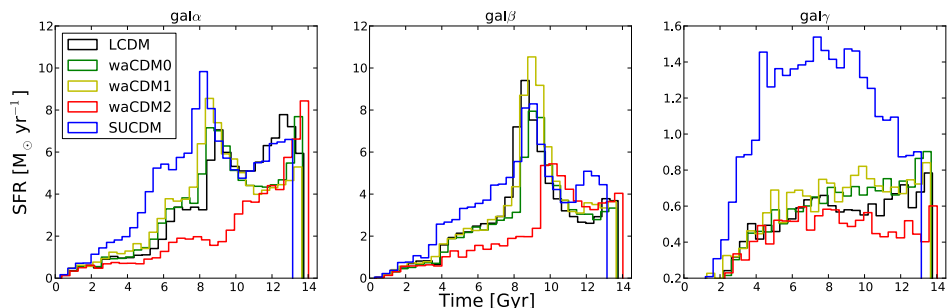


Figure 4.7: Star formation histories for  $\text{gal}\alpha$ ,  $\text{gal}\beta$  and  $\text{gal}\gamma$  in all the cosmological models.

shows a clear increase in the dark matter mass due to the accretion of a nearby satellite galaxy.

### Star Formation Histories

Figure 4.7 shows the star formation rate (SFR) as a function of physical time. Different cosmological models show longer or shorter ages of the universe because how much physical time elapses as the universe expands depends on the cosmology. The choice of showing the star formation in standard physical units is made to give more insight. Figure 4.7 shows how dark energy can suppress and delay star formation. Interestingly,  $\text{waCDM2}$  cosmology (red lines) *delays* star formation, both in the case of  $\text{gal}\alpha$  and  $\text{gal}\beta$ . In all three galaxies the  $\text{waCDM2}$  cosmology drastically *suppresses* star formation until recent times.

As pointed out, both  $\text{gal}\alpha$  and  $\text{gal}\beta$  undergo a merger. The merger event is clearly marked by the presence of a peak in the SFRs between 7 and 10 Gyr (notice how the peak shifts in time according to the cosmological model). After the star formation burst due to the merger, both galaxies decrease

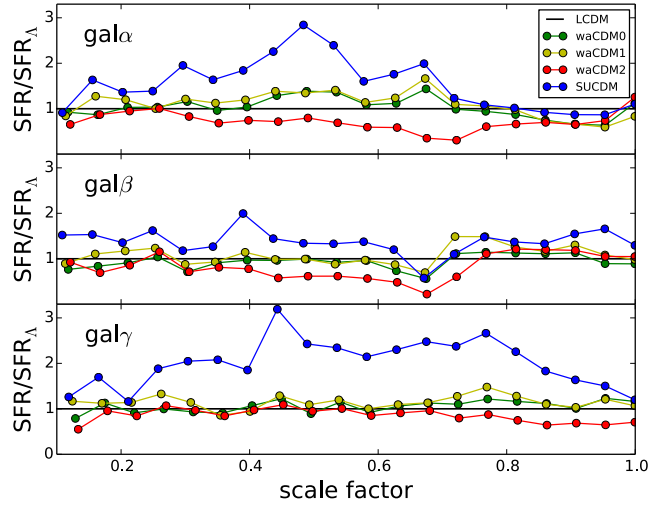


Figure 4.8: For each galaxy we show the ratio of  $\text{SFR}/\text{SFR}_\Lambda$  (Star Formation Rate) for all cosmological models as a function of scale factor. The top panel shows  $\text{gal}_\alpha$ , the middle panel  $\text{gal}_\beta$  and the bottom panel  $\text{gal}_\gamma$ .

their star formation activity due to the decrease in the amount of available cold gas. This is shown in Figure 4.6, where we plot the evolution of the dark matter mass and the cool gas mass ( $T < 10^5$  K).

In order to compare the effects of dynamical dark energy on galaxies with different masses, in Figure 4.8 we show for each galaxy the ratio of the star formation rate in a given cosmology and the star formation rate in  $\Lambda\text{CDM}$  ( $\text{SFR}/\text{SFR}_\Lambda$ ) for all cosmological models as a function of scale factor to more easily compare with Fontanot et al. (2012). Fontanot et al. used semi-analytic models to investigate differences in cosmic star formation in dynamical dark energy cosmologies. They find a larger difference between cosmological models at high redshifts. In our case the contribution of cosmology seems not to change significantly with redshifts. The reason for this apparent inconsistency is that, while we are looking at the evolution of an individual object, Fontanot et al. looked at the evolution of an entire population of galaxies. Clearly, the effect of dark energy on a single halo has to be convolved with the evolution of the mass function itself. Convolution of the two components explains the stronger redshift evolution seen in Fontanot et al.. To this stage, we note that, given our limited sample, the effect of dark energy seems not to have a trend with the mass of the galaxy (taken into account cosmic variance).

### Rotation Curves

Different star formation histories reflect different matter distributions among the galaxy, as the rotation curves in Figure 4.9 show. Galaxies with delayed

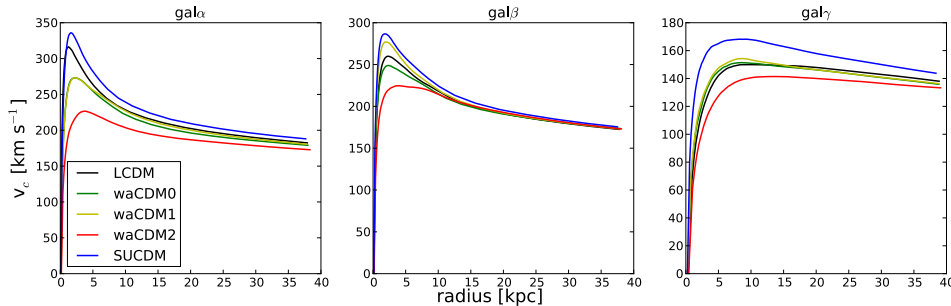


Figure 4.9: Rotation curves for  $\text{gal}\alpha$ ,  $\text{gal}\beta$  and  $\text{gal}\gamma$  in all cosmological models.

star formation (waCDM2 cosmology, red lines in Figure 4.7) have flatter rotation curves than galaxies where star formation started earlier (SUCDM cosmology, blue lines), see [Stinson et al. 2013b](#). Thus, a galaxy can have a flat or centrally peaked rotation curve based simply on the background cosmology in which it forms. Centrally peaked rotation curves have long been the prime symptom of the overcooling problem in disc galaxy formation simulations ([Scannapieco et al., 2012](#)). In the centers of haloes the gas density becomes high enough that hot gas starts radiating and consequently cools. In such environments, the cooling process is unstable because, once the hot gas has cooled, it no longer pressure supports the surrounding gas, which then becomes denser and cools. Stars then form in excess and primarily in the central concentration, and they produce peaked rotation curves. Most solutions have focused on adding energy from stars or AGN ([Scannapieco et al. 2012](#)). [Stinson et al. \(2013b\)](#) showed one solution based on stellar winds from massive stars (i.e. “early stellar feedback”). Our results show that also cosmology can have a considerable effect on flattening rotation curves. This work shows that *simply* changing the evolutions of the dark energy equation of state *flattens* rotation curves of a considerable and definitely *observable* amount (i.e. more than 100 km/s in both  $\text{gal}\alpha$  and  $\text{gal}\beta$ ). Figure 4.10 compares rotation curves for  $\text{gal}\alpha$  in dark matter only simulations (left panel) and in SPH simulations (right panel) for each cosmological model. The change is striking. While in the dark matter only case the cosmological models are almost indistinguishable, they become clearly distinguishable in the hydrodynamical simulations and they vary of an observable amount.

### Feedback and Cosmology, Metallicity Interplay

We showed that a model whose universe velocity expansion is slower compared to the one of  $\Lambda$ CDM (e.g. waCDM2, red lines) has a lower star formation till much later times, and on the other hand a model whose universe velocity expansion is faster than  $\Lambda$ CDM (e.g. SUCDM, blue lines) has a

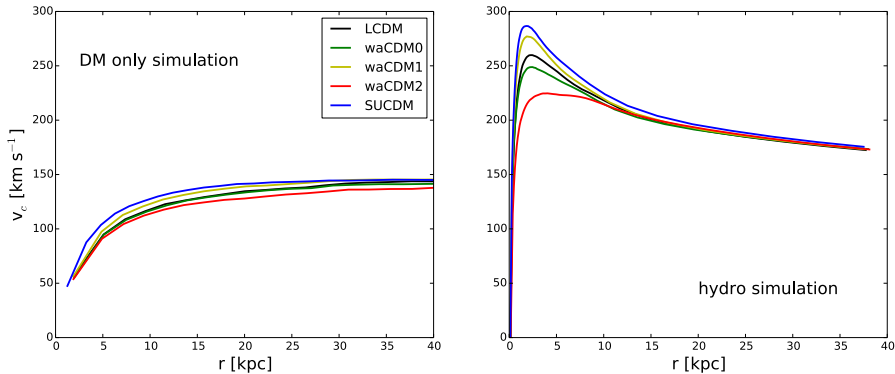


Figure 4.10: Rotation curve for  $\text{gal}\alpha$  in all different cosmological models, respectively in a dark matter only simulation (left panel) and in a hydrodynamical simulation (right panel).

higher star formation at all redshifts (see Figure 4.7). We can trace back this difference to the fact that all five different cosmological models have the same  $\sigma_8$  today, because, in order for this to happen, structures in a SUCDM model (blue lines) have to start forming earlier. This implies that, at the starting redshift ( $z = 99$  for all simulations), density perturbations that seeded structure formation had to be slightly bigger in the SUCDM model (blue lines) compared to the initial density perturbations in the waCDM2 model (red lines). Thus, stars will start forming earlier since more gas is accreted and cools. These differences in the initial perturbations do not significantly affect properties of structures on galactic scales in dark matter only simulations. On the other hand, the interplay between cooling, metallicity and star formation not only helps differentiating between the cosmological models but also enhances their differences. To highlight the “positive feedback” that star formation has on radiative cooling through metal enrichment, Figure 4.11 shows the evolution of metallicity as a function of scale factor for three different regions of  $\text{gal}\alpha$  and  $\text{gal}\beta$ , a central 2 kpc sphere (“bulge”), a disc cylinder with radius 20 kpc and 6 kpc thickness (“disc”), and a sphere of the size of the  $R_{vir}$  (“halo”). The waCDM2 model (red lines) exhibits the lowest metallicity in the bulge and disc throughout its evolution, which reflects its lower star formation rate and hence lower enrichment rate. The effect of increased metal enrichment is non-linear: the more star formation enriches gas, the faster the gas cools, and the more stars that subsequently form.

The halo metallicity of waCDM2 is also lower throughout most of the galaxy evolution, but becomes higher after  $a \sim 0.75$ , as its mean halo metallicity continues increasing while the metallicity in the other models starts to decrease or flatten out at that time. Both waCDM2 galaxies start to have more metallicity in the halo due to Supernova explosions being able to move

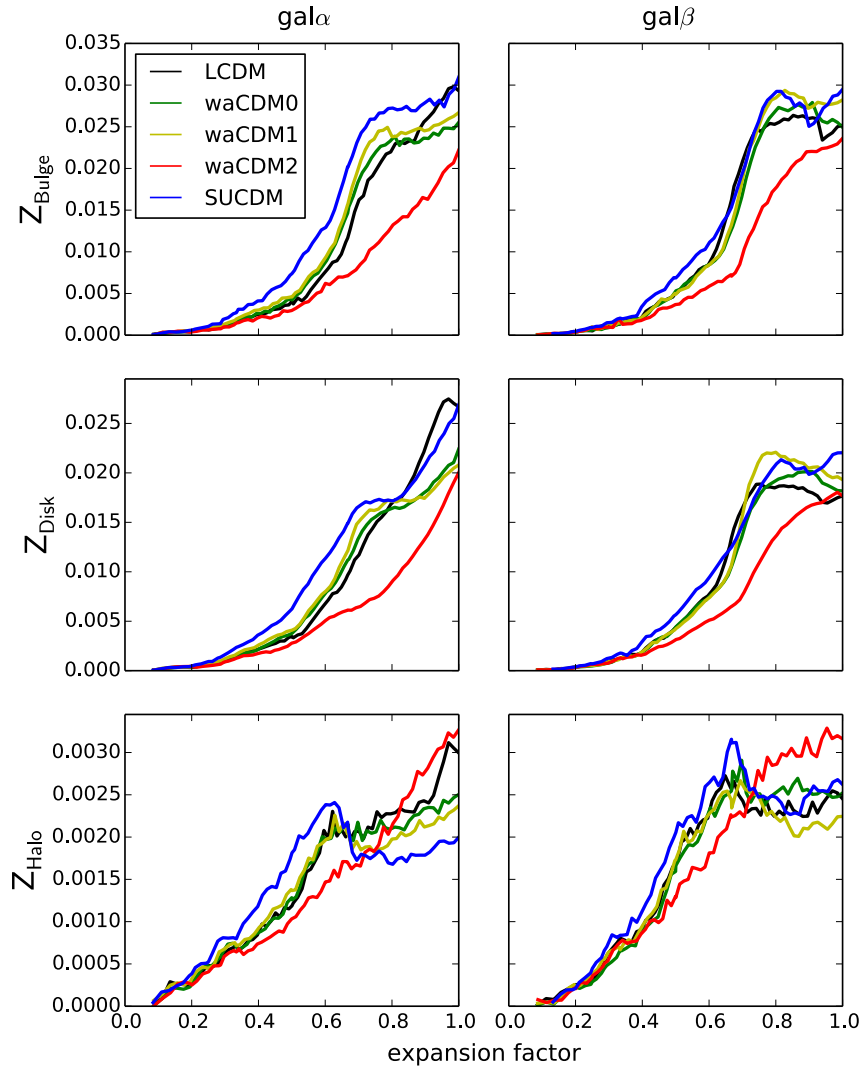


Figure 4.11: Mean metallicity in solar units for  $gal_\alpha$  and  $gal_\beta$  as function of scale factor in “bulge”, “disk” and “halo”. Different colors represent different cosmological models.

---

the gas outside from the disc.

Comparing the trends for metallicity (Figure 4.11), cool gas (Figure 4.12) and star formation rates (Figure 4.7) as functions of scale factor, we find them in agreement. Because of the lower metallicity, the  $\Lambda$ CDM2 model (red lines) ends up having the least amount of gas that has been able to cool and thus also makes the least amount of stars. Having used up a smaller amount of cold gas at earlier times increases the amount of cold gas left for star formation at late times. The presence of cool gas that has yet not formed stars can be seen in Figure 4.12, where after  $a = 0.7$  the disc of the  $\Lambda$ CDM2 galaxy has the most amount of cool gas compared to the galaxies in the other cosmological models. This is also the case for the galaxy halo, and this is probably due to the cooled gas moved by supernova explosions.

### Feedback–Dark Energy Degeneracy

Along with dark energy having a profound effect on disc galaxy evolution, galaxy formation strongly depends on how feedback is modeled. The effects of suppressing star formation, and hence flattening rotation curves, can also be obtained by varying the feedback sub-grid recipes. As shown in [Stinson et al. \(2013b\)](#), pre-supernova feedback from massive stars significantly suppresses star formation, which is the same effect seen in the dark energy model that has the most delayed expansion ( $\Lambda$ CDM2). For this reason, we wish to explore whether dark energy or stellar feedback have a greater effect in suppressing star formation and whether their effect changes with redshift.

We select the  $\Lambda$ CDM2 cosmology (red lines in previous plots), which showed the most star formation suppression and delay, and we re-simulate it with a range of stellar feedback strengths. We vary both the supernova feedback efficiency and the early stellar feedback separately. First, the early stellar feedback is turned from 10% down to 0% efficiency with the standard  $10^{51}$  erg of supernova energy. Then, with no early stellar feedback, the supernova feedback strength is increased to 120% and 150%.

The left panel of Figure 4.13 shows each of these variations implemented in the  $\Lambda$ CDM2 model for  $\text{gal}\alpha$ . The stellar mass evolution shows a strong dependence on the early stellar feedback parameter. A decrease of 25% to 7.5% increases the final stellar mass 50% and moves most of the star formation from late to early times. All the simulations with less than 7.5% efficiency, but more than 0 early stellar feedback end with nearly the same final stellar mass. What is somewhat surprising is that the simulation with no early stellar feedback ends with *less* stellar mass than these intermediate feedback models. [Stinson et al. \(2013b\)](#) also saw this effect and found that it was due to the higher star formation efficiency at early times driving stronger outflows due to the greater supernova feedback. Thus, gas was driven to radii where it could not be re-accreted, whereas the early stellar feedback does not drive gas so far away.

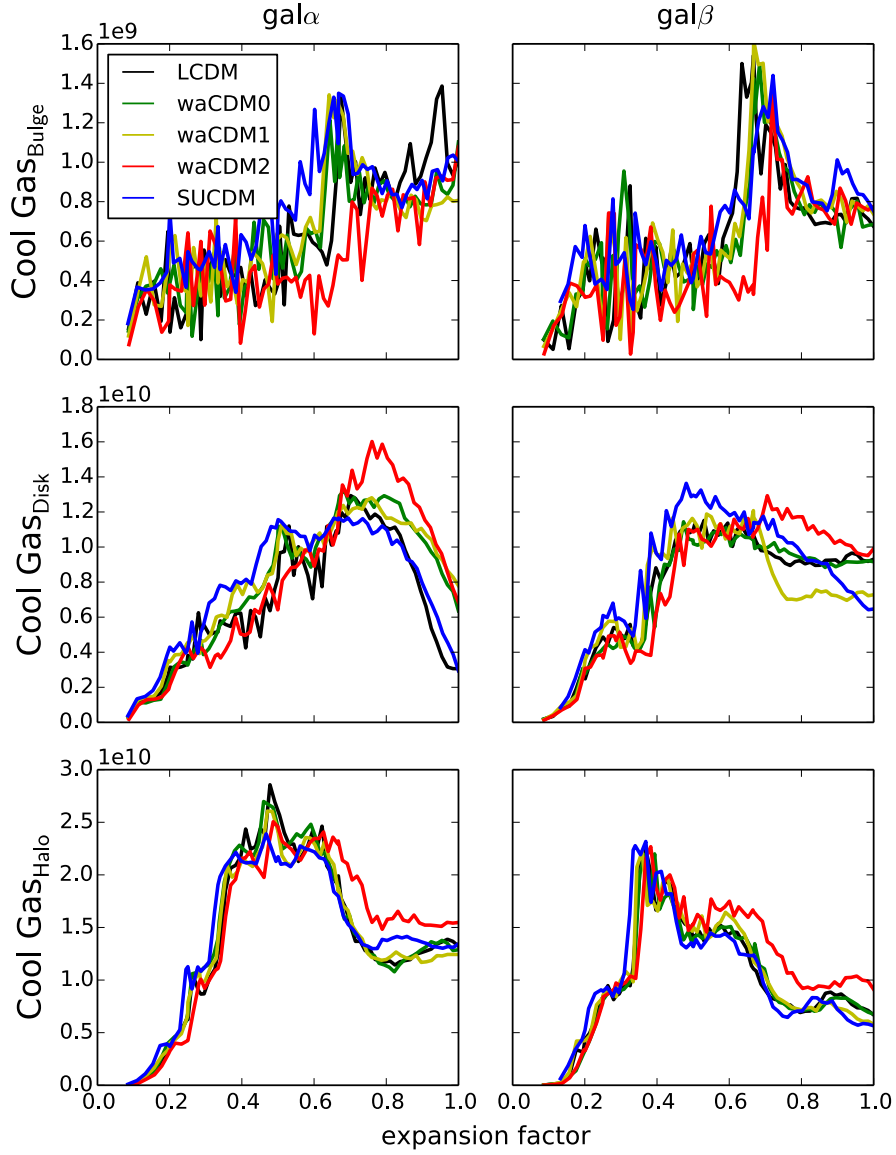


Figure 4.12: Cool gas in solar masses ( $T < 10^5\text{K}$ ) for gal $\alpha$  and gal $\beta$  as function of scale factor in “bulge”, “disc” and “halo”. Different colors represent different cosmological models.

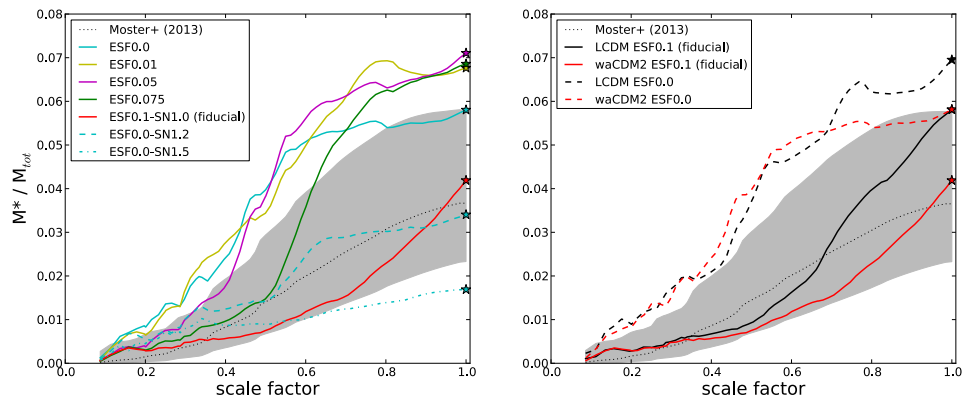


Figure 4.13: Evolution of stellar-halo mass relation with scale factor. We are now showing only the case of  $gal\alpha$ . In the left panel we have changed the feedback parameters for the waCDM2 run. We have increased the early stellar feedback parameter (ESF) from zero to the fiducial value (see [Stinson et al. \(2013b\)](#)) while keeping the SN parameter fixed to the fiducial value of 1.0 (solid lines). We then have changed the supernova parameter (SN) while keeping the early stellar feedback fixed to zero (dashed and dash-dotted cyan lines). The dotted black line is the abundance matching prediction from [Moster et al. 2013](#) and the shaded area its  $2\sigma$  contours. In the right panel we compare the effect of early stellar feedback feedback with the effect of different cosmology,  $\Lambda$ CDM (red and black lines) and waCDM2 (blue and red).

Supernova feedback unambiguously decreases the amount of stars formed throughout the galaxy’s evolution, but can easily push the trends out of the expected behaviors from abundance matching techniques suggesting that Supernova feedback alone is not enough to reproduce realistic galaxies.

The right panel of Figure 4.13 shows a comparison of the stellar mass-halo mass evolution of the  $\Lambda$ CDM2 model (red lines) with the  $\Lambda$ CDM model (black lines) for  $\text{gal}\alpha$ . The models separate most notably at late times. The corresponding simulations with no early stellar feedback are shown in the dashed lines. They clearly show that both cosmology and pre-SN feedback have a strong effect in suppressing star formation, but while pre-SN feedback has the strongest effect at high redshift, cosmology has the strongest effect more recently (i.e. after  $a = 0.7$ ).

The degeneracy between feedback and dark energy parametrizations certainly cannot be disentangled with our limited sample of galaxies, on the other hand Fontanot et al. (2013) pointed out that a possible way to put constraints on dynamical dark energy models would come from future missions, when we will be able to have more sensitivity at high redshifts.

### 4.2.3 Conclusions on Disc Galaxies simulations in Dynamical Dark Energy

The intention of this work was to investigate for the first time the effect of dark energy on galactic scales in SPH simulations. We find that the dark energy modeling has an unexpected significant effect on disc galaxy formation, on the contrary of what is most commonly believed.

The experiment used a suite of SPH multi-mass cosmological simulations with masses of  $3.4 \times 10^{11} M_{\odot}$ ,  $6.6 \times 10^{11} M_{\odot}$  and  $7.7 \times 10^{11} M_{\odot}$ , in four dynamical dark energy models plus the reference  $\Lambda$ CDM model. The models all employed the *same* baryonic physics prescriptions. All dynamical dark energy models are within the two sigma contours given by WMAP7. We examined the dark matter distribution, gas, star and total halo masses, star formation histories, rotation curves and the chemical enrichment of the galaxies.

Changing the dark energy evolution implies changing the expansion rate of the universe, which in turn affects the accretion history. We show how the same galaxy evolved in different dark energy cosmologies does not present significant differences in dark matter only simulations, while in hydrodynamical simulations the galactic properties change greatly.

At  $z = 0$ , the stellar mass inside one virial radius can vary by a factor of 2 depending on cosmology, while the dark matter mass only changes of a few percent. Thus baryons amplify differences between dark energy models, as the evolution of the stellar mass - halo mass ratio shows: by simply changing the dark energy parametrization stellar mass either decreases or increase of a factor of two throughout the whole galaxy evolution.

---

The reason why baryons amplify the differences among the various dynamical dark energy models lies on the non linear response of the hydrodynamical processes. Once the cosmological model introduces slightly different density perturbations, feedback processes enhances those differences by producing slightly more (or less) stars. More stars introduce more metals in the feedback cycle and more metals decrease the cooling time, which in turn allows gas to cool faster and produce even more stars. Through the highly non-linear response of baryons, dark energy models that would have been indistinguishable from  $\Lambda$ CDM on galactic scales show distinctive features in SPH simulations.

The distinctive features of dynamical dark energy become clear when looking at the star formation rates. We find that certain dark energy models are able to both delay and suppress star formation until recent epochs. The delay in star formation is then in turn responsible for the flattening of rotations curves, where we show a change of about 100 km/s in the two most massive galaxies we considered.

Finally we compare the effect of dynamical dark energy with the effect of baryonic feedback. We keep the cosmology fixed (waCDM2) and change the feedback parametrization. Provided that the Supernova feedback is kept constant, at late times the effect of dark energy is comparable to the effect of early stellar feedback (see Section 3.2.1 for details on feedback modeling). Even the degree at which stellar feedback is able to flatten rotation curves, is comparable to the effect of dark energy. We noted on the other hand, that in order to obtain the behavior suggested by abundance matching considerations at high redshifts, early stellar feedback had to be introduced since at high redshifts it has the most important effect compared to the dark energy modeling.

Having shown that the dark energy modeling has an important effect on disc galaxy formation and evolution, we would like to stress on the fact that, especially in the era of high precision cosmology, the details on dark energy do matter and certainly need further investigations.

## 4.3 Hydrodynamical Cosmological Volumes in Dynamical Dark Energy

### 4.3.1 Introduction

In Section 4.2 we have investigated high resolution single-object simulations of galaxies. Despite the multi-mass technique being an extremely useful tool to reach high resolutions and minimize the computational costs, only some tens of objects can be usually simulated. Recently, Wang et al. (2015) were able to build a larger  $\Lambda$ CDM set of single-galaxy simulations, which accounts for 100 objects. When aiming at describing the behavior of a signif-

icant distribution of galaxies ( $\sim$  thousands of objects at least), single-object simulations can no longer be employed.

In this Section we will present hydrodynamical simulations of a large volume of the universe ( $L_{\text{box}} = 114$  Mpc) in the dynamical dark energy models described in Section 4.1. The aim is to test the effects of viable dark energy models across a wide range of galaxy masses, environments and merger histories. Our work is an extension of Kannan et al. (2014), where they investigated the effectiveness of the feedback implementation as part of the MaGICC project in a  $\Lambda$ CDM cosmology. In our case, we adopted the sub-grid model for feedback proposed in Stinson et al. (2013b) and discussed in Section 3.2.1 and we varied the dark energy equation of state. These are the first fully hydrodynamical simulations of a significant volume of the universe in non- $\Lambda$ CDM cosmologies. This type of simulations treats hydrodynamics in the entire box and all particles of each type have the same mass. Previous studies have either been dark matter only (Klypin et al., 2003; Dolag et al., 2004; Bartelmann et al., 2005; Francis et al., 2009; Grossi and Springel, 2009; Li et al., 2012) or adiabatic hydrodynamical simulations, i.e. no gas cooling (Baldi, 2012b; Carlesi et al., 2014).

Nowadays we can rely on large catalogues describing the galactic population in the local universe (Kajisawa et al., 2010; Karim et al., 2011; Santini et al., 2012). These set observational constraints to statistical properties of galaxies and can be used to determine whether the implemented sub-grid modeling is able to accurately describe galaxy formation processes. Most importantly, data constrain the galaxy Stellar Mass Function (SMF), namely the number density of galaxies as a function of their stellar mass.

In the following Section we show results related to the cosmological volumes in different dynamical dark energy models. We focus on the effects of resolution compared to the multi-mass simulations described in Section 4.2 and finally we determine whether these cosmological models can be constrained by recent observations. This work has been part of a collaboration with L. Casarini, who is responsible for running the simulation set. I carried out the analysis with the supervision of A. V. Macciò.

### 4.3.2 Numerical and Cosmological Settings

We simulate a cosmological volume  $(114 \text{ Mpc})^3$ , starting at redshift  $z = 99$ . Initial conditions were created with GRAFIC2-DE (see Section 3.1.1) using the cosmological parameters from Section 4.2, i.e. at  $z = 0$ :  $\Omega_{b_0} = 0.0458$ ,  $\Omega_{DM_0} = 0.229$ ,  $H_0 = 70.2 \text{ km}^{-1} \text{ s}^{-1} \text{ Mpc}^{-1}$ ,  $\sigma_8 = 0.816$ ,  $n_s = 0.968$ , where these are density parameters for baryons and dark matter, Hubble constant, root mean square of the fluctuation amplitudes and primeval spectra index.

We have two sets of simulations, a higher resolution case (HR) with  $512^3$  particles and a lower resolution case (LR) with  $256^3$  particles. In both cases we simulated both a hydrodynamical and a dark matter only box (in the

---

hydrodynamical simulations the particle number doubles for both resolutions, accounting for dark matter and gas particles). For the HR simulations, due to the very high computational time ( $\sim$  six months), we selected  $\Lambda$ CDM, waCDM0 and SUCDM cosmologies, while we are running the LR in all cosmological models. In the HR case, the dark matter particle mass is  $3.5 \times 10^8 M_\odot$  and the initial gas particle mass and initial star particle mass are  $6.9 \times 10^7 M_\odot$  and  $2.3 \times 10^7 M_\odot$ . The softening for dark matter particles is 3.7 kpc, while for gas and stellar particles is 2.17 kpc. In the LR case, the dark matter particle mass is  $2.8 \times 10^9 M_\odot$  and the initial gas particle mass and initial star particle mass are  $5.6 \times 10^8 M_\odot$  and  $1.9 \times 10^8 M_\odot$ . The softening for dark matter particles is 7.4 kpc, while for gas and stellar particles is 4.34 kpc.

We used the code GASOLINE2-DE for all hydrodynamical simulations and PKDGRAV for the dark matter only runs. To identify haloes in each snapshots we used the Spherical Overdensity (SO) algorithm (Macciò et al., 2008).

### 4.3.3 Results and Discussion

#### Halo Mass Function

In the  $\Lambda$ CDM LR dark matter only volume ( $256^3$  particles) we find about 4 000 halos with more than 100 particles at  $z = 4$  and about 19 000 at  $z = 0$ . While, in the  $\Lambda$ CDM HR dark matter only volume ( $512^3$  particles) we find about 63 000 halos with more than 100 particles at  $z = 4$  and 117 000 at  $z = 2$  (our lowest redshift).

In Figure 4.14 and 4.15, for the  $256^3$  and  $512^3$  sets respectively, we show the ratio of halo mass functions to the  $\Lambda$ CDM case, namely the number density of haloes as a function of their halo mass in the dark matter only simulations. We choose not to include error bars since we are showing the mass function ratio. Calculating the error propagation on the ratio (where we would use the Poisson relative error  $1/\sqrt{N}$  with  $N$  number counts) makes the ratio error bar depend on the ratio value itself, which in turn would not give direct insight on the number of halos present in our analysis. Instead, we give details on our Milky-Way-like sample in  $\Lambda$ CDM cosmology for general guidelines. In the LR  $\Lambda$ CDM run we count about 2 000 halos with masses in the range  $11.8 < \log(M_{\text{halo}}) < 12.2$  at  $z = 4$  and about 8 600 at  $z = 0$ . In the HR  $\Lambda$ CDM run we count again about 2 000 halos with  $11.8 < \log(M_{\text{halo}}) < 12.2$  at  $z = 4$  and about 6 400 at  $z = 2$ .

Figure 4.14 and 4.15 show that the volume simulated in SUCDM cosmology features the highest number of haloes at higher redshifts. This is the consequence of the choice of normalization, namely, all simulations have the same  $\sigma_8$  at  $z = 0$ . Thus, having SUCDM a faster universe expansion compared to the  $\Lambda$ CDM case, it must have an earlier formation of structures to reach the same  $\sigma_8$  at  $z = 0$  than  $\Lambda$ CDM (see the evolutions of  $D_+$

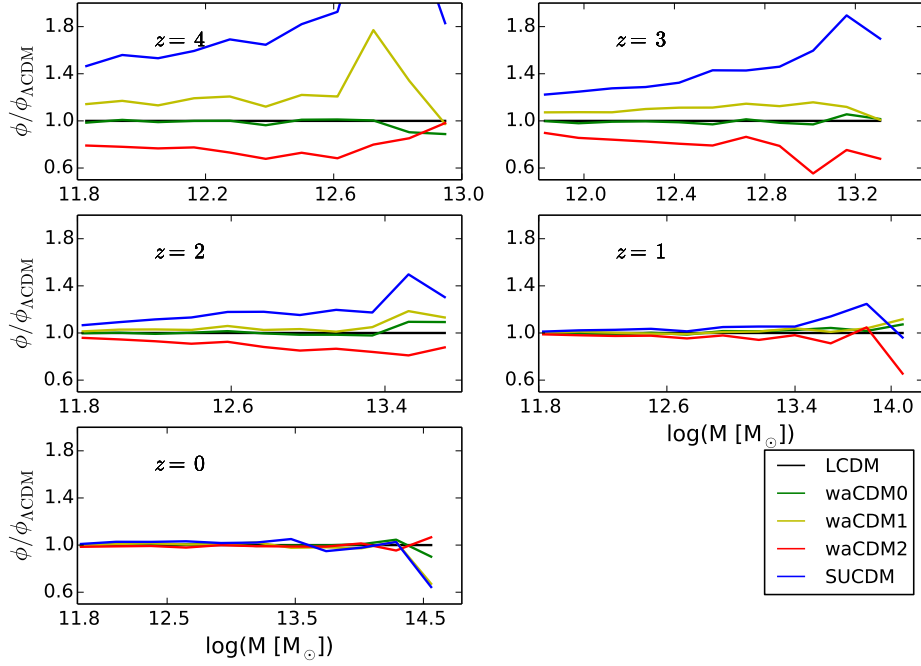


Figure 4.14: Ratio of the halo mass functions in different cosmologies to the halo mass function in the  $\Lambda\text{CDM}$  case for the LR dark matter only simulations ( $256^3$ ). We show snapshots at redshifts  $z = 4, 3, 2, 1, 0$  in the different panels.

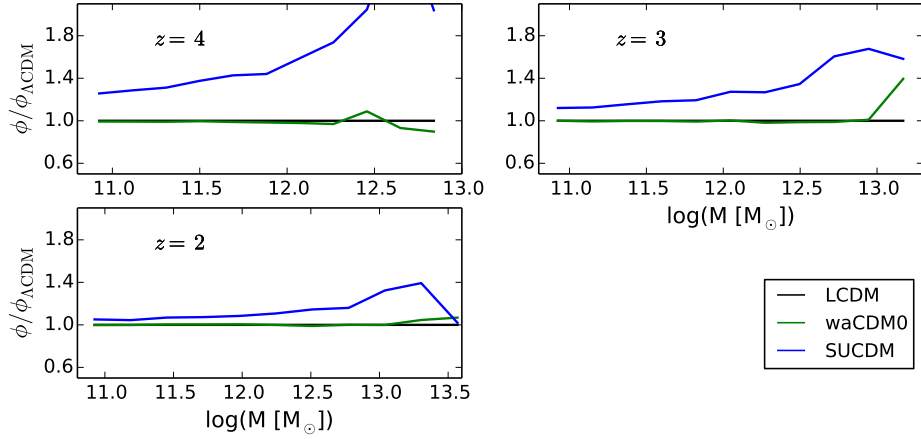


Figure 4.15: Ratio of the halo mass functions in different cosmologies to the halo mass function in the  $\Lambda\text{CDM}$  case for the HR dark matter only simulations ( $512^3$ ). We show snapshots at redshifts  $z = 4, 3, 2$  in the different panels.

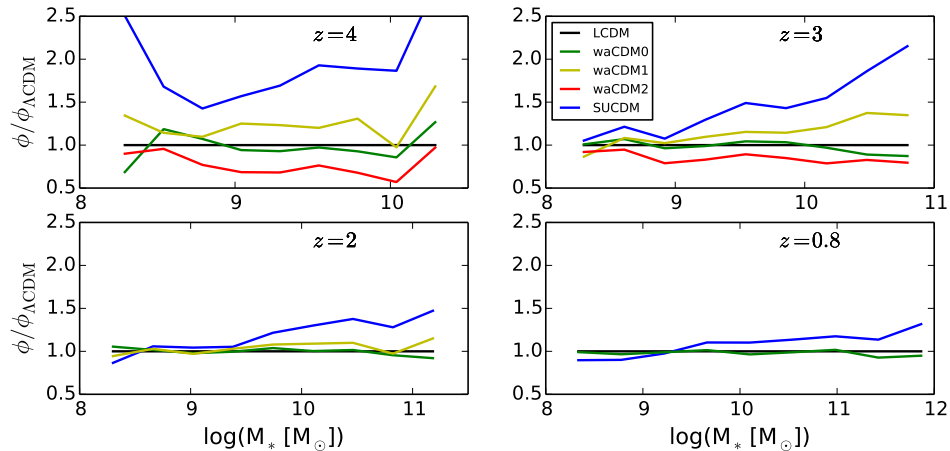


Figure 4.16: Ratio of the stellar mass functions to the stellar mass function in the  $\Lambda$ CDM case for the LR hydrodynamical simulations ( $256^3$ ). We show snapshots at redshifts  $z = 4, 3, 2, 0.8$  in the different panels.

in Figure 4.2). As expected, differences in structure distributions between cosmologies decrease going towards  $z = 0$ . waCDM0 shows a halo mass function remarkably close to  $\Lambda$ CDM at all examined redshifts; this was chosen by construction when setting the combination of  $w_a$  and  $w_0$  as done in Casarini et al. (2009b). Results from LR and HR are globally in agreement and differences in the halo mass functions among cosmologies show an increase when halo mass increases, as previously found in the literature (Klypin et al., 2003; Dolag et al., 2004; Bartelmann et al., 2005; Francis et al., 2009; Grossi and Springel, 2009).

### Galaxy Stellar Mass Function

In the  $\Lambda$ CDM LR hydrodynamical volume simulation ( $256^3$  particles) we find a total of about 900 galaxies at  $z = 4$  and about 6 300 galaxies at  $z = 0.8$  (our lowest redshift), while in the HR  $\Lambda$ CDM run we find about 7 000 galaxies at  $z = 4$  and 25 700 galaxies at  $z = 2$  (our lowest redshift).

In the LR  $\Lambda$ CDM run, we count about 52 galaxies with  $9.8 < \log(M_*) < 10.2$  at  $z = 4$  and 884 galaxies at  $z = 0.8$ . In the HR  $\Lambda$ CDM run, we find 94 galaxies with  $9.8 < \log(M_*) < 10.2$  at  $z = 4$  and 841 at  $z = 2$ .

In Figure 4.16 and Figure 4.17 we show the galaxy stellar mass functions for LR and HR cases. As expected, the number of galaxies with a certain stellar mass is higher in SUCDM cosmology compared to  $\Lambda$ CDM or waCDM2. Snapshots at redshift  $z = 4, 3$  allow a comparison between the two resolutions and, also in the hydrodynamical case, these globally agree.

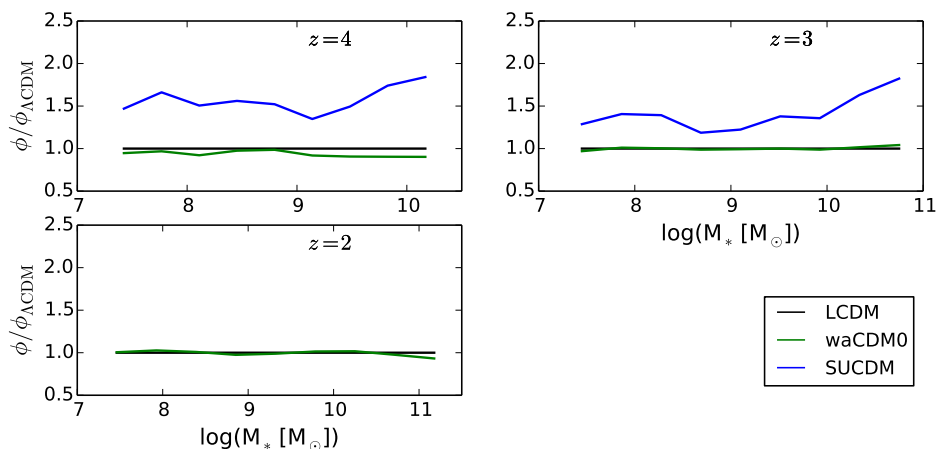


Figure 4.17: Ratio of the stellar mass functions to the stellar mass function in the  $\Lambda$ CDM case for the HR hydrodynamical simulations ( $512^3$ ). We show snapshots at redshifts  $z = 4, 3, 2$  in the different panels.

### Star Formation Efficiency and Resolution

Differences in the galaxy stellar mass functions are due to a combination of two effects: an increased number of dark matter haloes and a possible increase of star formation efficiency at a fixed halo mass. Thus, we are interested in disentangling the two quantities and focusing in the variations of the star formation efficiency. In the case of single-object high resolution multi-mass simulations, described in Section 4.2, differences in the dark matter accretion histories were amplified by the behavior of baryons. In fact, thanks to the highly non-linear nature of the star forming mechanisms, producing just slightly more stars leads to an increase of the inter stellar medium metallicity and, as in a vicious cycle, higher metallicity leads to a higher star formation. In turn, this process should be reproduced in all galaxies in our volumes and eventually differences in stellar mass between cosmologies should rise. To assess this, we look at the mean stellar mass of the sample of galaxies with a certain halo mass. We are interested in checking whether a “typical galaxy”, given a halo mass, makes more or less stars when cosmology changes. In Figure 4.18 and Figure 4.19 we normalize the mean stellar mass to the mean stellar mass in the  $\Lambda$ CDM case, respectively for the LR and HR cases.

In Figure 4.18 we show the behavior of the mean stellar mass as a function of halo mass for  $z = 4, 3, 2, 0.8$ . First of all, we note that the ranking in cosmological models is what we expected from Section 4.2, with SUCDM having the largest mean stellar masses and waCDM2 having the smallest. Secondly, the differences compared to  $\Lambda$ CDM are hardly reaching 20% for all redshifts. In panels showing  $z = 2$  and  $z = 0.8$  there seem to be larger

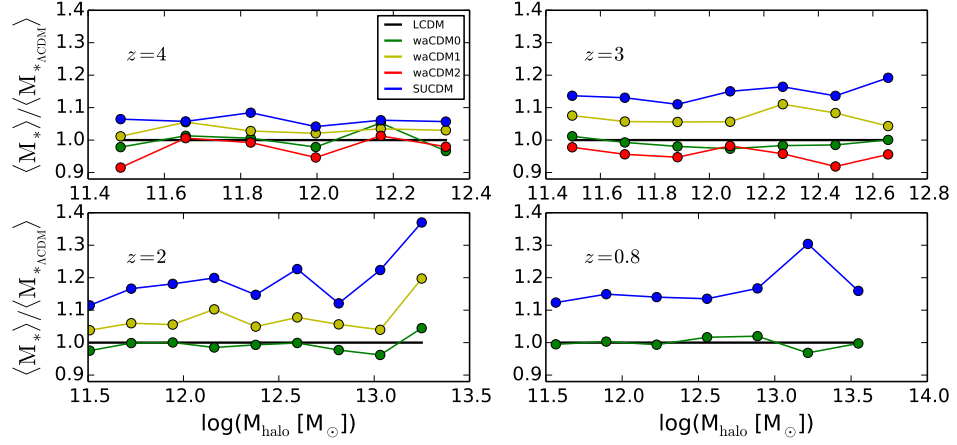


Figure 4.18: Ratio of the mean stellar mass to the mean stellar mass in the  $\Lambda$ CDM case as function of halo mass for the LR hydrodynamical simulations ( $256^3$ ). We show snapshots at redshifts  $z = 4, 3, 2, 0.8$  in the different panels.

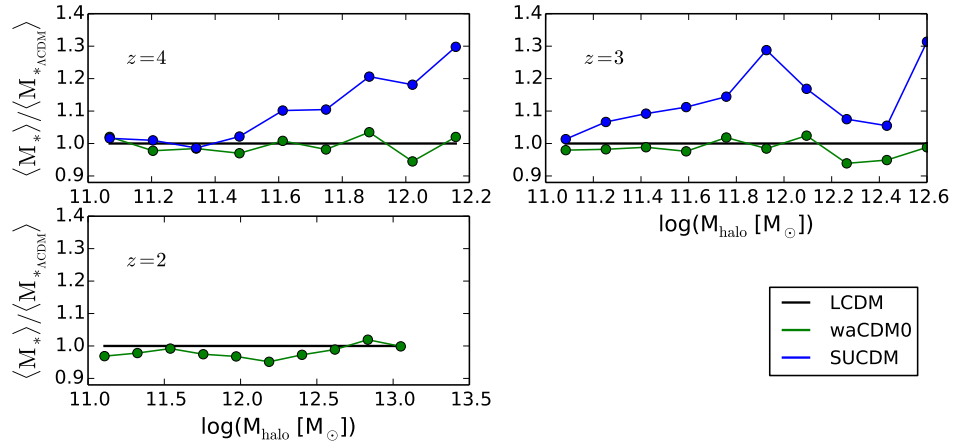


Figure 4.19: Ratio of the mean stellar mass to the mean stellar mass in the  $\Lambda$ CDM case as function of halo mass for the HR hydrodynamical simulations ( $512^3$ ). We show snapshots at redshifts  $z = 4, 3, 2$  in the different panels.

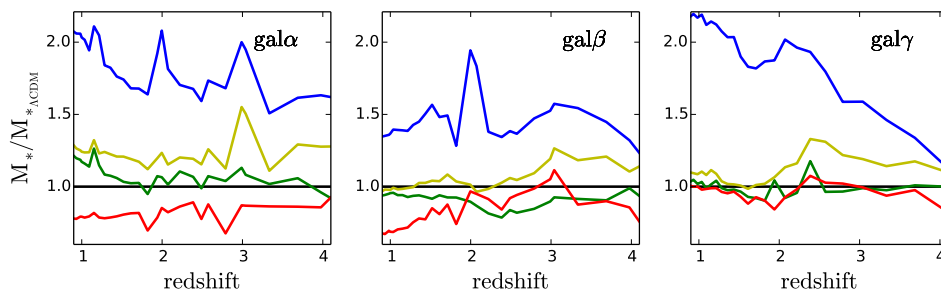


Figure 4.20: Ratio of the stellar mass to the stellar mass in the  $\Lambda$ CDM case as function of redshift for the single-galaxy simulations studied in Section 4.2. The dynamical dark energy models are the same used in the volume simulations.

differences but we would like to point out that for those masses feedback from active galactic nuclei is believed to be significant and GASOLINE does not have such feedback implemented. Thus we will not further discuss masses greater than  $10^{12}M_{\odot}$ . Furthermore, there seem to be an increase in the departures from  $\Lambda$ CDM from redshift  $z = 4$  onwards of about 5-10% at all masses. This could be the effect of two distinct causes, (i) star formation at redshift  $z = 4$  is not yet at its peak and thus has not reached its fully potential in fueling differences between cosmological models, or (ii) the resolution is too low at this redshift and the number of particles describing haloes is not sufficient to correctly capture star formation.

Figure 4.19 shows a clearer trend with increasing masses. Differences between SUCDM and  $\Lambda$ CDM reach 20% for a  $10^{12}M_{\odot}$  halo, while are negligible till  $3 \times 10^{11}M_{\odot}$  for  $z = 4$ . This could have a double explanation: (i) differences are larger at  $10^{12}M_{\odot}$  because this is the mass at which the peak for star formation efficiency is reached (Moster et al., 2010), (ii) we do not have enough resolution to describe objects less massive than  $3 \times 10^{11}M_{\odot}$  for  $z = 4$ . At  $z = 4$  differences in the LR case are only of 10%, while in the HR case they reach 20% for masses around  $3 \times 10^{11}M_{\odot}$ , suggesting that resolution is playing an important role in describing the star formation processes.

To better compare Figure 4.18 and Figure 4.19 with results from Section 4.2, in Figure 4.20 we show the ratio of stellar mass to  $\Lambda$ CDM stellar mass for  $gal\alpha$ ,  $gal\beta$  and  $gal\gamma$ . Departures from  $\Lambda$ CDM are clearly much more significant for these three galaxies, especially in the SUCDM case, where differences at  $z = 1, 2, 3, 4$  range from 50% to 100%. Given the striking difference between the single-galaxy runs and the cosmological volumes in departures from the  $\Lambda$ CDM reference model, it would be hard not to point the finger at the role that resolution plays in enhancing differences between star formations in the various cosmologies. As already pointed out, the non-linear cycle involving star formation and metallicity is what fuels differences

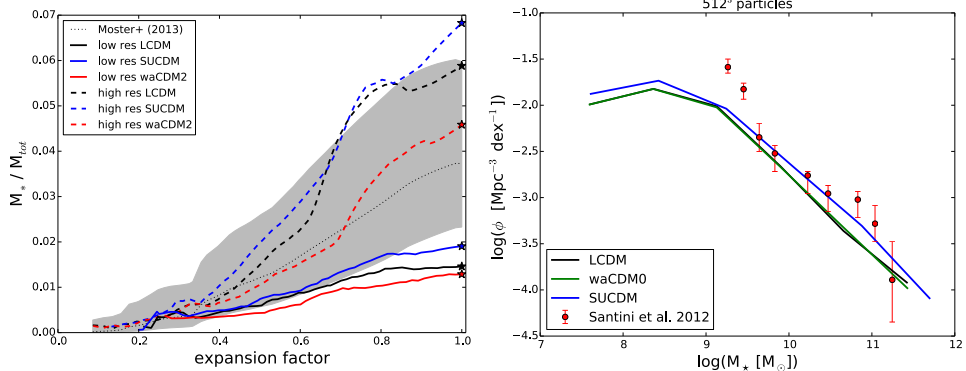


Figure 4.21: The left panel shows the evolution of the stellar-halo mass relation as a function of scale factor for  $\text{gal}\beta$  for  $\Lambda$ CDM, waCDM2 and SUCDM. Each cosmology has a high resolution (dashed lines) and low resolution (solid lines) run. The high resolution is the same resolution used in Section 4.2, while the low resolution is comparable to the resolution in the HR volume. The right panel shows the stellar mass functions for  $\Lambda$ CDM, waCDM0 and SUCDM for the HR volume. In red observational constraints from Santini et al. (2012) are shown.

in the single-objects runs. When these processes cannot be represented by a sufficiently high number of particles, their role in enhancing differences in the accretion history due to cosmology is no longer dominant. To further support the last statement, we ran  $\text{gal}\beta$  with the lowest possible resolution for a multi-mass simulation, i.e. refinement factor  $RF = 2$ , while the simulations showed in Section 4.2 and in Figure 4.20 have  $RF = 8$ . This implies that the gas mass resolution for the HR set is  $m_{\text{gas}} = 6.9 \times 10^7 M_{\odot}$ , while in the single-galaxy runs  $m_{\text{gas}} = 4.2 \times 10^5 M_{\odot}$ . The evolution of the stellar-halo mass relation as a function of the scale factor is shown in the left panel of Figure 4.21. The differences between cosmologies are significantly reduced when the resolution is lowered. Note that the dark matter particle mass in the low-resolution multi-mass  $\text{gal}\beta$  is  $m_{\text{DM}} = 1.4 \times 10^8 M_{\odot}$  and in the HR cosmological volume is  $m_{\text{DM}} = 4.0 \times 10^8 M_{\odot}$ .

Furthermore, the right panel of Figure 4.21 shows the mass functions for the HR volume runs at  $z = 3$ . In red we show the observational constraints from Santini et al. (2012) for redshift  $z \simeq 2.5$ . Despite the normalization of the stellar mass functions that can be explained with a non-precise redshift matching between our snapshot and the data, it is clear that the error bars on observations are comparable to the difference that we find between SUCDM and  $\Lambda$ CDM (which are the two most distant models in our choices). Thus, at our resolution, viable dynamical dark energy models cannot be constrained using current data on the galaxy mass function.

Fontanot et al. (2012) investigated the effects of early dark energy models

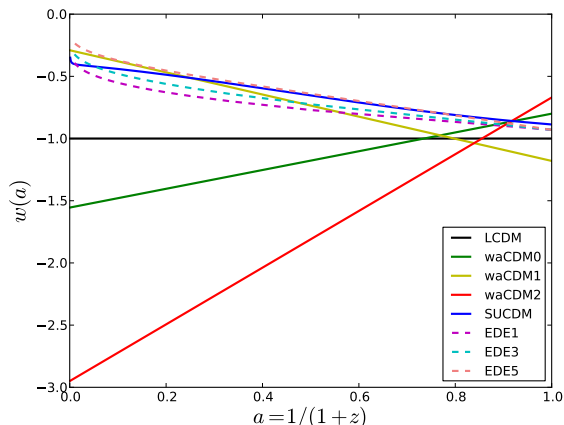


Figure 4.22: Evolutions of the equation of state parameter  $w \equiv p/\rho$  for the dynamical dark energy models used in this Chapter (solid lines) and for the Early Dark Energy (EDE) models used in [Fontanot et al. \(2012\)](#) (dashed lines).

([Wetterich, 1988](#)) using Semi Analytical Models (SAMs). Early dark energy models exhibit a non-negligible amount of dark energy at early times. In [Figure 4.22](#) we show the evolutions of the equation of state parameter  $w \equiv p/\rho$  for his choices of early dark energy parametrization (EDE1, EDE3, EDE5) and our choices for dynamical dark energy models. [Fontanot et al.](#) concluded that, for their models, differences due to cosmology were not significant given the current data precision and were especially evident at high redshifts. In [Section 4.2](#) we attributed their small differences between cosmological models compared to our findings to the fact that SAMs cannot account for the large role of non-linearity in star formation processes. The same happens in hydrodynamical simulations when resolution is not large enough to fully describe the interplay between star formation and metallicity. Thus, SAMs or hydrodynamical cosmological volume simulations (at this state) are not the best tools to set precise constraints to differentiate among dynamical dark energy models.

#### 4.3.4 Conclusions on Hydrodynamical Cosmological Volumes in Dynamical Dark Energy

We ran cosmological hydrodynamical simulations of a volume with side  $L_{\text{box}} = 114$  Mpc in dynamical dark energy models plus the  $\Lambda$ CDM reference model in two resolutions,  $N_p = 256^3$  and  $N_p = 512^3$ . The code used is GASOLINE-DE for hydrodynamical runs, which features gas cooling, supernova feedback and feedback from young massive stars, while we used PKDGRAV for dark matter only runs. The dynamical dark energy models

---

chosen lie within the  $2\sigma$  constraints from WMAP7. Our goal was to test the effects of dynamical dark energy on galaxy formation across a wider range of galaxy masses, environments and merger histories compared to the single-object runs shown in Section 4.2 in the same cosmological models.

In the cases of single-galaxy runs we find that baryonic processes enhance already present differences in dark matter accretion histories across the various dynamical dark energy models, and produce an increase in stellar mass that can reach a factor of two in SUCDM compared to  $\Lambda$ CDM, while dark matter mass only increases of a few percents. We ascribe this boost to the feedback cycle that connects the increase in star formation to an increase of metallicity, which is in turn connected to a decreasing cooling time. We expected the same process to be manifest at all mass scales, possibly with a different degree of efficiency as a function of halo mass.

For all examined redshifts,  $z = 0.8, 2, 3, 4$ , we find that in the galaxy sample contained in our cosmological volumes the increase in the mean stellar mass given a halo mass is at maximum 20% in SUCDM, our most distant model from  $\Lambda$ CDM. We attribute the lower differences among cosmologies compared to the single-galaxy runs to the change in resolution. In fact, in order for baryonic feedback processes to be well sampled they require a high enough resolution. For comparison, the mass resolution of the most refined of the two sets of volumes ( $N_p = 512^3$ ) is for gas particles (initial masses)  $m_{\text{gas}} = 6.9 \times 10^7 M_\odot$ , while in the single-galaxy runs  $m_{\text{gas}} = 4.2 \times 10^5 M_\odot$ . To support the resolution argument, we ran one of the single-galaxy simulations with a resolution for gas particles  $m_{\text{gas}} = 2.7 \times 10^7 M_\odot$  and differences between cosmologies became comparable to the differences found in the hydrodynamical volumes.

To conclude, we would like to stress that in the era of precision cosmology making detailed numerical predictions is essential. In this Section we showed that in order to distinguish between  $\Lambda$ CDM and a dynamical dark energy models we need to employ high enough resolutions to fully describe the baryonic processes that fuel differences between cosmologies.

## 4.4 Dwarf Galaxies Simulations in Dynamical Dark Energy and $\Lambda$ CDM

### 4.4.1 Introduction

In Section 4.2 we investigated the effects of dynamical dark energy on disc galaxies with masses  $\sim 5 \times 10^{11} M_\odot$ . We found that the effects of dynamical dark energy on the star formation efficiency were significant and they shaped galaxy properties. In this Section we aim at extending our study to dwarf mass scales, precisely to haloes with masses between a few  $10^9 - 10^{10} M_\odot$ .

Inconsistencies in the  $\Lambda$ CDM paradigm are mostly showing at dwarf

galaxy scales.  $\Lambda$ CDM predicts an extremely low efficiency in converting gas into stars at these halo masses, given that in dark matter only simulations the number of subhaloes in a Milky-Way-size host halo is much higher than the number of satellite dwarf galaxies observed (Klypin et al., 1999; Moore et al., 1999). Furthermore, recent claims (Boylan-Kolchin et al., 2011, 2012) suggested that the central density of these dwarf haloes must be lower than expected from dark matter only simulations (Flores and Primack, 1994; Kuzio de Naray et al., 2008; de Blok et al., 2008), questioning whether dwarf haloes can be described by a Navarro, Frenk and White (NFW) profile (Navarro et al., 1997).

Dekel and Silk (1986) and Bullock et al. (2000) suggested that the low efficiency in converting gas into stars for dwarf haloes could be attributed to both feedback from supernovae and from the UV ionizing background. In fact, supernova explosions not only heat the gas but, for these low masses, can also easily blow the gas away from the halo; while the existence of a UV background radiation prevents less massive haloes from cooling gas and start star formation. Thus, the possibility for a dwarf halo to form stars or to remain dark until  $z = 0$  is strictly connected to how much its virial mass has grown by the time reionization happens. As shown in Section 4.2, varying the background cosmology translates into varying accretion histories, so that for all redshifts galaxies in SUCDM were always more massive than their equivalent galaxies in  $\Lambda$ CDM. These variations were only of a few percents in the case of disc galaxies, but for dwarf galaxies such variations in mass can become crucial in determining whether star formation will start at all.

Supernova feedback can also be responsible for halo density profile that is less cuspy when rapid starburst events occur. These can transfer energy to dark matter particles which in turn will make the system expand (Navarro et al., 1996; Governato et al., 2010; Pontzen and Governato, 2012; Di Cintio et al., 2014) and thus lower the density in inner regions. On the other hand, Trujillo-Gomez et al. (2015) find that in their simulations the formation of a core in the dwarf density profiles is strictly linked to radiation pressure more than feedback from supernovae. Recently Oñorbe et al. (2015) simulated dwarf haloes with  $M_{\text{vir}} = 10^{9.5-10} M_{\odot}$  and they were able to produce a cored density profile when the dwarf star formation was mainly happening at later times. A delayed star formation as cause for lower density in the halo center was also a proposed argument in Stinson et al. (2013b) and is the reason for flat rotation curves in the  $w$ aCDM2 models discussed in Section 4.2 (see Figure 4.9). The effects on the density profiles are less evident for these more massive galaxies, but anyhow Figure 4.3 shows the slightly less cuspy profile of the  $w$ aCDM2 case. Based on these reasons, we are interested in extending the dynamical dark energy analysis to dwarf galaxy mass scales.

The dwarf galaxies from Oñorbe et al. (2015) reproduce the observational-inferred relation between stellar mass and dark matter halo mass obtained via the abundance matching technique, but one could argue that a larger

---

set of dwarf halo simulations is needed to better sample the behavior of star formation efficiency in dwarf haloes. [Boylan-Kolchin et al. \(2011\)](#) pointed out that there could be a mass scale under which star formation will become stochastic, and, more recently, [Sawala et al. \(2014a,b\)](#) suggest that the mass scale could be  $M_{\text{vir}} \simeq 10^{9-9.5} M_{\odot}$ . To better test these suggestions with a larger sample of dwarf galaxies, in the second part of this Section we will describe our study on 22 dwarf galaxies with masses  $\sim 10^{9-10} M_{\odot}$  within a  $\Lambda$ CDM scenario.

This is part of the study that will be published in [Macciò, Penzo et al. in preparation](#). I and A. V. Macciò performed simulations and carried out the analysis for half of the  $\Lambda$ CDM dwarf galaxy sample each. Furthermore, I ran and analyzed the set of dwarf galaxy simulations in dynamical dark energy.

#### 4.4.2 Results and Discussion

We present a set of four dwarf galaxies with virial masses of a few  $10^9 M_{\odot}$ . We chose the two most distant cosmological models based on the results from Section 4.2, waCDM2 and SUCDM. We selected the galaxies from a volume of side 15 Mpc/h and then re-simulated them at a much higher resolution. Particle masses are  $m_{\text{DM}}=4.1 \times 10^3 M_{\odot}$ ,  $m_{\text{gas}}=8.2 \times 10^2 M_{\odot}$  (initial),  $m_{\text{star}}=2.7 \times 10^2 M_{\odot}$  (initial), while the softening length for dark matter particles is 64 pc and for stellar and gas particles is 29 pc. Initial conditions were generated using GRAFIC2-DE and they were evolved using GASOLINE-DE (for details on the codes, see Sections 3.1.1 and 3.2.1). Our aim is to study dwarf galaxies as satellites of a Milky-Way size halo, because of this, each galaxy was evolved from  $z = 99$  to  $z = 1$  assuming that for  $z \geq 1$  they would evolve as single objects and for  $z \leq 1$  the satellites would be accreted and would start to feel the influence of the parent halo.

#### Stellar-Halo Mass Relation

Figure 4.23 shows stellar and halo masses for our four dwarfs in  $\Lambda$ CDM, waCDM2 and SUCDM cosmologies. We show the prediction from abundance matching ([Moster et al., 2013](#)), but we should remark that this is an extrapolation to lower masses of the original relation. The hierarchy of cosmological models is maintained, with the SUCDM dwarfs making more stars than  $\Lambda$ CDM and waCDM2, but the difference in stellar mass compared to  $\Lambda$ CDM varies in the four dwarfs and is negligible in two out of four cases. That differences between cosmological models vary among our four cases is in agreement with the statement that star formation becomes stochastic at these mass scales, thus also the enhancement due to baryonic processes of differences between cosmological models is expected to vary. In the case of the dwarf with the lowest halo mass, its waCDM2 realization does not make

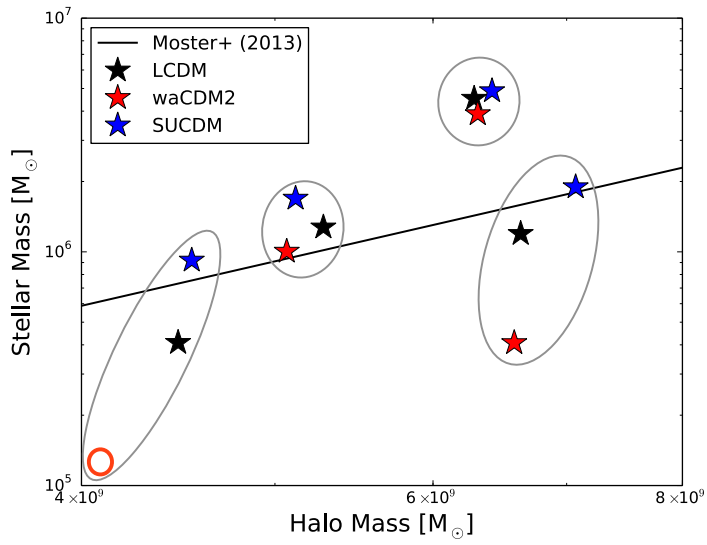


Figure 4.23: Stellar-halo mass relation for our four dwarf galaxies in  $\Lambda$ CDM, waCDM2 and SUCDM cosmologies. The black line shows an extrapolation to lower masses of the prediction from abundance matching. Symbolically, the empty red circle represents the waCDM2 dwarf galaxy that did not make stars. Different realizations of the same galaxy in the various cosmologies are grouped by the grey ellipses.

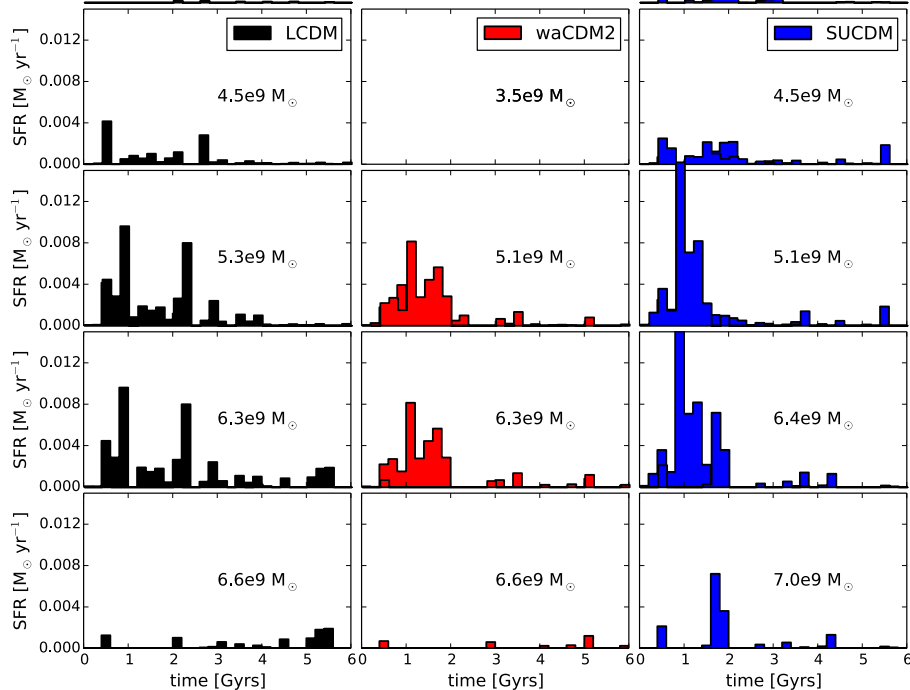


Figure 4.24: Each row shows the Star Formation Rate (SFR) of one of the three dwarf galaxies in  $\Lambda$ CDM, waCDM2 and SUCDM cosmologies. Virial mass is written in each panel.

any stars and will remain dark throughout its life. This shows that even small departures from  $\Lambda$ CDM can affect the number of luminous subhaloes when their virial mass is around a few  $10^9 M_{\odot}$ .

### Star Formation Histories

Figure 4.24 shows the star formation histories for our four dwarf galaxies. Each row represents one galaxy and each column a cosmological model. Our four SUCDM dwarf galaxies show a global increase of star formation compared to  $\Lambda$ CDM and, on the other hand, the three dwarf galaxies in waCDM2 show a decrease compared to their  $\Lambda$ CDM realizations. The trend of delaying star formation in waCDM2 and, on the other hand, anticipating star formation in SUCDM is no longer clear at these masses as it was for disc galaxies in Figure 4.7. Even given the limited number of simulations, we can notice quite different behaviors even within cosmologies, supporting the suggested stochasticity on these masses (Boylan-Kolchin et al., 2011; Sawala et al., 2014a,b).

### 4.4.3 Remarks

We conclude our experiment on dynamical dark energy at dwarf mass scales by stating that the impact that cosmology has on our four dwarf galaxies is not as significant as in the case of  $\sim 5 \times 10^{11} M_{\odot}$  galaxies showed in Section 4.2. Stellar mass at  $z = 1$  has important differences only in two out of four cases. Star formation histories are globally enhanced or decreased but no delay or anticipation shows, as instead was the case for  $\sim 5 \times 10^{11} M_{\odot}$  galaxies. Furthermore, for all our dwarf galaxies, density profiles do not vary between different dynamical dark energy models (differences are less than few percents at inner radii). On the other hand, diversity in star formation histories within a given cosmological model may be important. Indeed, Figure 4.24 shows a significant difference in star formation histories between the two most massive dwarfs galaxies which have comparable masses; in all cosmologies we note a significantly higher star formation in the  $6.3 \times 10^9 M_{\odot}$  galaxy.

### 4.4.4 $\Lambda$ CDM Follow-Up

To better investigate what fuels these different star formation histories, in the next Section we will increase the dwarf sample and focus on the  $\Lambda$ CDM model. This is part of the study that will be carried out in [Macciò, Penzo et al. in preparation](#).

Figure 4.25 shows our sample of 22 galaxies; circular symbols indicate galaxies that remained dark. Resolution and settings are the same as described in the previous Section. The solid line shows the extrapolation of the abundance matching relation from [Moster et al. \(2013\)](#), suggesting a quite large scatter ( $\sim$  a factor of ten) around the extrapolated relation. To be noted that 7 out of 22 galaxies never started forming stars. Their halo masses span from  $8 \times 10^8 M_{\odot}$  to  $\sim 4 \times 10^9 M_{\odot}$ . In our sample we have 8 galaxies in the same halo mass range that on the contrary were active in forming stars, suggesting that halo mass is not uniquely what determines these different star forming modes.

As suggested in the previous Section, at a given halo mass, we find heterogeneous star formation histories. Figure 4.26 shows star formation histories for all our dwarf galaxies that formed stars. Virial masses in  $M_{\odot}$  are shown for each panel. We note that generally more massive systems tend to have more active star formation, but we can find systems with comparable masses that have very different star formation behaviors.

To better investigate what triggers such variety of star formation modes, we investigate four galaxies with comparable masses, dwarf $\alpha$  (blue), dwarf $\beta$  (red), dwarf $\gamma$  (cyan) and dwarf $\delta$  (black). Precisely, their masses are  $5.0 \times 10^9 M_{\odot}$ ,  $5.7 \times 10^9 M_{\odot}$ ,  $6.0 \times 10^9 M_{\odot}$  and  $1.0 \times 10^{10} M_{\odot}$ . The left panel of Figure 4.27 shows their star formation rates with a different binning compared to the previous figures. The right panel shows density profiles normalized to the

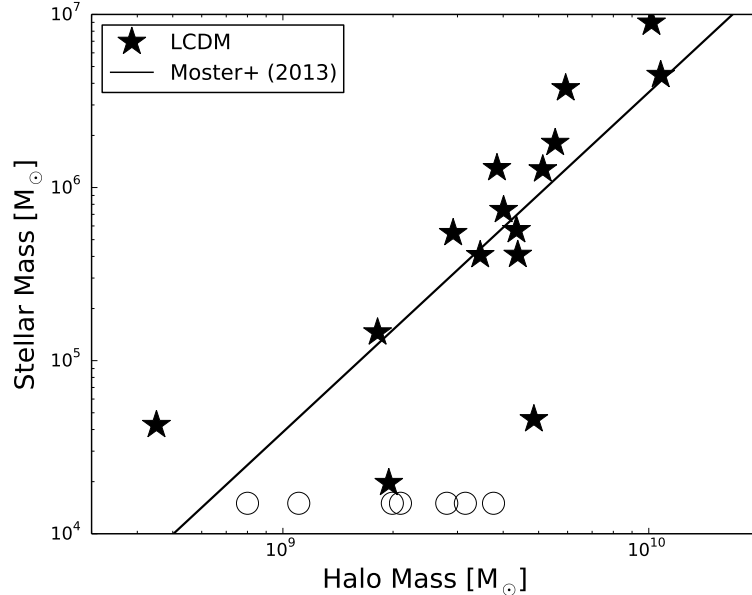


Figure 4.25: Stellar-halo mass relation for our 22 dwarf galaxies in  $\Lambda$ CDM cosmology at  $z = 1$ . The black line shows an extrapolation to lower masses of the abundance matching from [Moster et al. \(2013\)](#). The round solid symbols represent galaxies that did not make any stars.

radius at which the density profile slope reaches  $-2$  (dashed lines show an NFW profile). While for dwarf $\beta$  the scatter is high for the inner points, we can confidently say that dwarf $\delta$  does show a cored density profile. [Oñorbe et al. \(2015\)](#) also were able to produce cores in their two dwarf galaxies, which have virial masses that are comparable with the virial mass of dwarf $\delta$ .

Figure 4.28 shows for dwarf $\alpha$ , dwarf $\beta$ , dwarf $\gamma$  the evolution of the amount of dark matter mass contained in a sphere centered on the potential minimum of each halo with radius 4 kpc (left panel) and 2 kpc (right panel). Note that virial radii for these systems are  $\sim 35$ -45 kpc, thus we are estimating the change in dark matter mass in their centers, regions where star formation is expected to happen. The steep increase shown in dwarf $\beta$  and dwarf $\gamma$  is the result of a major merger, which is what triggers further star formation episodes in these two systems. As a result, their stellar masses at  $z = 1$  is one order of magnitude higher than the stellar mass in dwarf $\alpha$ . To justify this claim, in Figure 4.29 we show density maps (first row) and gas temperature maps (second row) for a cube of size 20 kpc for dwarf $\beta$ . Panels are snapshots taken at  $z = 4.97, 4.49, 3.98$ . The major merger can clearly be followed in the dark matter row. The gas temperature snapshots show a temperature increase after the major merger happened. At this high resolution, we can

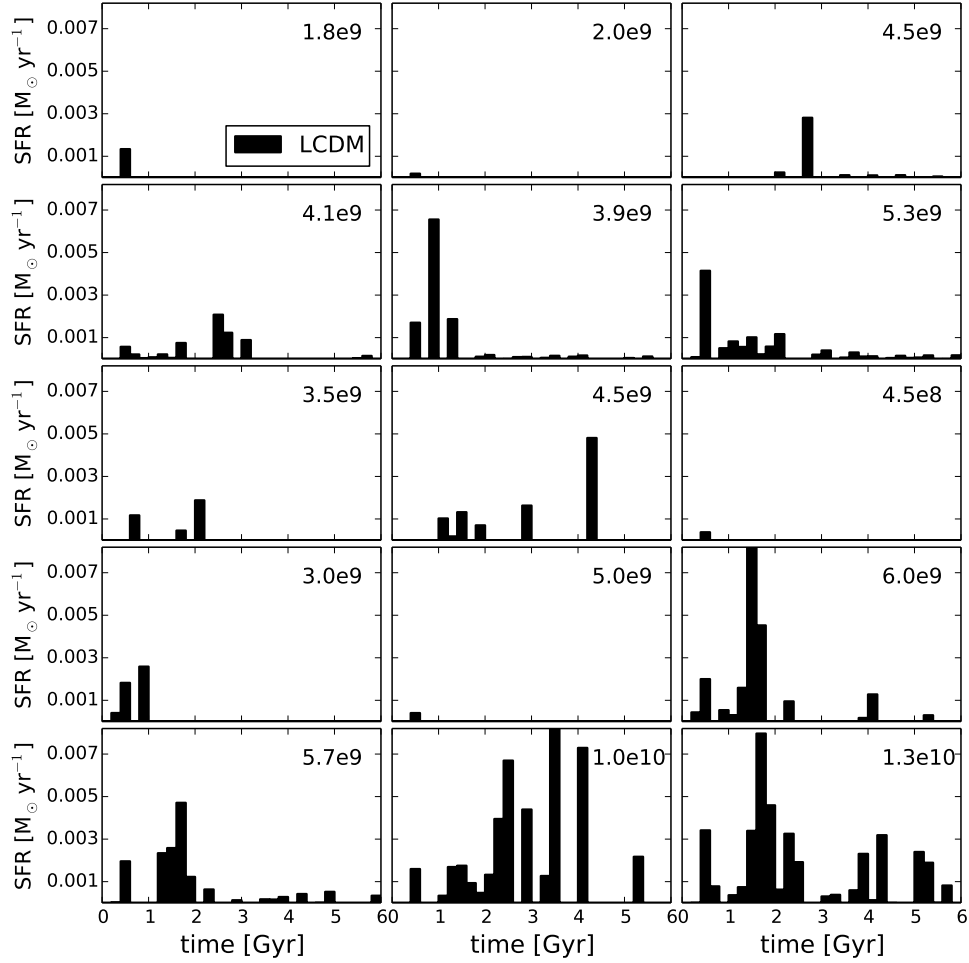


Figure 4.26: Each panel shows the Star Formation Rate (SFR) of one of the 15 dwarf galaxies that succeeded in forming stars in  $\Lambda$ CDM cosmology. Virial mass in  $M_{\odot}$  is written on each panel.

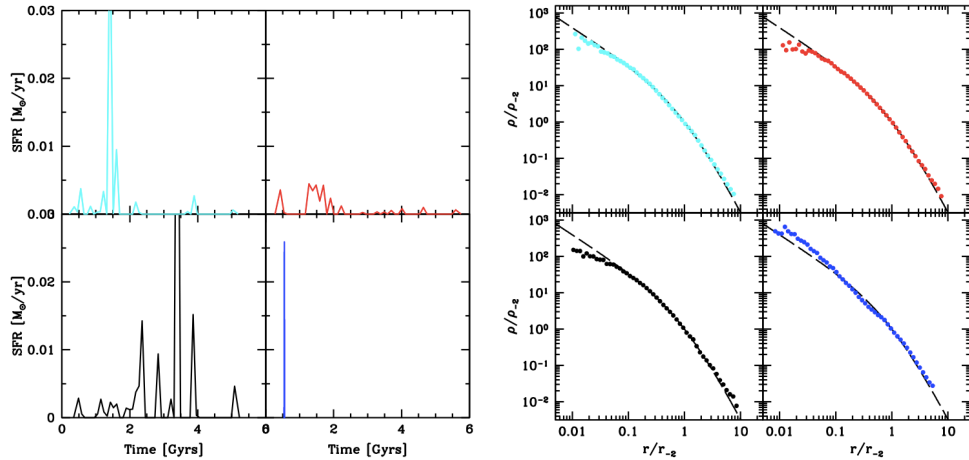


Figure 4.27: The left panel shows star formation rates of four dwarf galaxies from our sample, dwarf $\alpha$  (blue), dwarf $\beta$  (red), dwarf $\gamma$  (cyan) and dwarf $\delta$  (black), with masses  $5.0 \times 10^9 M_{\odot}$ ,  $5.7 \times 10^9 M_{\odot}$ ,  $6.0 \times 10^9 M_{\odot}$  and  $1.0 \times 10^{10} M_{\odot}$ . The right panel shows density profiles for the same galaxies with distance from the center normalized to the radius at which the density profile slope is  $-2$ .

fully describe the blast wave that is being produced. The presence of such strong increase in temperature is due to the strong feedback, which is an evidence for a significant increase in star formation. As a consequence, we find that more than 85% of the stellar mass is produced during the merger.

#### 4.4.5 Conclusions on Dwarf Galaxies Simulations in Dynamical Dark Energy and $\Lambda$ CDM

In this Section we aimed at studying the properties of simulated satellites of Milky-Way size galaxies. To do so, we built a suite of hydrodynamical single-object simulations of dwarf galaxies with masses  $\sim 10^9$ – $10^{10} M_{\odot}$ . A subsample of four objects were run in waCDM2 and SUCDM dynamical dark energy models described in Section 4.1. Our goal is to study the properties of dwarf satellites before the in-fall into their parent halo. For this reason, we simulated isolated dwarf galaxies from  $z = 99$  to  $z = 1$ , with the assumption that for  $z > 1$  the influence of the parent halo can be neglected. At these mass scales, galaxies have typical ratios  $M_*/M_{\text{DM}} \sim 10^{-5}$  and  $R_*/R_{\text{DM}} \lesssim 0.001$ , which make them interesting environments to test the effects of baryons on the dark matter distribution.

Comparing our findings on dwarf galaxies in dynamical dark energy models with Section 4.2, differences in stellar mass and in star formations histories compared to the  $\Lambda$ CDM reference models are less significant for dwarf scales than for disc galaxy scales. Since differences between cosmologies are fu-

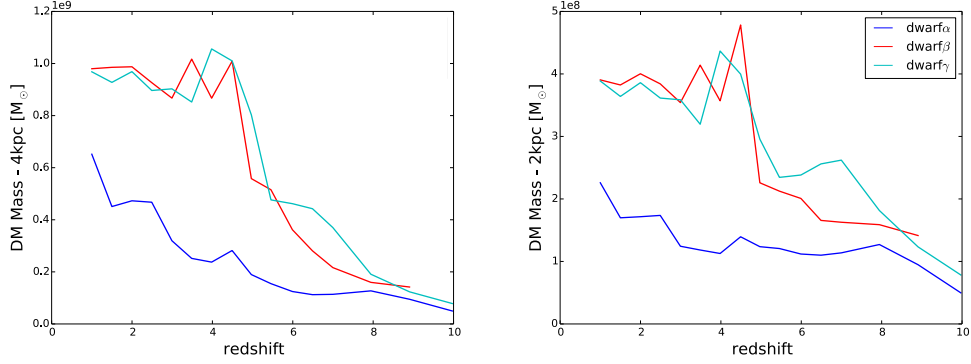


Figure 4.28: We show the dark matter mass evolution for three dwarf galaxies with masses  $5.0 \times 10^9 M_\odot$  (blue),  $5.7 \times 10^9 M_\odot$  (red) and  $6.0 \times 10^9 M_\odot$  (cyan) for a sphere centered on the halo center with radius 4 kpc (left panel) and 2 kpc (right panel).

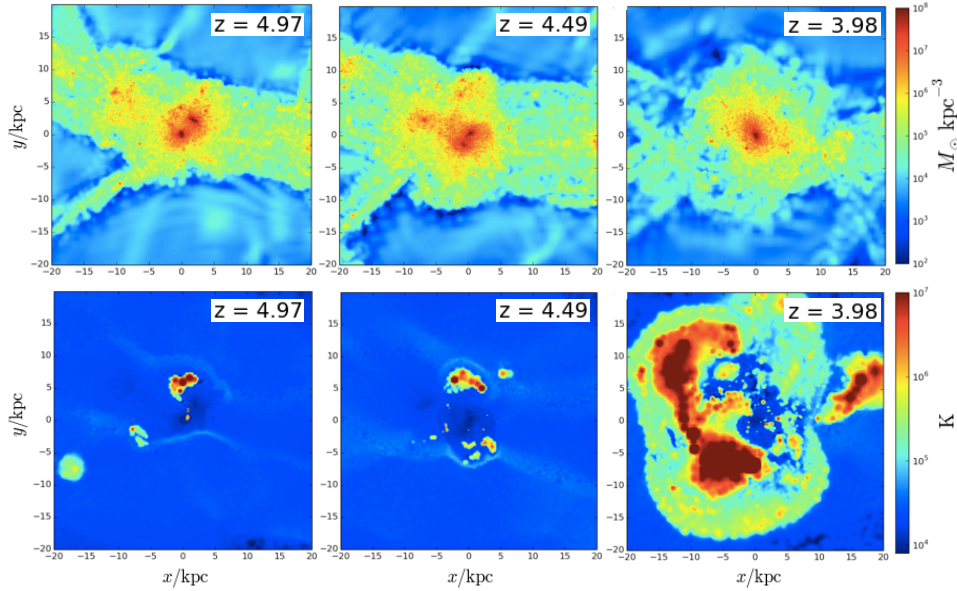


Figure 4.29: First row shows dark matter density, while the second row the gas temperature at three different redshifts  $z = 4.97, 4.49, 3.98$ .

---

eled by baryonic feedback mechanisms, we expected larger departures from  $\Lambda$ CDM close to the peak of star formation efficiency ( $\sim 10^{12}M_{\odot}$ ). We as well realized that scatter in star formation histories within a given cosmology among different dwarf galaxies was more significant than the scatter among cosmologies given a certain galaxy. Due to this, we enlarged the sample and focused only in a  $\Lambda$ CDM cosmology.

In our sample of 22 dwarf galaxies, we find that 7 out of 13 haloes with masses  $8 \times 10^8 \lesssim M_{\text{halo}}/M_{\odot} \lesssim 4 \times 10^9$  do not form any stars. The reason for these haloes to remain dark lies in the presence of the UV background radiation from the reionization epoch. We turned off its contribution in one of these simulations and the gas in the halo was able to cool and, consequently, it started star formation.

Our sample follows the extrapolation of the abundance matching prediction for the stellar-halo mass relation at  $z = 1$ , but shows a large scatter ( $\sim$  factor of 10). We find a variety of star formation histories which supports the suggestion that star formation at these mass scales might be stochastic. Though, the stochasticity of star formation can be connected to the stochasticity of halo formation histories. We find that whether a dwarf halo undergoes major mergers in its recent past or not produces very different galaxy properties at fixed halo mass. Because of this, we expect dwarf satellites to be heterogeneous objects even before their in-fall due to their very different formation histories.

## Chapter 5

# Halo and Subhalo properties in Coupled Dark energy

Despite the highly successful inflationary  $\Lambda$ CDM paradigm, the fundamental problems associated with the introduction of a cosmological constant, namely *fine-tuning* and *coincidence* problems (Weinberg, 1989), have served as motivations for alternative descriptions of the dark sector.

Given the currently still unknown nature of the dark sector, the possibility of a non-null coupling between dark matter and dark energy has been considered (see Chapter 1.4.2). Since in these models dark matter and dark energy density evolutions are strongly coupled, the *coincidence* problem outlined in Section 1.3.4 is alleviated.

The effects of such interaction might be seen on the Cosmic Microwave Background (CMB), on supernovae and on the growth of structures, as pointed out by Matarrese et al. (2003); Amendola (2004b); Amendola et al. (2004); Koivisto (2005); Guo et al. (2007) and many others. Structure formation has been as well investigated via numerical simulations by Macciò et al. (2004); Baldi et al. (2010); Li and Barrow (2011); Carlesi et al. (2014) and their follow up works, where the statistical distribution of structures has been studied. Both Baldi et al. (2010) and Carlesi et al. (2014) found that, when introducing a coupling between dark energy and dark matter, halo concentrations decrease.

This Chapter is based on Penzo et al. (2015), and will describe the analysis of the first high resolution simulations on galactic scales in coupled dark energy cosmology. The aim is to obtain high enough resolutions to investigate the properties of the dark matter distribution at sub-galactic scales, mass scales at which the effects of the coupling have not yet been studied. The subhalos will in turn be the hosts of dwarf galaxies and their properties can be compared with observations of satellite dwarf galaxies of both Milky Way and Andromeda. In fact, despite  $\Lambda$ CDM predictions on large scales being in very good agreement with galaxy clustering surveys (Jones

---

et al., 2009; Alam et al., 2015), on galactic scales challenges between  $\Lambda$ CDM predictions and observations have appeared.

Firstly, the *missing satellites* problem, i.e. overabundance of substructures in  $\Lambda$ CDM Milky-Way size halo simulations when compared to observations of the Milky Way dwarf galaxies (Klypin et al., 1999; Moore et al., 1999). On the other hand, as showed in Madau et al. (2008) and Macciò et al. (2010), accounting for the baryonic physics drastically reduces the number of visible satellites.

Secondly, the *core/cusp* problem, namely the inconsistency between the constant density cores estimated from observations and the cuspy inner density profiles found in  $\Lambda$ CDM simulations. See Flores and Primack (1994); Moore (1994); Diemand et al. (2005); Gentile et al. (2009); Walker and Peñarrubia (2011); Agnello and Evans (2012); Salucci et al. (2012), but also van den Bosch and Swaters (2001); Swaters et al. (2003); Simon et al. (2005). While this inconsistency can be attributed to baryonic feedback processes (e.g. Governato et al., 2012; Di Cintio et al., 2014; Oñorbe et al., 2015), for the case of Milky Way satellites the baryonic explanation is not straightforward since these objects can be almost completely dark matter dominated. Baldi et al. (2010) and Carlesi et al. (2014) showed that for halos with  $M \gtrsim 10^{13} M_{\odot}$  the coupling between dark matter and dark energy produces density profiles that are less cuspy in the inner density regions, which can help alleviating the core/cusp problem. The aim of the work presented in this Chapter is to investigate whether this effect persists at lower masses  $M \lesssim 10^{12} M_{\odot}$ .

Moreover, concentrations of the most massive subhalos orbiting around a  $\Lambda$ CDM Milky-Way size halo seem to be too high to be hosting the brightest dwarf galaxies observed. This translates into a prediction from  $\Lambda$ CDM numerical simulations for the existence of massive dark matter subhalos that seem to have failed at forming stars, and is known as the *too big to fail* problem (Boylan-Kolchin et al., 2011; Lovell et al., 2012; Rashkov et al., 2012; Tollerud et al., 2012).

Whether these issues bring serious challenges for the  $\Lambda$ CDM model or whether they can entirely be treated by invoking baryonic physics is currently under debate. The aim of this study is to investigate the properties of halos and their sub-structures to determine whether coupled dark energy cosmologies can alleviate the aforementioned issues.

This work is based on Penzo et al. (2015), a result of the collaboration with M. Baldi, who performed the numerical simulations. I produced the initial conditions and carried out the analysis, under the supervision of A. V. Macciò.

## 5.1 Details on the Cosmological Models

As described in Section 1.4.2 and 2.1.1, the main effects of an interaction between dark matter and dark energy are: (i) dark matter particles masses change with time, (ii) the gravitational strength felt by dark matter particles is stronger than in Newtonian dynamics, (iii) an extra friction term appears, which accelerates dark matter particles in the direction of their motion. We plan to investigate how these departures from  $\Lambda$ CDM influence galactic and sub-galactic scales.

Based on Baldi et al. (2010) and Baldi (2011a), we chose three coupling scenarios. EXP003 (cyan) and EXP008e3 (blue) are observationally viable models (see Pettorino et al. 2012 for CMB constraints on the coupling value), respectively with a constant coupling  $\beta_c = 0.15$  and a coupling  $\beta_c(a)$  varying with the scale factor. We choose the parametrization

$$\beta_c(a) = \beta_0 e^{\beta_1 \phi(a) M_{\text{Pl}}}, \quad (5.1)$$

where  $\beta_0 = 0.4$  and  $\beta_1 = 3$ . We also explore an extreme constant coupling case EXP006 (red) with  $\beta_c = 0.3$  (about  $6\sigma$  outside present observational limits, Pettorino et al. 2012) to better understand the implications of the coupling. All the models share the same cosmological parameters and have at  $z = 0$ :  $\Omega_{b_0} = 0.0458$ ,  $\Omega_{\text{DM}_0} = 0.229$ ,  $H_0 = 70.2 \text{ km s}^{-1} \text{ Mpc}^{-1}$ ,  $\sigma_8 = 0.816$ ,  $n_s = 0.968$ , where these parameters are density parameters for baryons and dark matter, Hubble constant, root mean square of the fluctuation amplitudes and primeval spectra index.

## 5.2 Numerical Set-Up

We first generated two sets of uniform particle distributions, a 80 Mpc/h box and a 12 Mpc/h box, both with  $350^3$  particles. We produced the initial conditions with GRAFIC-2 (see Section 3.1.1), which requires background evolution and transfer functions. In the left panel of Figure 5.1 we show the evolution of the linear growth factor  $D_+$  for all four cosmological models. The transfer functions for  $\Lambda$ CDM have been produced using CAMB (Lewis and Bridle, 2002), while the transfer functions for the coupled dark energy models are obtained by weighting the  $\Lambda$ CDM transfer functions with the  $D_+$  of the coupled model. we created all initial conditions by using the same random seeds, in order to be able to identify structures among the models.

Initial conditions were then evolved with the code GADGET-2 described in Section 3.2.2. The right panel of Figure 5.1 shows the ratio between the mass functions for the coupled dark energy cosmologies with the one from  $\Lambda$ CDM for redshifts  $z = 2, 1, 0$  for the 80 Mpc/h boxes.

We then chose four dark matter halos in the  $\Lambda$ CDM 80 Mpc/h box and one dwarf halo in the  $\Lambda$ CDM 12 Mpc/h box, and looked for their corresponding realizations in the coupled dark energy simulations. Halos were chosen so

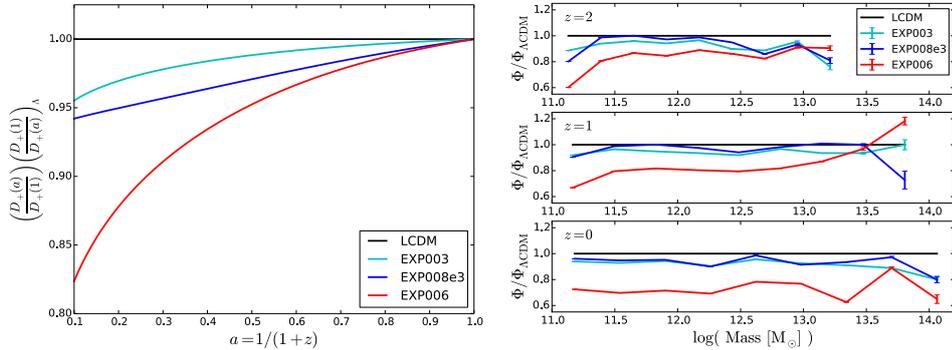


Figure 5.1: The left panel shows the linear growth factor evolutions for all cosmologies normalized to today’s values divided by the  $\Lambda$ CDM evolution. The right panel shows the ratio between the mass functions for the coupled dark energy cosmologies and the one from  $\Lambda$ CDM for redshifts  $z = 2, 1, 0$  for the cosmological boxes of size 80 Mpc/h.

that no other halos with comparable masses were found within four of their virial radii. We then re-ran the cosmological boxes with increased resolution in a Lagrangian volume that includes all particles that at  $z = 0$  were found in three virial radii of each selected halo.

The final sample is composed of three Milky-Way-size halos (halo $\alpha$ , halo $\beta$  and halo $\gamma$ ), a  $6 \times 10^{11} M_\odot$  halo (halo $\delta$ ) and a dwarf halo (halo $\epsilon$ ). For more details on the halos properties at  $z = 0$  see Table 5.1. For the halo identification we used the code Amiga Halo Finder (Knollmann and Knebe, 2009).

The softening lengths are chosen to be  $1/40$  of the intra-particle distance in the low resolution simulation divided by the refinement factor RF (see Section 3.1.1 for details on refinements);  $\text{RF} = 15$  for halo $\alpha$ , halo $\beta$  and halo $\epsilon$ ,  $\text{RF} = 24$  for halo $\gamma$  and halo $\delta$ . Precisely, the softening lengths are 0.54 kpc for halo $\alpha$  and halo $\beta$ , 0.34 kpc for halo $\gamma$  and halo $\delta$ , 0.081 kpc for halo $\epsilon$ . The particle masses at  $z = 0$  in the high resolution volumes are  $3.8 \times 10^5 M_\odot$  for halo $\alpha$  and halo $\beta$ ,  $9.4 \times 10^4 M_\odot$  for halo $\gamma$  and halo $\delta$ ,  $1.3 \times 10^3 M_\odot$  for halo $\epsilon$ . Figure 5.2 shows the projected density maps of the four most massive halos for each cosmological model. We will discuss the dwarf halo in Section 5.4. For the density maps and throughout the paper we chose to calculate halo properties using  $R_{200}$ , radius at which the density is 200 times the critical density  $\rho_c$ , with  $\rho_c \equiv 3H^2/(8\pi G)$ .

	$M_{200}$ [ $M_{\odot}$ ]	$R_{200}$ [kpc]	$c \equiv R_{200}/r_s$	$N_{200}$
<b>halo<math>\alpha</math></b>				
$\Lambda$ CDM	$2.6 \times 10^{12}$	284	11.8	$6.8 \times 10^6$
EXP003	$2.5 \times 10^{12}$	281	9.1	$6.6 \times 10^6$
EXP008e3	$2.6 \times 10^{12}$	282	10.2	$6.7 \times 10^6$
EXP006	$2.1 \times 10^{12}$	265	4.6	$5.5 \times 10^6$
<b>halo<math>\beta</math></b>				
$\Lambda$ CDM	$2.5 \times 10^{12}$	278	10.7	$6.3 \times 10^6$
EXP003	$2.2 \times 10^{12}$	267	8.0	$5.7 \times 10^6$
EXP008e3	$2.2 \times 10^{12}$	268	8.7	$5.8 \times 10^6$
EXP006	$1.7 \times 10^{12}$	246	4.3	$4.5 \times 10^6$
<b>halo<math>\gamma</math></b>				
$\Lambda$ CDM	$9.7 \times 10^{12}$	204	10.8	$1.0 \times 10^7$
EXP003	$9.3 \times 10^{12}$	201	8.6	$9.9 \times 10^6$
EXP008e3	$9.5 \times 10^{12}$	203	9.6	$1.0 \times 10^7$
EXP006	$7.6 \times 10^{12}$	188	3.2	$8.1 \times 10^6$
<b>halo<math>\delta</math></b>				
$\Lambda$ CDM	$6.4 \times 10^{11}$	177	13.3	$6.8 \times 10^6$
EXP003	$5.6 \times 10^{11}$	170	9.7	$6.0 \times 10^6$
EXP008e3	$5.9 \times 10^{11}$	172	11.0	$6.3 \times 10^6$
EXP006	$5.3 \times 10^{11}$	166	4.7	$5.6 \times 10^6$
<b>halo<math>\epsilon</math></b>				
$\Lambda$ CDM	$4 \times 10^9$	33	15.3	$3.1 \times 10^6$
EXP006	$3 \times 10^9$	30	6.6	$2.4 \times 10^6$

Table 5.1: Physical properties of the five halos in all cosmologies,  $\Lambda$ CDM, EXP003, EXP008e3 and EXP006. We show mass at  $R_{200}$ ,  $R_{200}$ , concentrations and number of particles within  $R_{200}$ .

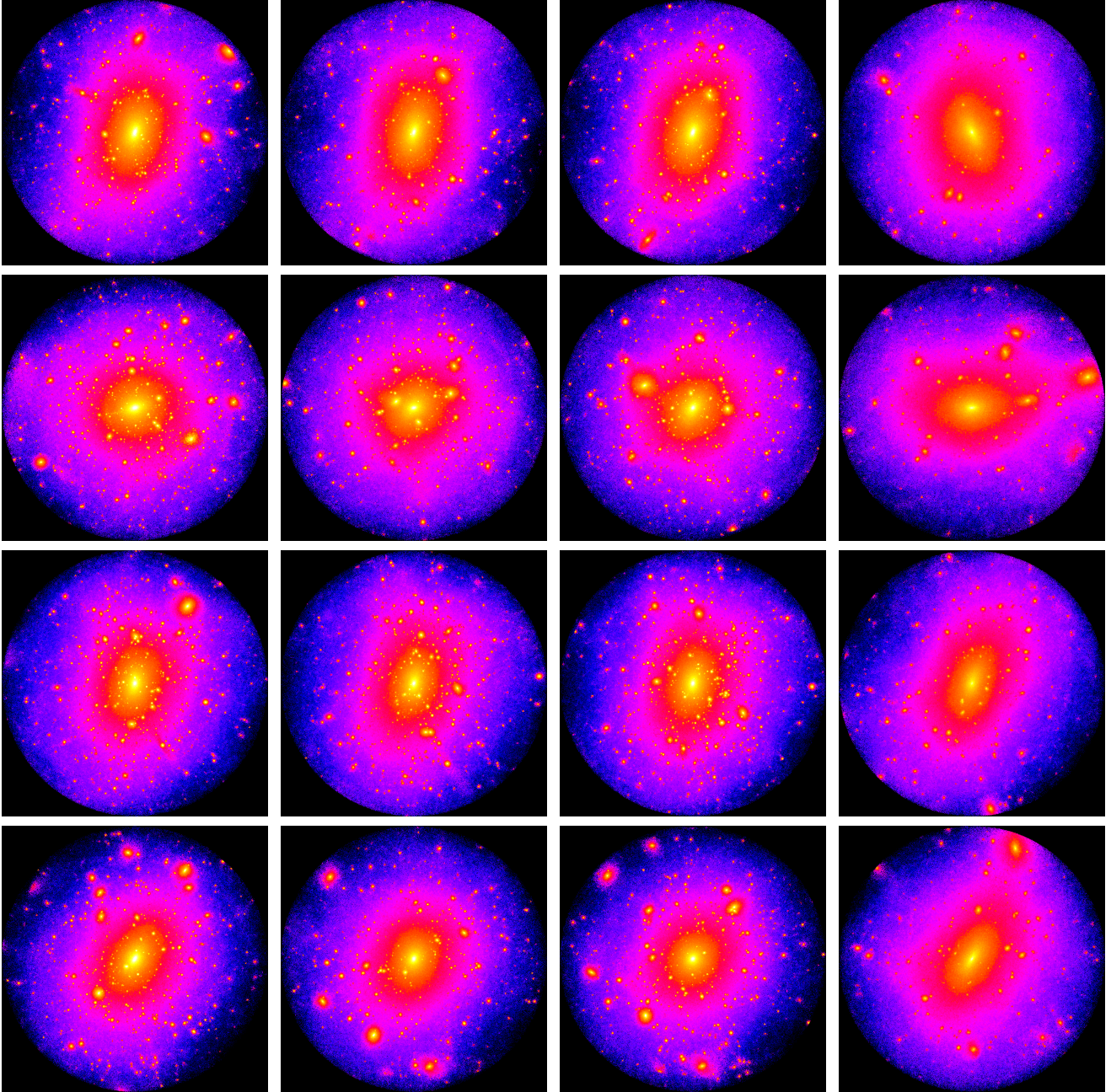


Figure 5.2: Projected density maps of our sample at  $z = 0$ . From first row to last we are showing halo $\alpha$ , halo $\beta$ , halo $\gamma$ , halo $\delta$ ; from first column to last we are showing  $\Lambda$ CDM, EXP003, EXP008e3 and EXP006 cosmologies.

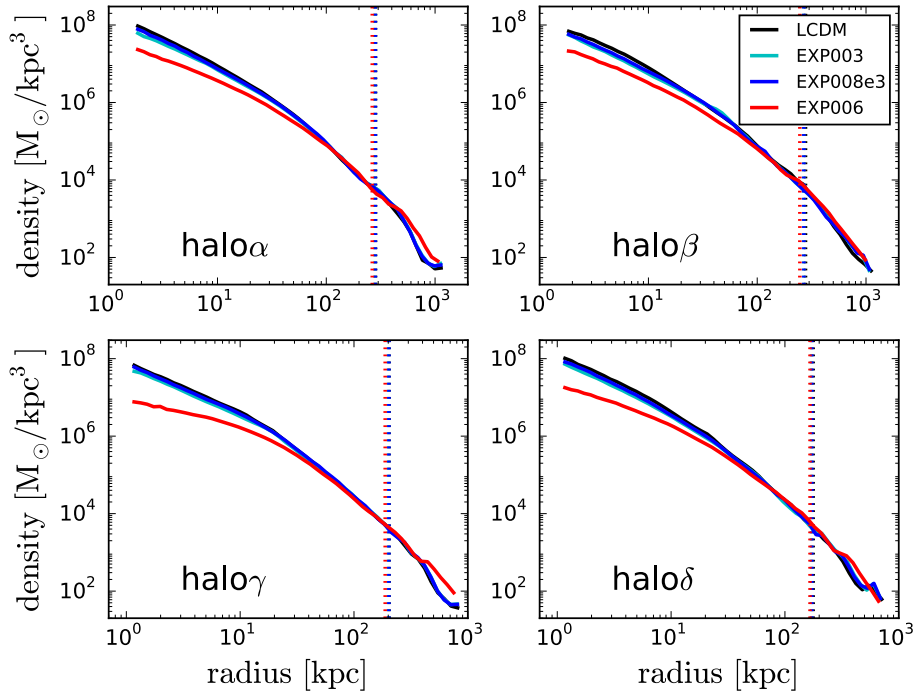


Figure 5.3: Density profiles for halo $\alpha$ , halo $\beta$ , halo $\gamma$  and halo $\delta$  at  $z = 0$ , each for  $\Lambda$ CDM (black), EXP003 (cyan), EXP008e3 (blue) and EXP006 (red). The inner radius is equal to three times the softening length, while the outer radius is four times  $R_{200}$  of each halo. The vertical dashed lines mark  $R_{200}$  for each halo in each cosmology.

## 5.3 Results on Milky-Way size Halo simulations

### 5.3.1 Host Halos Properties

We will first outline the properties of the four most massive halos, halo $\alpha$ , halo $\beta$ , halo $\gamma$  and halo $\delta$ , by showing concentrations, density profiles, rotation curves, evolution of the scale radii and accretion histories.

#### Concentrations and Density Profiles

By introducing a coupling between dark matter and dark energy, halo concentrations decrease. This was also shown in Baldi et al. (2010), Li and Barrow (2011), and Carlesi et al. (2014) for halos with masses  $M \gtrsim 10^{13} M_{\odot}$ . We investigate mass scales  $M \lesssim 10^{12} M_{\odot}$ . The resolution that we are able to reach is higher thanks to the multi-mass technique. In Table 5.1 we show the concentration values for each halo, for which we use the definition

$$c \equiv R_{200}/r_s, \quad (5.2)$$

---

where  $R_{200}$  is the radius at which the density equals 200 times the critical density and  $r_s$  is the scale radius in the Navarro Frenk and White (NFW) profile (Navarro et al., 1997), see Eq. (2.19). We computed  $r_s$  via a  $\chi^2$  minimization procedure using the Levenberg & Marquardt method. In agreement with literature, we find that halos which lived in a coupled dark energy cosmology have lower concentrations. Figure 5.3 shows the density profiles for halo $\alpha$ , halo $\beta$ , halo $\gamma$  and halo $\delta$ . The behavior of the profiles as a function of cosmology is maintained for all four halos, with a significant flattening of the inner part of the profiles only for the extreme coupled cosmology EXP006, while differences are less evident in the EXP003 and EXP008e3 halos. Interestingly, the EXP006 realization of halo $\gamma$  ( $M = 7.6 \times 10^{11} M_\odot$ ) produces a much flatter halo profile, with slope  $\alpha = -0.8$ , which falls out of NFW parametrization. On the other hand, all other profiles of halo $\alpha$ , halo $\beta$ , halo $\gamma$  and halo $\delta$  in all cosmologies are well described by the NFW profile.

Additionally, in Figure 5.4 we show the rotation curves at  $z = 0$  for the four halos. For models within the observational constraints the rotation curves are not significantly affected. The only case in which we observe a considerable flattening is the extreme model EXP006, for all four cases. This is in agreement with results from disc galaxies simulations in dynamical dark energy in Section 4.2.2, where we find that differences in rotation curves among models within observational constraints for dynamical dark energy are not significant in the dark matter only case. On the contrary, in hydrodynamical simulations we find observable differences in rotation curves due to the effects of baryons which enhance the variations in the dark matter accretion. We expect the same enhancement also in coupled dark energy models once hydrodynamics is taken into account. We leave this aspect to be investigated in a future work.

### NFW Scale Radius Evolution

In Section 5.3.1 we have showed that halos that form in a coupled dark energy cosmology with a high value for the coupling constant have concentrations that are significantly lower at  $z = 0$ . Given that almost all halos are well described by a NFW density profile, it means that their NFW scale radii  $r_s$  are much larger than the scale radii of the corresponding  $\Lambda$ CDM realizations. In Figure 5.5 we show the behavior of the scale radius  $r_s$  as a function of redshift for halo $\beta$  in all four cosmologies; the other Milky-Way size halos have similar behaviors. Compared to the  $\Lambda$ CDM case, halos which live in coupled dark energy cosmologies show a larger scale radius at all redshifts.

### Parent Halos Accretion Histories

In order to investigate the origin of the different concentrations, especially in the EXP006 cosmology, in this Section we concentrate on the halo forma-

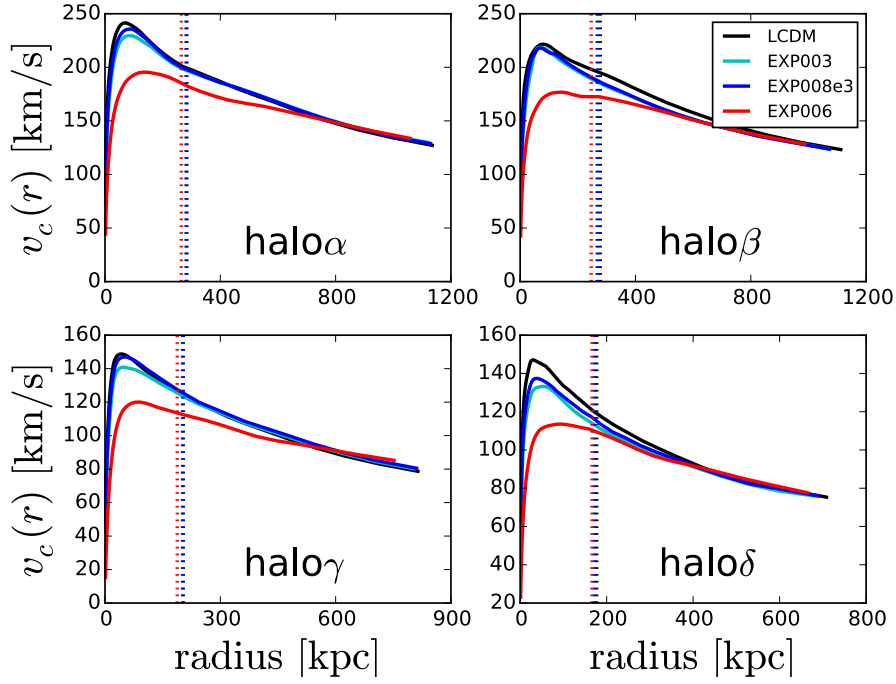


Figure 5.4: Rotation curves for halo  $\alpha$ , halo  $\beta$ , halo  $\gamma$  and halo  $\delta$  at  $z=0$ , each for  $\Lambda$ CDM, EXP003, EXP008e3 and EXP006. The inner radius is equal to three times the softening length, while the outer radius is four times  $R_{200}$  of each halo. The vertical dashed lines mark  $R_{200}$  for each halo in each cosmology.

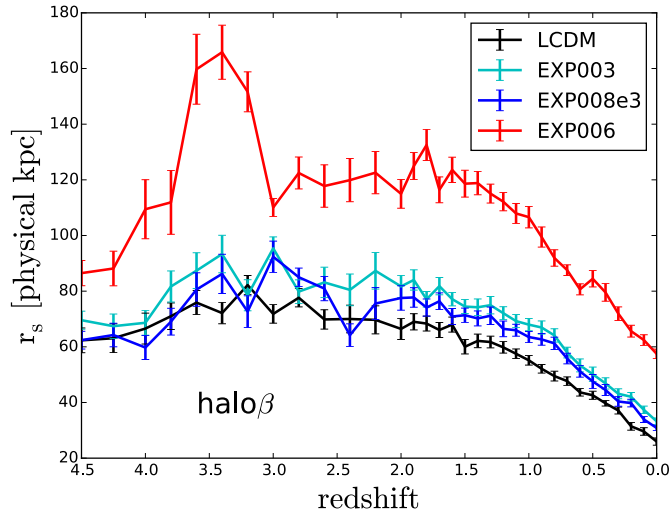


Figure 5.5: Scale radius obtained by fitting an NFW density profile using the Levenberg & Marquart method for halo  $\beta$  as a function of redshift.

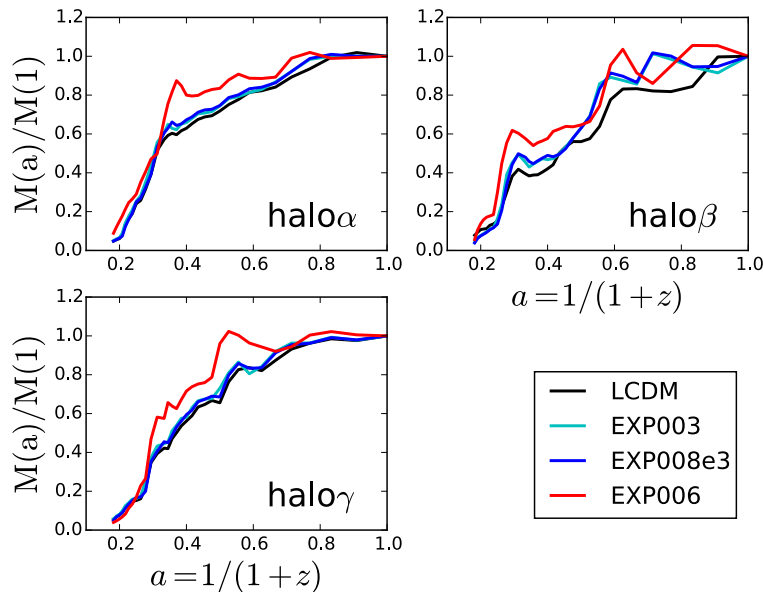


Figure 5.6: Evolution of the mass enclosed in  $R_{200}$  normalized to the mass at  $a = 1$  as a function of the scale factor for  $\text{halo}\alpha$ ,  $\text{halo}\beta$ ,  $\text{halo}\gamma$  in all four cosmologies.

tion times. Firstly, in Figure 5.6 we show the accretion histories, namely the evolution of the mass enclosed in  $R_{200}$  normalized to the value of the mass at  $z = 0$  as a function of expansion factor. Halos growing in  $\Lambda\text{CDM}$ , EXP003 and EXP008e3 cosmologies show similar accretion histories especially for  $\text{halo}\alpha$  and  $\text{halo}\gamma$ ; while halos living in the EXP006 cosmology accrete their mass earlier on compared to their  $\Lambda\text{CDM}$  realizations. Among the three halos, coupled cosmologies runs show unexpected drops in the accretion histories. These would be unusual in a  $\Lambda\text{CDM}$  scenario since halo total masses do not decrease unless it is a temporary effect of a merger (see for instance  $\text{halo}\alpha$  and  $\text{halo}\beta$  around  $a = 0.3$ ). On the other hand, in the case of coupled cosmologies the friction term in Eq. (2.11) is responsible for injecting kinetic energy into the system, which may cause some particles to become gravitationally unbound.

In order to estimate the time of formation for each halo, we followed the approach described in Wechsler et al. (2002). In their paper they show how halo accretion histories are well described by an exponential form that depends on one parameter, the formation epoch  $a_c$ , which is defined as the expansion factor at which the logarithmic derivative of the mass evolution falls below a critical value  $S$ . Specifically, the fitting form is given by

$$\frac{M(a)}{M(1)} = \exp \left[ -a_c S \left( \frac{1}{a} - 1 \right) \right] \quad (5.3)$$

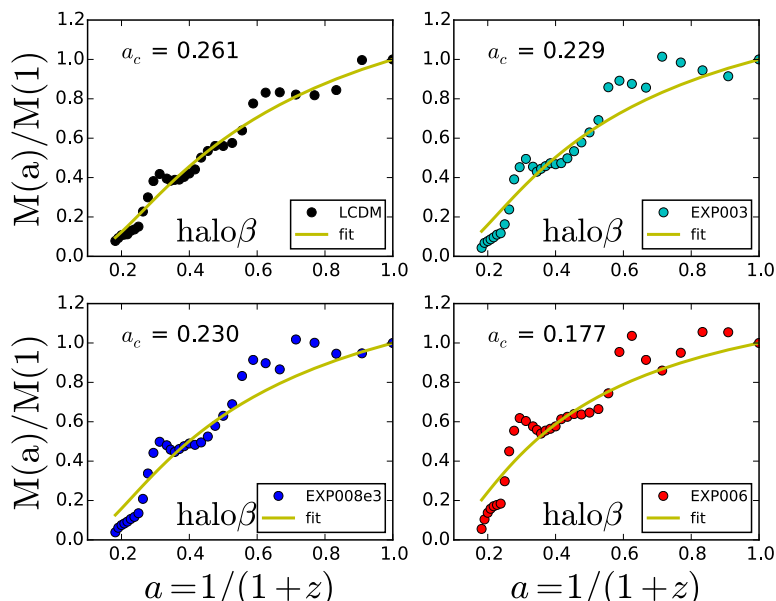


Figure 5.7: Accretion histories for  $\text{halo}\beta$ , where we show for each panel a different cosmological model. The fit to the accretion histories of each realization (solid yellow line) is obtained from Eq. (5.3).

	$\Lambda\text{CDM}$	EXP003	EXP008e3	EXP006
$\text{halo}\alpha$	0.194	0.181	0.183	0.142
$\text{halo}\beta$	0.261	0.229	0.230	0.177
$\text{halo}\gamma$	0.225	0.210	0.215	0.173

Table 5.2: Values for the formation epochs  $a_c$  for  $\text{halo}\alpha$ ,  $\text{halo}\beta$ ,  $\text{halo}\gamma$  in all four cosmologies.

with  $S = 2$ . We used the fitting function of Eq. (5.3) to compute the formation epochs for each of the three halos for all cosmologies. As an example, we show in Figure 5.7 the fitting result for  $\text{halo}\beta$  and we summarize the formation epochs for all halos in Table 5.3.1.

As pointed out in Wechsler et al. (2002), Dutton and Macciò (2014) and Ludlow et al. (2013), in a  $\Lambda\text{CDM}$  cosmology an early formation epoch leads to higher concentrations. The same happens for dynamical dark energy cosmologies, e.g. Klypin et al. (2003); Dolag et al. (2004). Interestingly, in coupled dark energy cosmology this behavior is not preserved. Despite the fact that a stronger coupling brings to an earlier halo formation epoch, halo concentrations decrease when the coupling is increased, as clearly visible from the EXP006 realizations. This phenomenon has also been showed in Baldi (2011a), where an analysis of the modifications due to the coupling has been extensively carried out, but the resolution was significantly lower.

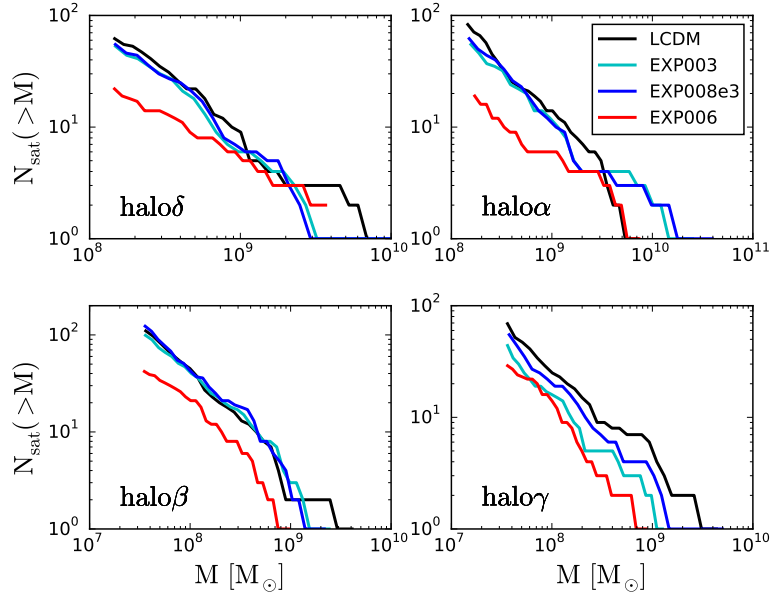


Figure 5.8: Cumulative number of subhalos with more than 400 particles as function of their mass for halo $\alpha$ , halo $\beta$ , halo $\gamma$  and halo $\delta$  at  $z = 0$  for each cosmology.

The friction term in Eq. (2.11) is responsible for making the halo expand by altering its virial equilibrium through the injection of kinetic energy in the system, which in turns lowers the concentration. This shows how in coupled cosmologies the lower concentrations are not the result of formation histories but the effect of the modified dynamics.

### 5.3.2 Subhalos

In this Section we describe the study on subhalo abundance, their radial distribution and circular velocities.

#### Abundance

The lower number of substructures present in EXP006 halos compared to  $\Lambda$ CDM can be recognized in Figure 5.2. In Figure 5.8 we show the subhalo mass function, where only subhalos that lie within  $R_{200}$  and that have more than 400 particles are considered. The total number of subhalos in EXP006 realizations is always from 50 to 75% lower than in the respective  $\Lambda$ CDM cases, while differences between EXP003 and EXP008e3 and  $\Lambda$ CDM are much less evident ( $\sim 10\%$ ). Thus, the missing satellites problem (Klypin et al., 1999; Moore et al., 1999) can be progressively alleviated when increasing the coupling. Note that the differences in the subhalos minimum mass

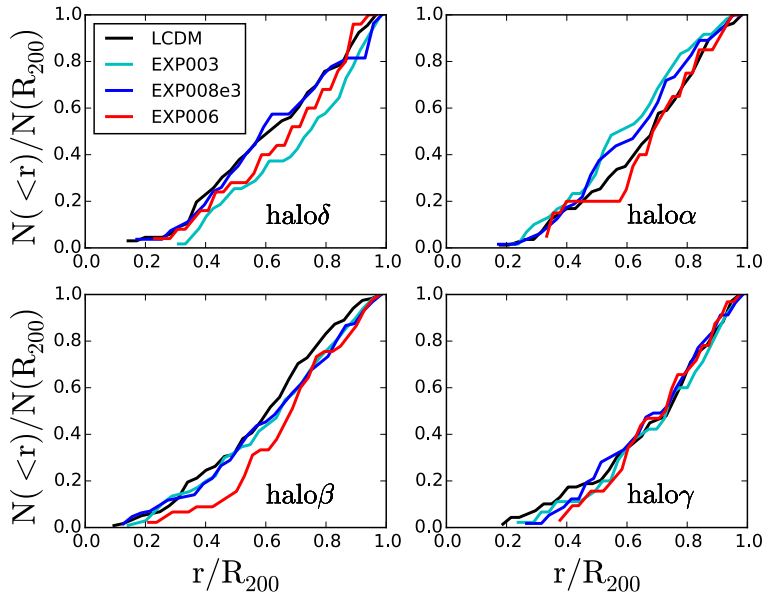


Figure 5.9: Cumulative number of subhalos with more than 400 particles as function of distance from the parent halo center for halo $\alpha$ , halo $\beta$ , halo $\gamma$  and halo $\delta$  at  $z = 0$  for each cosmology.

among halo $\alpha$ , halo $\beta$  and halo $\gamma$ , halo $\delta$  are due to the different resolutions used (see Section 5.2).

### Radial Distribution

Figure 5.9 shows the cumulative distribution of subhalos as a function of the distance from the parent halo center normalized to the total number of subhalos within  $R_{200}$ . All halos in all cosmologies show non-significant differences in the cumulative radial distribution. In order to better understand the distribution of subhalos, Figure 5.10 shows the differential distribution in a sphere of constant radius for all cosmologies, the radii are 350 kpc for halo $\alpha$  and halo $\beta$ , 250 kpc for halo $\gamma$  and 200 kpc halo $\delta$ . The number of bins is kept the same for each halo in all cosmologies and the vertical lines show the virial radii. The distributions show a clear decrease of the number of subhalos in EXP006 halos compared to their respective  $\Lambda$ CDM cases, while for EXP003 and EXP008e3 cosmologies differences are not so evident.

As pointed out in Section 5.3.1, coupled cosmologies decrease halo concentrations thanks to the presence of a friction term in the equation for the evolution of density perturbations, Eq. (2.11), despite the earlier halo formation epochs. We claim that the same effect can be responsible for the lower number of subhalos compared to  $\Lambda$ CDM. Thanks to the extra friction term and to subhalo lower concentrations, subhalos that are falling into the par-

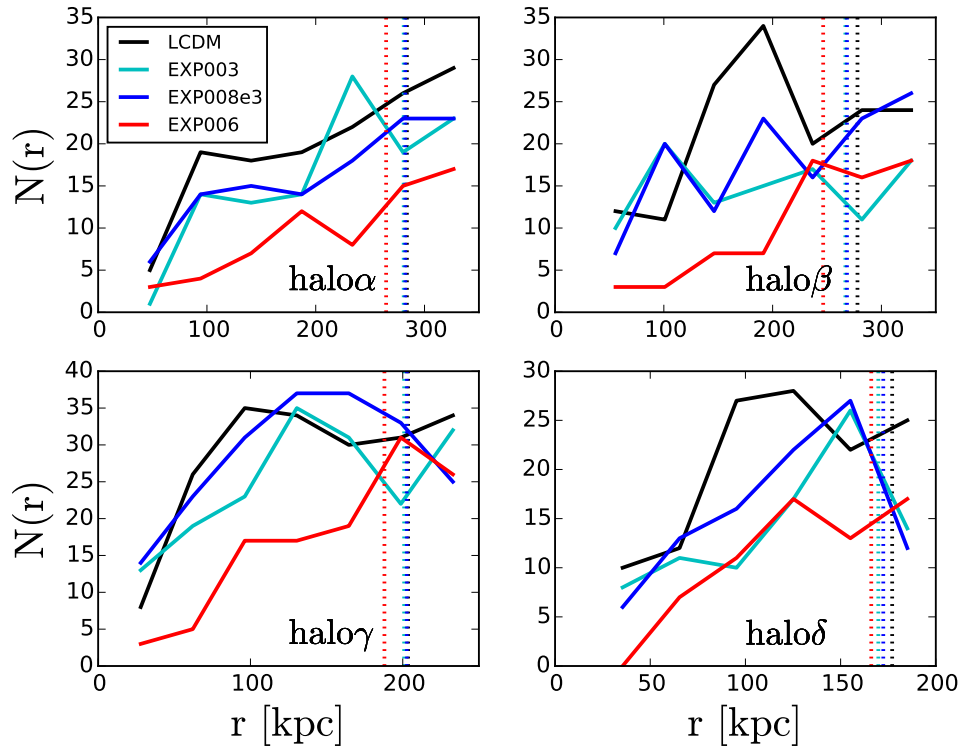


Figure 5.10: Differential number of subhalos in  $R_{200}$  with more than 400 particles as function of distance from parent halo center for  $\text{halo}\alpha$ ,  $\text{halo}\beta$ ,  $\text{halo}\gamma$  and  $\text{halo}\delta$  at  $z = 0$  for each cosmology. The vertical dashed lines mark  $R_{200}$  for each halo in each cosmology. For a given halo, the binning is kept constant for all cosmologies.

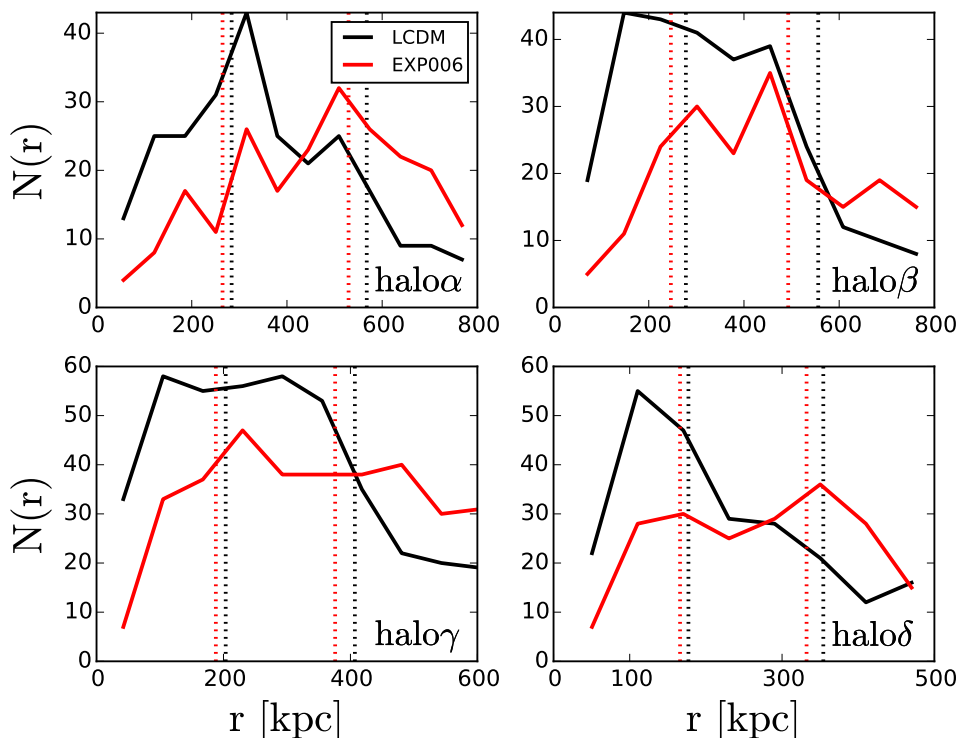


Figure 5.11: Number of subhalos in  $3R_{200}$  with more than 400 particles as function of distance from parent halo center for  $\text{halo}\alpha$ ,  $\text{halo}\beta$ ,  $\text{halo}\gamma$  and  $\text{halo}\delta$  at  $z = 0$  for each cosmology. The vertical dashed lines mark  $R_{200}$  and  $2R_{200}$  for each halo in each cosmology. For a given halo, the binning is kept constant for all cosmologies.

ent halo potential well are more heavily stripped, thus less halos with more than 400 particles survive. If this claim is correct, we should be able to find a difference in the subhalos number distribution when we reach distances from the parent halo center that are bigger than the radius from which the gravitational influence of the host halo is felt. In Figure 5.11 we show the differential radial distribution of the number of subhalos out to about three times the virial radius of each halo. For the sake of clarity, we choose to show only the most extreme cases, EXP006, and  $\Lambda$ CDM for all four halos. The dotted lines represent one and two times  $R_{200}$  for each halo in each cosmology. What we would like to stress, is that there seem to be a decrease in the number of subhalos in halos living in EXP006 cosmology compared to their  $\Lambda$ CDM realizations *only* within the gravitational influence of the parent halo. Between  $1.5$  and  $2 R_{200}$  this behavior inverts and halos living in the strongly coupled cosmology seem to have a larger or at least a comparable number of subhalos with respect to their  $\Lambda$ CDM cases. Thus, we ascribe the presence of a lower subhalos number to a massive stripping effect rather

---

than EXP006 producing intrinsically a lower number of subhalos. We would like to stress on the fact that lowering the number of subhalos can also be achieved by warm dark matter cosmologies (e.g. [Anderhalden et al. 2013](#)), but the fundamental difference lies on the fact that those subhalos in warm dark matter cosmologies were never formed, while in coupled dark energy cosmologies subhalos do form but they are heavily stripped.

### Circular Velocities

[Boylan-Kolchin et al. \(2011\)](#) first showed that N-body simulations of a Milky-Way size halo predict a significant number of subhalos with circular velocities higher than the circular velocities that we measure for the brightest satellites of the Milky Way, which is surprising since these massive subhalos should not fail in producing stars.

The discrepancy between  $\Lambda$ CDM prediction and observations can be alleviated in multiple ways, starting from baryonic processes. [Brooks and Zolotov \(2014\)](#) suggest that baryonic feedback processes could be responsible for a dark matter redistribution, with the result of decreasing the central densities of the most massive subhalos. [Rashkov et al. \(2012\)](#) point out that the possibility of star formation being stochastic below a certain mass would justify the Milky Way having massive dark satellites; furthermore, they highlight the fact that the tension between the Via Lactea II simulation and observations is only a factor of two in mass, which suggests that the uncertainty on the Milky Way virial mass could be a viable way out from the tension ([Vera-Ciro et al., 2013](#); [Kennedy et al., 2014](#)). [Purcell and Zentner \(2012\)](#) showed that there exists a significant variation in subhalo properties even when the host halos have the same virial mass.

Last but not least, the discrepancy can be alleviated by appealing to non- $\Lambda$ CDM cosmologies. The cases for warm, mixed (cold and warm) and self-interacting dark matter are considered respectively in [Lovell et al. \(2012\)](#), [Anderhalden et al. \(2012, 2013\)](#), [Vogelsberger et al. \(2012\)](#). In all cases they find that subhalos are less concentrated due to their late formation time, suggesting that alternative cosmologies can contribute to alleviate the tension between predictions and observations.

Figure 5.12 shows the rotation curves for the twelve most massive subhalos at the moment of infall. We used the correlation between orbital energy and subhalo mass loss found in [Anderhalden et al. \(2013\)](#) to determine the subhalos ranking. [Anderhalden et al.](#) define the binding energy of a subhalo as the sum of the kinetic plus potential energy, divided by the mass of the subhalo

$$e_{\text{orbit}} \equiv K + U = \frac{1}{2} \vec{v}^2 - \frac{GM}{r} \ln \left( 1 + \frac{r}{r_s} \right), \quad (5.4)$$

where  $\vec{v}$  is the velocity of the subhalo with respect to the parent halo center and the parent halo is fitted with an NFW density distribution which gives

its scale radius  $r_s$ . They argue that the ratio  $v_{\max}(z=0)/v_{\max}(z_{\text{infall}})$  is a proxy for the subhalo mass loss since the time of accretion due to tidal stripping and they find it correlates with the subhalo binding energy. In fact, the deeper a subhalo orbits within the potential well of the parent halo, the more tidal stripping it has undergone. This leads to a reduced value of the maximum circular velocity at  $z=0$  relative to the value of velocity at infall. They give the following fitting form:

$$\frac{v_{\max}(z=0)}{v_{\max}(z_{\text{infall}})} = 1 + \xi \cdot e_{\text{orbit}} \quad (5.5)$$

where  $\xi = 2.89 \times 10^{-6} \text{ (km/s)}^{-2}$ . This formula suggests a straight-forward way to calculate the infall velocity once the velocity at  $z=0$  is known.

Each row of Figure 5.12 illustrates the twelve subhalos rotation curves for a given parent halo in all considered cosmologies, from the top down we show halo $\alpha$ , halo $\beta$ , halo $\gamma$ , halo $\delta$ . The observed values for  $v_{\text{circ}}(r_{1/2})$  for the brightest dwarf galaxies orbiting around the Milky Way are shown in yellow. Data are taken from [Anderhalden et al. \(2013\)](#) and references therein. Despite halo $\alpha$  and halo $\beta$  having comparable masses, the tension between simulated curves and measured points in the  $\Lambda$ CDM case is more evident in halo $\beta$ , supporting the fact that subhalo properties can vary even when host halos have the same virial mass ([Purcell and Zentner, 2012](#)). The tension is alleviated in the case of halo $\gamma$  and even more halo $\delta$ , given their lower masses ([Vera-Ciro et al., 2013](#)). Overall, when looking at all halos in EXP003 and EXP008e3 cosmologies these do not show significant improvement compared to their  $\Lambda$ CDM realizations in decreasing the inner densities of subhalos. On the other hand, in the case of EXP006 cosmology, all four halos show such a dramatic decrease in subhalos rotational velocity peaks that rotation curves become incompatible with measured values. The dramatic decrease was to be expected given the choice of a large coupling parameter for EXP006 cosmology, but nonetheless it is useful to understand the effects of the coupling.

## 5.4 Zooming-in on a dwarf halo

To better explore the effects of the coupling at high resolutions, we simulated a dwarf galaxy halo, halo $\epsilon$ . We chose an isolated halo (no structures with comparable mass within four of its virial radii) and, given the results of Section 5.3.2, we only focused on the two most distant cosmological cases,  $\Lambda$ CDM and EXP006 cosmology. The virial masses are respectively  $4 \times 10^9 M_{\odot}$  and  $3 \times 10^9 M_{\odot}$ , with a mass resolution of  $1.3 \times 10^3 M_{\odot}$ . We show in Figure 5.13 the density maps for halo $\epsilon$  in both cosmologies,  $\Lambda$ CDM on the left panel. It is visible how the number of substructures decreases in the case with coupling. In Figure 5.14 we show density profiles and rotation curves for

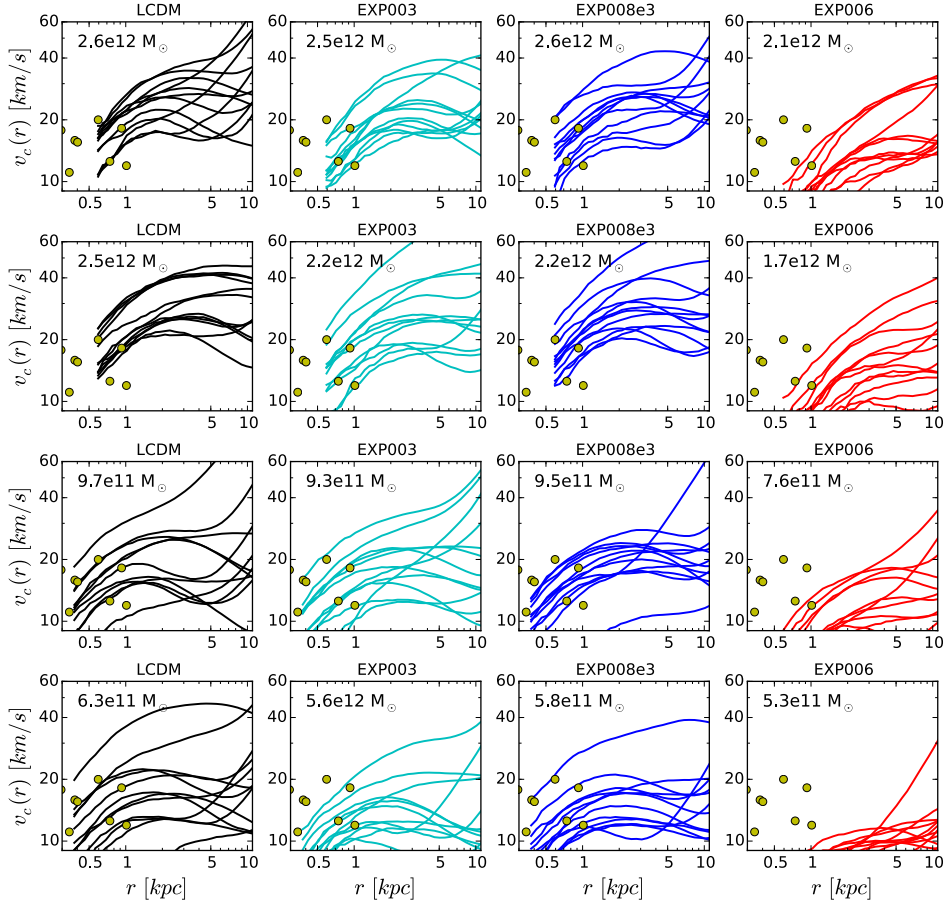


Figure 5.12: Rotation curves of the most massive subhalos at the moment of infall for each halo in each cosmology. From the top row down we show halo $\alpha$ , halo $\beta$ , halo $\gamma$ , halo $\delta$ , from left to right we show  $\Lambda$ CDM (black), EXP003 (cyan), EXP008e3 (blues), EXP006 (red). We estimate the subhalo mass ranking at the moment of infall using the correlation between orbital energy and subhalo mass loss found in [Anderhalden et al. \(2013\)](#). The yellow points are the observed values for  $v_{\text{circ}}(r_{1/2})$  for the brightest dwarf galaxies orbiting around the Milky Way. Data are taken from [Anderhalden et al. \(2013\)](#) and references therein. The masses of each parent halo realization is written on each panel.

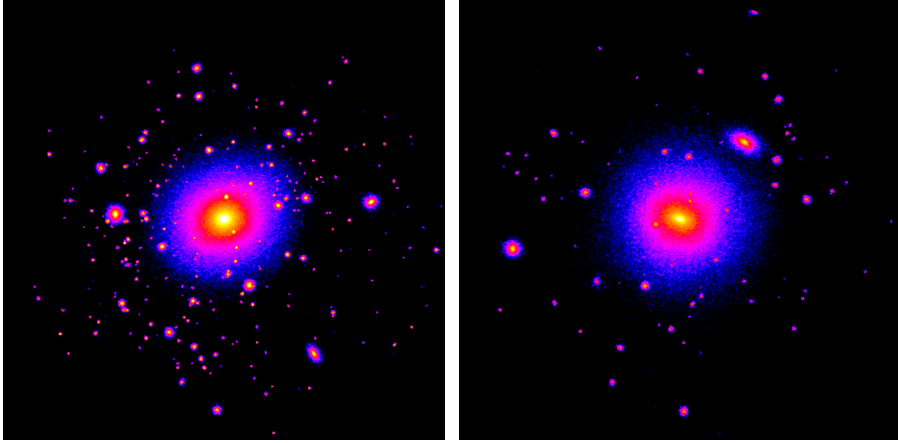


Figure 5.13: Density maps for haloes in  $\Lambda$ CDM (left panel) and in EXP006 cosmology (right panel). The side of each projection is  $2 \times R_{200}$ .

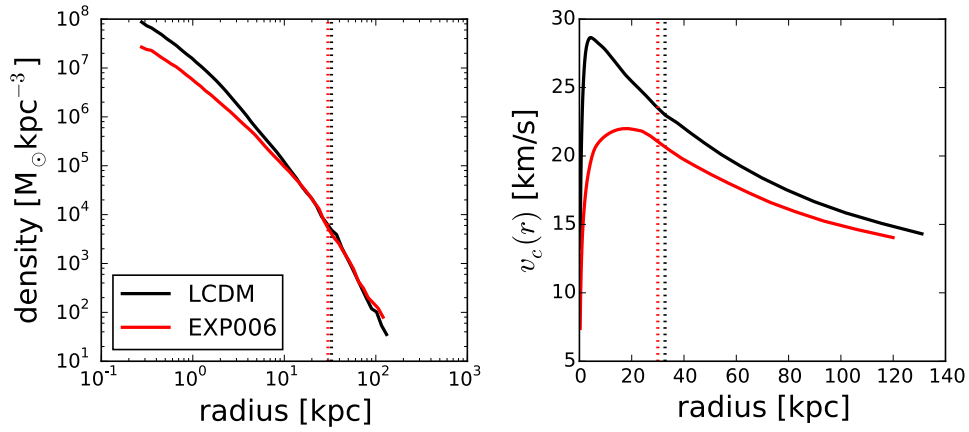


Figure 5.14: Density profiles and rotation curves for haloes in  $\Lambda$ CDM (black) and in EXP006 (red) cosmology. The inner minimum radius is three times the softening length, while the most outer radius is four times  $R_{200}$  respectively. The vertical dashed lines represent  $R_{200}$  for each cosmology.

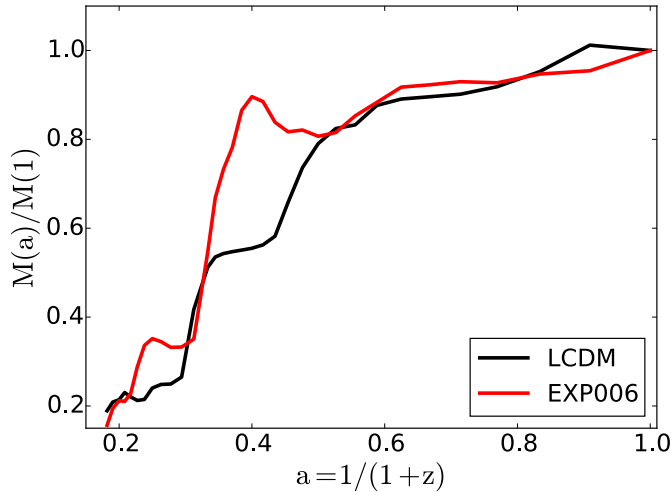


Figure 5.15: Accretion histories for haloes in  $\Lambda$ CDM (black) and in EXP006 (red) cosmology. We show the ratio of  $M_{200}$  at a given time and  $M_{200}$  today as a function of the scale factor.

haloes in both cosmologies. The effect of the coupling is very evident in lowering the concentration and flattening the rotation curve. The values for the halo concentrations are  $c = 15.2$  and  $c = 6.5$  for  $\Lambda$ CDM and EXP006 cosmology respectively. Although the density profile in the coupled dark energy case is less concentrated, it is still cuspy, showing that in coupled cosmologies, as in  $\Lambda$ CDM, we are not able to produce a dark matter only cored density profile. The inconsistency with observation thus still persists, given the observational evidence that supports cored density profiles for the satellites of the Milky Way (Walker and Peñarrubia, 2011; Amorisco and Evans, 2012; Amorisco et al., 2013). Interesting to note, by constructing a model in which both warm and cold dark matter are present and only the cold component is coupled to dark energy, a very high value ( $\beta_c \sim 10$ ) for the coupling constant is favored (Bonometto et al., 2015) and simulated dark matter only dwarf halos show a cored density profile (Macciò et al., 2015). Figure 5.15 shows accretion histories, the ratio of  $M_{200}$  to its value today is plotted as function of scale factor. As in Section 5.3.1, we calculated the formation epochs as in Wechsler et al. (2002) and obtained  $a_c = 0.191$  ( $\Lambda$ CDM),  $a_c = 0.146$  (EXP006), confirming the finding that coupled dark energy models have earlier formation times, also for less massive halos.

## 5.5 Conclusions

We have outlined the first study in coupled dark energy cosmologies on high resolution simulations on galactic scales, with the aim to study the effects

of the coupling between dark energy and dark matter on these scales, so far neglected in previous works. We investigated two viable models, one with constant coupling and one with varying coupling with redshift; we also chose a third case where the constant coupling value has been pushed beyond observational constraints to better investigate its effects. We then selected three Milky-Way size halos, a  $6 \times 10^{11} M_{\odot}$  halo and a dwarf halo  $5 \times 10^9 M_{\odot}$ , and studied their properties in a  $\Lambda$ CDM reference model and in the coupled cosmologies, resolving each halo with  $\sim 10^6$  particles.

We computed concentrations and formation epochs for all halos and we find that, despite the earlier formation epochs of the coupled cosmologies halos, these have lower concentrations. In a  $\Lambda$ CDM or a dynamical dark energy scenario, earlier formation epochs would imply higher concentrations, but in the coupled dark energy case the reason for lower concentrations is not related to formation histories, but rather to the modified dynamics. In fact, the equation for the linear evolution of density perturbations, Eq. (2.9), shows the friction term  $-\beta_c \dot{\phi} \dot{\delta}_c$ , an extra term compared to the  $\Lambda$ CDM case that redistributes the dark matter particles and lowers the central densities, despite the earlier formation times (see Baldi 2011a). We find that this behavior is reproduced for all mass scales that we have investigated.

In particular, subhalos can also be significantly less concentrated. When falling towards their host, they are more heavily stripped once they start feeling the gravitational influence of the host halo. This translates into decreasing the number of subhalos compared to the  $\Lambda$ CDM realization and, additionally, subhalos are themselves less massive and less concentrated. For these reasons, coupled cosmologies can be helpful in alleviating satellite-scales inconsistencies of  $\Lambda$ CDM. On the other hand, we find that, in order to try to solve these issues with the coupling alone, one needs to use an extreme value for the coupling constant that is ruled out by observational constraints. In fact, only in the case with the highest coupling value the number of subhalos is significantly reduced (up to 75% less subhalos) than in the respective  $\Lambda$ CDM cases, while for the viable coupling cosmologies the decrease is much less significant (10% less subhalos). Moreover, we find that the distribution of the subhalos inside the parent halo virial radius does not vary significantly among cosmologies.

Less concentrated coupled cosmologies subhalos can in principle be useful to reconcile the inconsistency between the observed properties of the Milky Way dwarf galaxies and  $\Lambda$ CDM simulations predictions, but once more a high enough value for the coupling must be assumed. Interestingly, allowing the introduction of massive neutrinos does alleviate the constraints on the coupling (see e.g. La Vacca et al., 2009), leaving coupled dark energy models dynamics on sub-galactic scales an interesting option.

Overall coupled dark energy models can be as effective as  $\Lambda$ CDM in reproducing observations on sub-galactic scales and, for specific choices of the coupling, they can improve the agreement between predicted and observed

---

properties. Hence, coupled models would need to be further investigated, possibly taking into account the effects of baryons at sub-galactic scales, which, as already shown in dynamical dark energy models (Section 4.2), are expected to amplify differences observed in the dark matter only case.

## Chapter 6

# Summary and Conclusions

Since it was realized that an extra term in Einstein's fields equations was needed to explain the acceleration of the universe, alternatives to a Cosmological Constant have been proposed and dark energy models largely developed. In this thesis, we focused on two of the most popular choices nowadays available in literature, Dynamical Dark Energy ([Wetterich, 1988](#)) and Coupled Dark Energy ([Amendola, 2000](#)).

Dynamical dark energy only affects the background evolution of the universe and various geometry probes can be used to constrain the model parameters (e.g. luminosity distance, angular-diameter distance, baryonic acoustic oscillations). In turn, the change in background evolution affects the linear growth factor, with the result that structure formation is sped up or slowed down compared to  $\Lambda$ CDM ([Klypin et al., 2003](#)). Coupled dark energy exhibits similar changes to the background evolution as dynamical dark energy, but, additionally, an extra force between dark energy and dark matter alters the equation for the evolution of linear perturbations. As a consequence, the modified dynamics further influence structure and galaxy formation ([Macciò et al., 2004](#)).

Thus, structure formation and evolution can show significant departures from a  $\Lambda$ CDM model. For this reason, it is extremely useful to compare predictions of dark energy models with observations, which can range from cosmologically large scales to the highly non-linear end of the power spectrum down to galactic and sub-galactic scales. Given that formation of structures is a strongly non-linear process, numerical simulations need to be employed to obtain detailed predictions. Furthermore, when investigating galactic scales, baryonic effects play a significant role and should not be overlooked. Modeling the luminous matter is necessary for a consistent comparison with observations but treating hydrodynamical processes is a very challenging task. Nonetheless, understanding the role of baryonic matter in shaping differences among cosmologies is crucial to make use of the very high resolution data coming from the next generation of galaxy surveys.

---

Dynamical dark energy and coupled dark energy have been extensively tested both at linear level and on large-scale predictions, but scarcely investigated on galactic and sub-galactic scales. In this thesis I outlined our work on structure and galaxy formation in both dynamical and coupled dark energy across the mass range  $\sim 10^9\text{--}10^{12} M_\odot$  via dark matter only and hydrodynamical numerical simulations.

Firstly, we developed an initial condition generator suitable for producing initial conditions for multi-mass cosmological simulations in a large variety of non- $\Lambda$ CDM models, GRAFIC2-DE. The code is a generalization of the already available GRAFIC2 (Bertschinger, 2001). Details on initial conditions generator and its extension to non- $\Lambda$ CDM cosmologies were given in Chapter 3.

In Section 4.1 I described our choices for the linear parametrization of the dynamical dark energy equation-of-state parameter  $w \equiv p/\rho$ . Four models plus  $\Lambda$ CDM were selected and used throughout Chapter 4: waCDM0, waCDM1, waCDM2 and SUCDM. All dynamical dark energy models lie within the two-sigma contours given by WMAP7 data (Komatsu et al., 2011), employ the *same* baryonic physics prescriptions and share the same  $\sigma_8$  at  $z = 0$ . The code used is GASOLINE-DE for hydrodynamical runs (Wadsley et al., 2004), which features gas cooling, supernova feedback and feedback from young massive stars, while PKDGRAV (Stadel, 2001) was used for dark matter only runs. Both codes have implementations that account for the background expansion of a given dynamical dark energy model (Casarini et al., 2011b).

In Section 4.2 I show our results on high resolution hydrodynamical simulations of three single-galaxies with masses  $8 \times 10^{11} M_\odot$ ,  $6 \times 10^{11} M_\odot$  and  $3 \times 10^{11} M_\odot$ . The intention of this work<sup>1</sup> is to investigate the effects of dark energy on galactic scales in hydrodynamical simulations. We find that the same galaxy evolved in different dark energy cosmologies does not present significant differences in dark matter only simulations, while in hydrodynamical simulations galactic properties vary greatly. By changing the dark energy parametrization, stellar mass either decreases or increase of a factor around two throughout the whole galaxy evolution. Baryons amplify differences among dynamical dark energy models due to their non-linear response in hydrodynamical processes. Cosmological models set the initial differences in density perturbations, but these are not sufficient to produce significant changes in galaxies unless feedback processes start enhancing those differences by producing slightly more (or less) stars. More stars introduce more metals in the feedback cycle and more metals decrease the cooling time, which in turn allows gas to cool faster and produce even more stars. Through

---

<sup>1</sup> Published in Penzo et al. (2014)

the highly non-linear response of baryons, dark energy models that would have been indistinguishable from  $\Lambda$ CDM on galactic scales show distinctive features in hydrodynamical simulations. We find that, by changing the dark energy model, we are able to delay and suppress (or anticipate and increase) star formation until recent epochs. The delay in star formation is then in turn responsible for flattening rotations curves. We find a significant change, about 100 km/s, in the two most massive galaxies that we considered.

We compare the effect of dynamical dark energy with the effect of baryonic feedback on disc galaxies. We keep the cosmology fixed (waCDM2) and change the feedback parametrization. Provided that supernova feedback is kept constant, at late times the effect of dark energy is comparable to the effect of feedback from young massive stars. Also the degree at which stellar feedback is able to flatten rotation curves is comparable to the effect of dark energy. On the other hand, at high redshift, the effect of feedback from young massive stars becomes more significant than the dark energy modeling. Nonetheless, the importance of the dark energy modeling can be compared to the importance of the details in the feedback parametrization.

The implications of the dynamical dark energy modeling on the formation and evolution of our three high-resolution galaxy simulations are noteworthy and in principle may be reproduced at all mass scales. To check whether this is the case, in Section 4.3 we extend the exercise to hydrodynamical simulations of a cube of the universe with side 114 Mpc. This is a hydrodynamical simulation with the same feedback implementation used in Section 4.2, with the difference that resolution is constant throughout the box and hydrodynamics are treated in the full volume. Due to the high computational cost of such settings, the resolution had to be much lower than in the single-object cases. In fact, the high resolution of single-galaxy runs makes it possible to simulate only a few tens of objects. When interested in a larger sample ( $\sim$  thousands of objects), single-galaxy simulations can no longer be employed. With a hydrodynamically simulated volume we can study the effects of dynamical dark energy on galaxy formation across a wider range of galaxy masses, environments and merger histories.

In the galaxy sample contained in our cosmological volumes the increase in the mean stellar mass given a halo mass is at most 20% in SUCDM, our most distant model from  $\Lambda$ CDM, while for our three single-galaxy simulations the increase reaches 100%. We attribute the lower differences among cosmologies compared to the single-galaxy runs to the change in resolution. In fact, in order for baryonic feedback processes to be well sampled and fuel the feedback cycle, they require a high enough resolution. For comparison, the mass resolution of the most refined of the two sets of volumes ( $N_p = 512^3$ ) is for gas particles (initial masses)  $m_{\text{gas}} = 6.9 \times 10^7 M_\odot$ , while in the single-galaxy runs  $m_{\text{gas}} = 4.2 \times 10^9 M_\odot$ . To support the resolution argument, we ran one of the single-galaxy simulations with a resolution for gas particles  $m_{\text{gas}} = 2.7 \times 10^7 M_\odot$  and differences between cosmologies became comparable

---

to the differences found in the hydrodynamical volumes.

Our work<sup>2</sup> on the cosmological volumes in dynamical dark energy diverted the focus onto resolution and underlined its crucial role in differentiating between dynamical dark energy models. In particular, we argued that resolution in our volume simulations may not be sufficient to disentangle between cosmological models at dwarf galaxy mass scales where we find a variation in the mean stellar mass from  $\Lambda$ CDM of only a few percents. In the higher resolution volume ( $N_p = 512^3$ ), a  $\sim 10^{10} M_\odot$  galaxy is described with a total of about 100 particles.

To investigate whether low resolution is suppressing potential differences between cosmological models or simply differences are intrinsically not present at these mass scales, in Section 4.4 we investigated hydrodynamical simulations of dwarf galaxies in dynamical dark energy. I present a set of four dwarf galaxies with virial masses of a few  $\times 10^9 M_\odot$  evolved in  $\Lambda$ CDM and in the two most distant cosmological models, waCDM2 and SUCDM. In this case a typical  $10^{10} M_\odot$  dwarf galaxy is described with about four million particles within its virial radius and the softening length for stellar and gas particles is 29 pc. We find that the hierarchy of cosmological models is maintained in our four dwarf galaxies, with the SUCDM dwarfs making more stars than  $\Lambda$ CDM and waCDM2, but the difference in stellar mass compared to  $\Lambda$ CDM varies and is significant only in two out of four cases. That differences between cosmological models vary among our four cases is in agreement with the statement that star formation becomes stochastic at these mass scales (Boylan-Kolchin et al., 2011), thus also the enhancement due to baryonic processes of variations between cosmological models is expected to vary.

We find that the waCDM2 realization of the least massive dwarf galaxy does not make any stars and will remain dark throughout its life. This shows that even small departures from  $\Lambda$ CDM can affect the number of luminous subhaloes when their virial mass is around a few  $\times 10^9 M_\odot$ . Star formation histories are globally enhanced or decreased but no delay or anticipation shows at these mass scales. Furthermore, for all our dwarf galaxies, density profiles do not vary between different dynamical dark energy models (differences are less than few percents at inner radii).

I conclude our experiment on dynamical dark energy at dwarf mass scales by stating that cosmology does not have a significant impact on our four dwarf galaxy cases compared to the impact we find on disc galaxies. This is in agreement with expecting higher variations among cosmological models around the peak of star formation efficiency ( $M_{\text{halo}} \sim 10^{12} M_\odot$ ) (Moster et al., 2010).

---

<sup>2</sup> Collaboration with L. Casarini and A. V. Macciò, where L. Casarini was responsible for running the simulations, while I performed the analysis under the supervision of A. V. Macciò

Our findings from dwarf galaxies simulations additionally suggested that scatter in star formation histories within a given cosmological model may be extensive. To better investigate what fuels these different star formation histories, in Section 4.4.4, we increase the dwarf sample and focus on the  $\Lambda$ CDM model<sup>3</sup>. Our goal is to study the properties of dwarf satellites before in-fall into their Milky-Way size parent halo ( $z \sim 1$ ).

Our sample is composed of 22 dwarf galaxies in the mass range a few  $10^9$ – $10^{10} M_{\odot}$ ; 7 out of 13 haloes with masses  $8 \times 10^8 \lesssim M_{\text{halo}}/M_{\odot} \lesssim 4 \times 10^9$  do not form any stars. The reason for these haloes to remain dark lies in the presence of the UV background radiation from the reionization epoch (Dekel and Silk, 1986). Generally, the sample follows the extrapolation of the stellar mass halo mass relation at  $z = 1$  from abundance matching (Moster et al., 2013), but it suggests a quite large scatter ( $\sim$  a factor of ten) around the extrapolated relation. We find a wide variety of star formation histories, which supports the suggestion that star formation at these mass scales may be stochastic.

We study three dwarf galaxies with comparable masses but diverse star formation histories and, as a consequence, different stellar mass at  $z = 1$ . We connect their heterogeneity with their various formation histories. Indeed, we find that what discriminates haloes with comparable masses is whether they underwent recent major mergers or not. At these mass scales, major mergers are the cause for a massive increase in star formation ( $\sim 85\%$  of the stellar mass is produced during the merger).

In Chapter 5 I describe our work on structure formation on galactic and sub-galactic scales in dark matter only simulations in coupled dark energy<sup>4</sup>. I start by describing our choices of coupling functions in a scenario in which dark matter and dark energy interact with each other. This class of models features interesting departures from the  $\Lambda$ CDM scenario, (*i*) an enhancement of the gravitational strength, (*ii*) a dark matter particle mass that changes with time as a function of the dark energy scalar field, (*iii*) a friction term that introduces a velocity dependence in the acceleration equation for dark matter particles (Amendola, 2000). We investigate two viable models (Pettorino et al., 2012), one with constant coupling and one with varying coupling with redshift; we also choose a third case where the constant coupling value is pushed beyond observational constraints to better investigate its effects.

We run single-object simulations of five dark matter haloes, precisely three Milky-Way size haloes, a  $6 \times 10^{11} M_{\odot}$  halo and a dwarf halo  $5 \times 10^9 M_{\odot}$ . These cosmologies have been previously studied in large volume simulations (Baldi et al., 2010; Carlesi et al., 2014), but, before this work, the effects of the coupling were never investigated at the aforementioned mass scales

---

<sup>3</sup> A. V. Macciò, C. Penzo et al. in preparation

<sup>4</sup> Penzo et al. (2015) submitted, arXiv:1504.07243

---

and at such high resolutions (each halo has a few million particles within the virial radius). Given that inconsistencies with a  $\Lambda$ CDM model appear mostly at sub-galactic scales (Klypin et al., 1999; Moore et al., 1999; Boylan-Kolchin et al., 2011), exploring the behavior of coupled dark energy models at these scales becomes of interest.

We compute concentrations and formation epochs for all haloes and we find that, despite the earlier formation epochs of the coupled cosmologies haloes, these have lower concentrations. In a  $\Lambda$ CDM or a dynamical dark energy scenario, earlier formation epochs would imply higher concentrations, but in the coupled dark energy case the reason for lower concentrations is not related to formation histories, but rather to the modified dynamics. In fact, the friction term redistributes the dark matter particles and lowers the central densities, despite the earlier formation times (Baldi, 2011a). We find that this behavior is reproduced for all haloes that we have investigated.

As a consequence of the lower concentration, when falling into the parent halo subhaloes are more heavily stripped in coupled cosmologies compared to  $\Lambda$ CDM. The heavy stripping is responsible for decreasing the number of subhalo orbiting a Milky-Way size halo and is proportional to the strength of the coupling. In our two models with coupling values within the observational constraints the decrease is of about 10%, while in the extreme model the decrease reaches 75%. Given that the high number of subhaloes predicted from  $\Lambda$ CDM simulations has been a concern in the last decade, a cosmological model that tends to alleviate the tension even before appealing to baryonic effects is undoubtedly useful to improve the matching with observations.

All subhaloes are heavily stripped in coupled cosmologies. Thus, subhaloes that succeeded in forming stars will be less massive than their equivalent subhaloes in  $\Lambda$ CDM. As a consequence, we find that these dwarf haloes show rotation curves that are flatter and lower than the dwarf haloes that reside in a  $\Lambda$ CDM Milky-Way parent halo. This can help in matching observational constraints from velocity dispersions of the Milky Way satellites (Wolf et al., 2010). In the light of the results from Chapter 4, also in this case the effects of baryons should be taken into account. We plan to explore this aspect in a future work.

Less concentrated subhalos of coupled cosmologies can in principle be useful to reconcile the inconsistency between the observed properties of the Milky Way dwarf galaxies and  $\Lambda$ CDM predictions from simulations, but a value for the coupling outside of observational constraints must be assumed. Interestingly, allowing the introduction of massive neutrinos alleviates these constraints (see e.g. La Vacca et al., 2009) and suggests that dynamics on sub-galactic scales in coupled dark energy models leave interesting options open.

To conclude, considering what our study covered, both dynamical dark

energy and coupled dark energy are plausible alternatives to  $\Lambda$ CDM. We showed that specific parameter choices can even improve the match with observations. Additionally, I hope we have drawn the reader's attention to the important roles played by baryonic processes and by resolution in differentiating between cosmological models. In the era of high precision cosmology, small departures from a cosmological constant do matter and must be further investigated together with baryonic physics.

---

# Bibliography

- Agertz, O., Teyssier, R., and Moore, B. (2011). The formation of disc galaxies in a  $\Lambda$ CDM universe. *MNRAS*, 410:1391–1408.
- Agnello, A. and Evans, N. W. (2012). A Virial Core in the Sculptor Dwarf Spheroidal Galaxy. *ApJ*, 754:L39.
- Alam, S., Albareti, F. D., Allende Prieto, C., Anders, F., Anderson, S. F., Andrews, B. H., Armengaud, E., Aubourg, É., Bailey, S., Bautista, J. E., and et al. (2015). The Eleventh and Twelfth Data Releases of the Sloan Digital Sky Survey: Final Data from SDSS-III. *ArXiv e-prints*.
- Alimi, J.-M., Füzfa, A., Boucher, V., Rasera, Y., Courtin, J., and Corasaniti, P.-S. (2010). Imprints of dark energy on cosmic structure formation - I. Realistic quintessence models and the non-linear matter power spectrum. *MNRAS*, 401:775–790.
- Alpher, R. A., Bethe, H., and Gamow, G. (1948). The Origin of Chemical Elements. *Physical Review*, 73:803–804.
- Alpher, R. A. and Herman, R. (1948). Evolution of the Universe. *Nature*, 162:774–775.
- Amendola, L. (2000). Coupled quintessence. *Phys. Rev. D*, 62(4):043511.
- Amendola, L. (2004a). Linear and nonlinear perturbations in dark energy models. *Phys. Rev. D*, 69(10):103524.
- Amendola, L. (2004b). Linear and nonlinear perturbations in dark energy models. *Phys. Rev. D*, 69(10):103524.
- Amendola, L., Gasperini, M., and Piazza, F. (2004). Fitting type Ia supernovae with coupled dark energy. *Journal of Cosmology and Astroparticle Physics*, 9:14.
- Amendola, L. and Tsujikawa, S. (2010). *Dark Energy: Theory and Observations*. Cambridge University Press.

- 
- Amorisco, N. C., Agnello, A., and Evans, N. W. (2013). The core size of the Fornax dwarf spheroidal. *MNRAS*, 429:L89–L93.
- Amorisco, N. C. and Evans, N. W. (2012). Dark matter cores and cusps: the case of multiple stellar populations in dwarf spheroidals. *MNRAS*, 419:184–196.
- Anderhalden, D., Diemand, J., Bertone, G., Macciò, A. V., and Schneider, A. (2012). The galactic halo in mixed dark matter cosmologies. *Journal of Cosmology and Astroparticle Physics*, 10:47.
- Anderhalden, D., Schneider, A., Macciò, A. V., Diemand, J., and Bertone, G. (2013). Hints on the nature of dark matter from the properties of Milky Way satellites. *Journal of Cosmology and Astroparticle Physics*, 3:14.
- Appel, A. W. (1985). An Efficient Program for Many-Body Simulation. *SIAM Journal on Scientific and Statistical Computing*, vol. 6, no. 1, January 1985, p. 85-103., 6:85–103.
- Baldi, M. (2011a). Clarifying the effects of interacting dark energy on linear and non-linear structure formation processes. *MNRAS*, 414:116–128.
- Baldi, M. (2011b). Time-dependent couplings in the dark sector: from background evolution to non-linear structure formation. *MNRAS*, 411:1077–1103.
- Baldi, M. (2012a). Early massive clusters and the bouncing coupled dark energy. *MNRAS*, 420:430–440.
- Baldi, M. (2012b). The CoDECS project: a publicly available suite of cosmological N-body simulations for interacting dark energy models. *MNRAS*, 422:1028–1044.
- Baldi, M. and Pettorino, V. (2011). High- $z$  massive clusters as a test for dynamical coupled dark energy. *MNRAS*, 412:L1–L5.
- Baldi, M., Pettorino, V., Robbers, G., and Springel, V. (2010). Hydrodynamical N-body simulations of coupled dark energy cosmologies. *MNRAS*, 403:1684–1702.
- Barnes, J. and Efstathiou, G. (1987). Angular momentum from tidal torques. *ApJ*, 319:575–600.
- Bartelmann, M. (2012). *Cosmology Notes*. Unpublished Lecture Notes.
- Bartelmann, M., Dolag, K., Perrotta, F., Baccigalupi, C., Moscardini, L., Meneghetti, M., and Tormen, G. (2005). Evolution of dark-matter haloes in a variety of dark-energy cosmologies. *ApJ*, 49:199–203.

- Bertschinger, E. (2001). Multiscale Gaussian Random Fields and Their Application to Cosmological Simulations. *ApJS*, 137:1–20.
- Bertschinger, E. and Gelb, J. M. (1991). Cosmological N-body simulations. *Computers in Physics*, 5:164–175.
- Binney, J. and Tremaine, S. (1987). *Galactic dynamics*. Princeton Series in Astrophysics.
- Bonometto, S. A., Mainini, R., and Macciò, A. V. (2015). Strongly Coupled Dark Energy Cosmologies: preserving  $\Lambda$ CDM success and easing low scale problems I - Linear theory revisited. *ArXiv e-prints*.
- Boylan-Kolchin, M., Bullock, J. S., and Kaplinghat, M. (2011). Too big to fail? The puzzling darkness of massive Milky Way subhaloes. *MNRAS*, 415:L40–L44.
- Boylan-Kolchin, M., Bullock, J. S., and Kaplinghat, M. (2012). The Milky Way’s bright satellites as an apparent failure of  $\Lambda$ CDM. *MNRAS*, 422:1203–1218.
- Brandt, A. and Lubrecht, A. A. (1990). Multilevel Matrix Multiplication and Fast Solution of Integral Equations. *Journal of Computational Physics*, 90:348–370.
- Brax, P. H. and Martin, J. (1999). Quintessence and supergravity. *Physics Letters B*, 468:40–45.
- Brook, C. B., Di Cintio, A., Knebe, A., Gottlöber, S., Hoffman, Y., and Yepes, G. (2013a). The stellar-to-halo mass relation for Local Group galaxies. *ArXiv e-prints*.
- Brook, C. B., Stinson, G., Gibson, B. K., Shen, S., Macciò, A. V., Wadsley, J., and Quinn, T. (2013b). The MaGICC Baryon Cycle: The Enrichment History of Simulated Disc Galaxies. *ArXiv e-prints*.
- Brook, C. B., Stinson, G., Gibson, B. K., Wadsley, J., and Quinn, T. (2012). MaGICC discs: matching observed galaxy relationships over a wide stellar mass range. *MNRAS*, 424:1275–1283.
- Brooks, A. M. and Zolotov, A. (2014). Why Baryons Matter: The Kinematics of Dwarf Spheroidal Satellites. *ApJ*, 786:87.
- Bullock, J. S., Kravtsov, A. V., and Weinberg, D. H. (2000). Reionization and the Abundance of Galactic Satellites. *ApJ*, 539:517–521.
- Carlesi, E., Knebe, A., Lewis, G. F., Wales, S., and Yepes, G. (2014). Hydrodynamical simulations of coupled and uncoupled quintessence models - I. Halo properties and the cosmic web. *MNRAS*, 439:2943–2957.

- 
- Casarini, L., Bonometto, S. A., Borgani, S., Dolag, K., Murante, G., Mezzetti, M., Tornatore, L., and La Vacca, G. (2012). Tomographic weak-lensing shear spectra from large N-body and hydrodynamical simulations. *Astronomy and Astrophysics*, 542:A126.
- Casarini, L., La Vacca, G., Amendola, L., Bonometto, S. A., and Macciò, A. V. (2011a). Non-linear weak lensing forecasts. *Journal of Cosmology and Astroparticle Physics*, 3:26.
- Casarini, L., Macciò, A. V., and Bonometto, S. A. (2009a). Dynamical dark energy simulations: high accuracy power spectra at high redshift. *Journal of Cosmology and Astroparticle Physics*, 3:14.
- Casarini, L., Macciò, A. V., and Bonometto, S. A. (2009b). Dynamical dark energy simulations: high accuracy power spectra at high redshift. *Journal of Cosmology and Astroparticle Physics*, 3:14.
- Casarini, L., Macciò, A. V., Bonometto, S. A., and Stinson, G. S. (2011b). High-accuracy power spectra including baryonic physics in dynamical Dark Energy models. *MNRAS*, 412:911–920.
- Casarini, L., Macciò, A. V., Bonometto, S. A., and Stinson, G. S. (2011c). High-accuracy power spectra including baryonic physics in dynamical Dark Energy models. *MNRAS*, 412:911–920.
- Cen, R. (1992). A hydrodynamic approach to cosmology - Methodology. *ApJS*, 78:341–364.
- Chevallier, M. and Polarski, D. (2001). Accelerating Universes with Scaling Dark Matter. *International Journal of Modern Physics D*, 10:213–223.
- Coles, P. and Lucchin, F. (2002). *Cosmology*. Wiley, Second edition.
- Croton, D. J., Springel, V., White, S. D. M., De Lucia, G., Frenk, C. S., Gao, L., Jenkins, A., Kauffmann, G., Navarro, J. F., and Yoshida, N. (2006). The many lives of active galactic nuclei: cooling flows, black holes and the luminosities and colours of galaxies. *MNRAS*, 365:11–28.
- de Blok, W. J. G., Walter, F., Brinks, E., Trachternach, C., Oh, S.-H., and Kennicutt, Jr., R. C. (2008). High-Resolution Rotation Curves and Galaxy Mass Models from THINGS. *AJ*, 136:2648–2719.
- De Boni, C., Dolag, K., Ettori, S., Moscardini, L., Pettorino, V., and Baccigalupi, C. (2011). Hydrodynamical simulations of galaxy clusters in dark energy cosmologies - I. General properties. *MNRAS*, 415:2758–2772.
- Dekel, A. and Silk, J. (1986). The origin of dwarf galaxies, cold dark matter, and biased galaxy formation. *ApJ*, 303:39–55.

- Di Cintio, A., Brook, C. B., Macciò, A. V., Stinson, G. S., Knebe, A., Dutton, A. A., and Wadsley, J. (2014). The dependence of dark matter profiles on the stellar-to-halo mass ratio: a prediction for cusps versus cores. *MNRAS*, 437:415–423.
- Di Matteo, T., Springel, V., and Hernquist, L. (2005). Energy input from quasars regulates the growth and activity of black holes and their host galaxies. *Nature*, 433:604–607.
- Diemand, J., Zemp, M., Moore, B., Stadel, J., and Carollo, C. M. (2005). Cusps in cold dark matter haloes. *MNRAS*, 364:665–673.
- Dolag, K., Bartelmann, M., Perrotta, F., Baccigalupi, C., Moscardini, L., Meneghetti, M., and Tormen, G. (2004). Numerical study of halo concentrations in dark-energy cosmologies. *Astronomy and Astrophysics*, 416:853–864.
- Doroshkevich, A. G., Kotok, E. V., Poliudov, A. N., Shandarin, S. F., Sigov, I. S., and Novikov, I. D. (1980). Two-dimensional simulation of the gravitational system dynamics and formation of the large-scale structure of the universe. *MNRAS*, 192:321–337.
- Dutton, A. A. and Macciò, A. V. (2014). Cold dark matter haloes in the Planck era: evolution of structural parameters for Einasto and NFW profiles. *MNRAS*, 441:3359–3374.
- Einstein, A. (1917). Kosmologische Betrachtungen zur allgemeinen Relativitätstheorie. *Sitzungsberichte der Königlich Preussischen Akademie der Wissenschaften (Berlin)*, Seite 142-152., pages 142–152.
- Fedeli, C., Dolag, K., and Moscardini, L. (2012). Matter power spectra in dynamical dark energy cosmologies. *MNRAS*, 419:1588–1602.
- Ferreira, P. G. and Joyce, M. (1998). Cosmology with a primordial scaling field. *Phys. Rev. D*, 58(2):023503.
- Flores, R. A. and Primack, J. R. (1994). Observational and theoretical constraints on singular dark matter halos. *ApJ*, 427:L1–L4.
- Fontanot, F., Puchwein, E., Springel, V., and Bianchi, D. (2013). Semi-analytic galaxy formation in  $f(R)$ -gravity cosmologies. *ArXiv e-prints*.
- Fontanot, F., Springel, V., Angulo, R. E., and Henriques, B. (2012). Semi-analytic galaxy formation in early dark energy cosmologies. *MNRAS*, 426:2335–2341.
- Francis, M. J., Lewis, G. F., and Linder, E. V. (2009). Halo mass functions in early dark energy cosmologies. *MNRAS*, 393:L31–L35.

- 
- Friedmann, A. (1922). Über die Krümmung des Raumes. *Zeitschrift für Physik*, 10:377–386.
- Gallagher, III, J. S., Hunter, D. A., and Tutukov, A. V. (1984). Star formation histories of irregular galaxies. *ApJ*, 284:544–556.
- Gamow, G. (1946). Expanding Universe and the Origin of Elements. *Physical Review*, 70:572–573.
- Gentile, G., Famaey, B., Zhao, H., and Salucci, P. (2009). Universality of galactic surface densities within one dark halo scale-length. *Nature*, 461:627–628.
- Gingold, R. A. and Monaghan, J. J. (1977). Smoothed particle hydrodynamics - Theory and application to non-spherical stars. *MNRAS*, 181:375–389.
- Gould, H., Tobochnik, J., and Harrison, D. E. (1988). An Introduction to Computer Simulation Methods: Applications to Physical Systems, Part 1 and Part 2. *Computers in Physics*, 2:90.
- Governato, F., Brook, C., Mayer, L., Brooks, A., Rhee, G., Wadsley, J., Jonsson, P., Willman, B., Stinson, G., Quinn, T., and Madau, P. (2010). Bulgeless dwarf galaxies and dark matter cores from supernova-driven outflows. *Nature*, 463:203–206.
- Governato, F., Willman, B., Mayer, L., Brooks, A., Stinson, G., Valenzuela, O., Wadsley, J., and Quinn, T. (2007). Forming disc galaxies in  $\Lambda$ CDM simulations. *MNRAS*, 374:1479–1494.
- Governato, F., Zolotov, A., Pontzen, A., Christensen, C., Oh, S. H., Brooks, A. M., Quinn, T., Shen, S., and Wadsley, J. (2012). Cuspy no more: how outflows affect the central dark matter and baryon distribution in  $\Lambda$  cold dark matter galaxies. *MNRAS*, 422:1231–1240.
- Grossi, M. and Springel, V. (2009). The impact of early dark energy on non-linear structure formation. *MNRAS*, 394:1559–1574.
- Guedes, J., Callegari, S., Madau, P., and Mayer, L. (2011). Forming Realistic Late-type Spirals in a  $\Lambda$ CDM Universe: The Eris Simulation. *ApJ*, 742:76.
- Guo, Z.-K., Ohta, N., and Tsujikawa, S. (2007). Probing the coupling between dark components of the universe. *Phys. Rev. D*, 76(2):023508.
- Hernquist, L. and Katz, N. (1989). TREE SPH - A unification of SPH with the hierarchical tree method. *ApJS*, 70:419–446.
- Hubble, E. (1929). A Relation between Distance and Radial Velocity among Extra-Galactic Nebulae. *Proceedings of the National Academy of Science*, 15:168–173.

- Jeans, J. H. (1902). The Stability of a Spherical Nebula. *Royal Society of London Philosophical Transactions Series A*, 199:1–53.
- Jenkins, A., Frenk, C. S., White, S. D. M., Colberg, J. M., Cole, S., Evrard, A. E., Couchman, H. M. P., and Yoshida, N. (2001). The mass function of dark matter haloes. *MNRAS*, 321:372–384.
- Jing, Y. P., Zhang, P., Lin, W. P., Gao, L., and Springel, V. (2006). The Influence of Baryons on the Clustering of Matter and Weak-Lensing Surveys. *ApJ*, 640:L119–L122.
- Jones, D. H., Read, M. A., Saunders, W., Colless, M., Jarrett, T., Parker, Q. A., Fairall, A. P., Mauch, T., Sadler, E. M., Watson, F. G., Burton, D., Campbell, L. A., Cass, P., Croom, S. M., Dawe, J., Fiegert, K., Frankcombe, L., Hartley, M., Huchra, J., James, D., Kirby, E., Lahav, O., Lucey, J., Mamon, G. A., Moore, L., Peterson, B. A., Prior, S., Proust, D., Russell, K., Safouris, V., Wakamatsu, K.-I., Westra, E., and Williams, M. (2009). The 6dF Galaxy Survey: final redshift release (DR3) and southern large-scale structures. *MNRAS*, 399:683–698.
- Kajisawa, M., Ichikawa, T., Yamada, T., Uchimoto, Y. K., Yoshikawa, T., Akiyama, M., and Onodera, M. (2010). MOIRCS Deep Survey. VIII. Evolution of Star Formation Activity as a Function of Stellar Mass in Galaxies Since  $z = 3$ . *ApJ*, 723:129–145.
- Kannan, R., Stinson, G. S., Macciò, A. V., Brook, C., Weinmann, S. M., Wadsley, J., and Couchman, H. M. P. (2014). The MaGICC volume: reproducing statistical properties of high-redshift galaxies. *MNRAS*, 437:3529–3539.
- Karim, A., Schinnerer, E., Martínez-Sansigre, A., Sargent, M. T., van der Wel, A., Rix, H.-W., Ilbert, O., Smolčić, V., Carilli, C., Pannella, M., Koekemoer, A. M., Bell, E. F., and Salvato, M. (2011). The Star Formation History of Mass-selected Galaxies in the COSMOS Field. *ApJ*, 730:61.
- Kennedy, R., Frenk, C., Cole, S., and Benson, A. (2014). Constraining the warm dark matter particle mass with Milky Way satellites. *MNRAS*, 442:2487–2495.
- Kennicutt, Jr., R. C. (1998). The Global Schmidt Law in Star-forming Galaxies. *ApJ*, 498:541–552.
- Klypin, A. (2000). Numerical Simulations in Cosmology I: Methods. *ArXiv Astrophysics e-prints*.
- Klypin, A., Kravtsov, A. V., Valenzuela, O., and Prada, F. (1999). Where Are the Missing Galactic Satellites? *ApJ*, 522:82–92.

- 
- Klypin, A., Macciò, A. V., Mainini, R., and Bonometto, S. A. (2003). Halo Properties in Models with Dynamical Dark Energy. *ApJ*, 599:31–37.
- Knollmann, S. R. and Knebe, A. (2009). AHF: Amiga’s Halo Finder. *ApJS*, 182:608–624.
- Koivisto, T. (2005). Growth of perturbations in dark matter coupled with quintessence. *Phys. Rev. D*, 72(4):043516.
- Komatsu, E., Smith, K. M., Dunkley, J., Bennett, C. L., Gold, B., Hinshaw, G., Jarosik, N., Larson, D., Nolte, M. R., Page, L., Spergel, D. N., Halpern, M., Hill, R. S., Kogut, A., Limon, M., Meyer, S. S., Odegard, N., Tucker, G. S., Weiland, J. L., Wollack, E., and Wright, E. L. (2011). Seven-year Wilkinson Microwave Anisotropy Probe (WMAP) Observations: Cosmological Interpretation. *ApJS*, 192:18.
- Krumholz, M. R. and Tan, J. C. (2007). Slow Star Formation in Dense Gas: Evidence and Implications. *ApJ*, 654:304–315.
- Kuhlen, M., Strigari, L. E., Zentner, A. R., Bullock, J. S., and Primack, J. R. (2005). Dark energy and dark matter haloes. *MNRAS*, 357:387–400.
- Kuzio de Naray, R., McGaugh, S. S., and de Blok, W. J. G. (2008). Mass Models for Low Surface Brightness Galaxies with High-Resolution Optical Velocity Fields. *ApJ*, 676:920–943.
- La Vacca, G., Kristiansen, J. R., Colombo, L. P. L., Mainini, R., and Bonometto, S. A. (2009). Do WMAP data favor neutrino mass and a coupling between Cold Dark Matter and Dark Energy? *JCAP*, 0904:007.
- Lacey, C. and Cole, S. (1993). Merger rates in hierarchical models of galaxy formation. *MNRAS*, 262:627–649.
- Landau, L. D. and Lifshitz, E. M. (1976). *The Classical Theory of Fields.*, volume 1. Butterworth-Heinemann, Third edition.
- Larson, R. B. (1974). Effects of supernovae on the early evolution of galaxies. *MNRAS*, 169:229–246.
- Lemaître, G. (1927). Un Univers homogène de masse constante et de rayon croissant rendant compte de la vitesse radiale des nébuleuses extragalactiques. *Annales de la Société Scientifique de Bruxelles*, 47:49–59.
- Lewis, A. and Bridle, S. (2002). Cosmological parameters from CMB and other data: a Monte- Carlo approach. *Phys. Rev.*, D66:103511.
- Li, B. and Barrow, J. D. (2011). N-Body Simulations for Coupled Scalar Field Cosmology. *Phys. Rev.*, D83:024007.

- Li, B., Zhao, G.-B., Teyssier, R., and Koyama, K. (2012). ECOSMOG: an Efficient COde for Simulating MOdified Gravity. *Journal of Cosmology and Astroparticle Physics*, 1:51.
- Linde, A. (1987). *Inflation and quantum cosmology.*, pages 604–630.
- Linder, E. V. (2003). Exploring the Expansion History of the Universe. *Physical Review Letters*, 90(9):091301.
- Linder, E. V. and Jenkins, A. (2003). Cosmic structure growth and dark energy. *MNRAS*, 346:573–583.
- Lovell, M. R., Eke, V., Frenk, C. S., Gao, L., Jenkins, A., Theuns, T., Wang, J., White, S. D. M., Boyarsky, A., and Ruchayskiy, O. (2012). The haloes of bright satellite galaxies in a warm dark matter universe. *MNRAS*, 420:2318–2324.
- Lucy, L. B. (1977). A numerical approach to the testing of the fission hypothesis. *AJ*, 82:1013–1024.
- Ludlow, A. D., Navarro, J. F., Boylan-Kolchin, M., Bett, P. E., Angulo, R. E., Li, M., White, S. D. M., Frenk, C., and Springel, V. (2013). The mass profile and accretion history of cold dark matter haloes. *MNRAS*, 432:1103–1113.
- Macciò, A. V. (2004). *Non-linear features in dynamical and coupled dark energy models*. PhD thesis, University of Milano Bicocca.
- Macciò, A. V., Dutton, A. A., and van den Bosch, F. C. (2008). Concentration, spin and shape of dark matter haloes as a function of the cosmological model: WMAP1, WMAP3 and WMAP5 results. *MNRAS*, 391:1940–1954.
- Macciò, A. V., Kang, X., Fontanot, F., Somerville, R. S., Koposov, S., and Monaco, P. (2010). Luminosity function and radial distribution of Milky Way satellites in a  $\Lambda$ CDM Universe. *MNRAS*, 402:1995–2008.
- Macciò, A. V., Mainini, R., Penzo, C., and Bonometto, S. A. (2015). Strongly Coupled Dark Energy Cosmologies: preserving  $\Lambda$ CDM success and easing low scale problems II - Cosmological simulations. *ArXiv e-prints*.
- Macciò, A. V., Quercellini, C., Mainini, R., Amendola, L., and Bonometto, S. A. (2004). Coupled dark energy: Parameter constraints from N-body simulations. *Phys. Rev. D*, 69(12):123516.
- Macciò, A. V., Stinson, G., Brook, C. B., Wadsley, J., Couchman, H. M. P., Shen, S., Gibson, B. K., and Quinn, T. (2012). Halo Expansion in Cosmological Hydro Simulations: Toward a Baryonic Solution of the Cusp/Core Problem in Massive Spirals. *ApJ*, 744:L9.

- 
- Madau, P., Diemand, J., and Kuhlen, M. (2008). Dark Matter Subhalos and the Dwarf Satellites of the Milky Way. *ApJ*, 679:1260–1271.
- Maio, U., Dolag, K., Meneghetti, M., Moscardini, L., Yoshida, N., Baccigalupi, C., Bartelmann, M., and Perrotta, F. (2006). Early structure formation in quintessence models and its implications for cosmic reionization from first stars. *MNRAS*, 373:869–878.
- Mangano, G., Miele, G., and Pettorino, V. (2003). Coupled Quintessence and the Coincidence Problem. *Modern Physics Letters A*, 18:831–842.
- Marinacci, F., Pakmor, R., and Springel, V. (2013). The formation of disc galaxies in high resolution moving-mesh cosmological simulations. *ArXiv e-prints*.
- Matarrese, S., Pietroni, M., and Schimd, C. (2003). Non-linear gravitational clustering in scalar field cosmologies. *Journal of Cosmology and Astroparticle Physics*, 8:5.
- McKee, C. F. and Ostriker, J. P. (1977). A theory of the interstellar medium - Three components regulated by supernova explosions in an inhomogeneous substrate. *ApJ*, 218:148–169.
- Monaghan, J. J. (1992). Smoothed particle hydrodynamics. *ARA&A*, 30:543–574.
- Moore, B. (1994). Evidence against dissipation-less dark matter from observations of galaxy haloes. *Nature*, 370:629–631.
- Moore, B., Ghigna, S., Governato, F., Lake, G., Quinn, T., Stadel, J., and Tozzi, P. (1999). Dark Matter Substructure within Galactic Halos. *ApJ*, 524:L19–L22.
- Moore, B., Kazantzidis, S., Diemand, J., and Stadel, J. (2004). The origin and tidal evolution of cuspy triaxial haloes. *MNRAS*, 354:522–528.
- Moster, B. P., Naab, T., and White, S. D. M. (2013). Galactic star formation and accretion histories from matching galaxies to dark matter haloes. *MNRAS*, 428:3121–3138.
- Moster, B. P., Somerville, R. S., Maulbetsch, C., van den Bosch, F. C., Macciò, A. V., Naab, T., and Oser, L. (2010). Constraints on the Relationship between Stellar Mass and Halo Mass at Low and High Redshift. *ApJ*, 710:903–923.
- Mukhanov, V. (2005). *Physical Foundations of Cosmology*. Cambridge University Press.

- 
- Navarro, J. F., Eke, V. R., and Frenk, C. S. (1996). The cores of dwarf galaxy haloes. *MNRAS*, 283:L72–L78.
- Navarro, J. F., Frenk, C. S., and White, S. D. M. (1995). Simulations of X-ray clusters. *MNRAS*, 275:720–740.
- Navarro, J. F., Frenk, C. S., and White, S. D. M. (1997). A Universal Density Profile from Hierarchical Clustering. *ApJ*, 490:493.
- Oñorbe, J., Boylan-Kolchin, M., Bullock, J. S., Hopkins, P. F., Kerës, D., Faucher-Giguère, C.-A., Quataert, E., and Murray, N. (2015). Forged in FIRE: cusps, cores, and baryons in low-mass dwarf galaxies. *ArXiv e-prints*.
- Pace, F., Fedeli, C., Moscardini, L., and Bartelmann, M. (2012). Structure formation in cosmologies with oscillating dark energy. *MNRAS*, 422:1186–1202.
- Penzias, A. A. and Wilson, R. W. (1965). A Measurement of Excess Antenna Temperature at 4080 Mc/s. *ApJ*, 142:419–421.
- Penzo, C., Macciò, A. V., Baldi, M., Casarini, L., and Oñorbe, J. (2015). Effects of Coupled Dark Energy on the Milky Way and its Satellites. *ArXiv e-prints*.
- Penzo, C., Macciò, A. V., Casarini, L., Stinson, G. S., and Wadsley, J. (2014). Dark MaGICC: the effect of dark energy on disc galaxy formation. Cosmology does matter. *MNRAS*, 442:176–186.
- Perlmutter, S., Aldering, G., Goldhaber, G., Knop, R. A., Nugent, P., Castro, P. G., Deustua, S., Fabbro, S., Goobar, A., Groom, D. E., Hook, I. M., Kim, A. G., Kim, M. Y., Lee, J. C., Nunes, N. J., Pain, R., Pennypacker, C. R., Quimby, R., Lidman, C., Ellis, R. S., Irwin, M., McMahon, R. G., Ruiz-Lapuente, P., Walton, N., Schaefer, B., Boyle, B. J., Filippenko, A. V., Matheson, T., Fruchter, A. S., Panagia, N., Newberg, H. J. M., Couch, W. J., and The Supernova Cosmology Project (1999). Measurements of Omega and Lambda from 42 High-Redshift Supernovae. *ApJ*, 517:565–586.
- Pettorino, V., Amendola, L., Baccigalupi, C., and Quercellini, C. (2012). Constraints on coupled dark energy using CMB data from WMAP and South Pole Telescope. *Phys. Rev. D*, 86(10):103507.
- Pettorino, V. and Baccigalupi, C. (2008). Coupled and extended quintessence: Theoretical differences and structure formation. *Phys. Rev. D*, 77(10):103003.

- 
- Planck Collaboration, Ade, P. A. R., Aghanim, N., Arnaud, M., Ashdown, M., Aumont, J., Baccigalupi, C., Banday, A. J., Barreiro, R. B., Bartlett, J. G., and et al. (2015). Planck 2015 results. XIII. Cosmological parameters. *ArXiv e-prints*.
- Pontzen, A. and Governato, F. (2012). How supernova feedback turns dark matter cusps into cores. *MNRAS*, 421:3464–3471.
- Press, W. H. and Schechter, P. (1974). Formation of Galaxies and Clusters of Galaxies by Self-Similar Gravitational Condensation. *ApJ*, 187:425–438.
- Puchwein, E., Bartelmann, M., Dolag, K., and Meneghetti, M. (2005). The impact of gas physics on strong cluster lensing. *Astronomy and Astrophysics*, 442:405–412.
- Purcell, C. W. and Zentner, A. R. (2012). Bailing out the Milky Way: variation in the properties of massive dwarfs among galaxy-sized systems. *Journal of Cosmology and Astroparticle Physics*, 12:7.
- Raiteri, C. M., Villata, M., and Navarro, J. F. (1996). Simulations of Galactic chemical evolution. I. O and Fe abundances in a simple collapse model. *A&A*, 315:105–115.
- Rashkov, V., Madau, P., Kuhlen, M., and Diemand, J. (2012). On the Assembly of the Milky Way Dwarf Satellites and Their Common Mass Scale. *ApJ*, 745:142.
- Ratra, B. and Peebles, P. J. E. (1988). Cosmological consequences of a rolling homogeneous scalar field. *Phys. Rev. D*, 37:3406–3427.
- Rees, M. J. and Ostriker, J. P. (1977). Cooling, dynamics and fragmentation of massive gas clouds - Clues to the masses and radii of galaxies and clusters. *MNRAS*, 179:541–559.
- Riess, A. G., Filippenko, A. V., Challis, P., Clocchiatti, A., Diercks, A., Garnavich, P. M., Gilliland, R. L., Hogan, C. J., Jha, S., Kirshner, R. P., Leibundgut, B., Phillips, M. M., Reiss, D., Schmidt, B. P., Schommer, R. A., Smith, R. C., Spyromilio, J., Stubbs, C., Suntzeff, N. B., and Tonry, J. (1998). Observational Evidence from Supernovae for an Accelerating Universe and a Cosmological Constant. *The Astronomical Journal*, 116:1009–1038.
- Riotto, A. (2010). Particle cosmology. *ArXiv e-prints*.
- Robertson, B., Bullock, J. S., Cox, T. J., Di Matteo, T., Hernquist, L., Springel, V., and Yoshida, N. (2006). A Merger-driven Scenario for Cosmological Disk Galaxy Formation. *ApJ*, 645:986–1000.

- Robertson, H. P. (1935). Kinematics and World-Structure. *ApJ*, 82:284.
- Roll, P. G. and Wilkinson, D. T. (1966). Cosmic Background Radiation at 3.2 cm-Support for Cosmic Black-Body Radiation. *Physical Review Letters*, 16:405–407.
- Rubin, V. C., Peterson, C. J., and Ford, Jr., W. K. (1980). Rotation and mass of the inner 5 kiloparsecs of the S0 galaxy NGC 3115. *ApJ*, 239:50–53.
- Rudd, D. H., Zentner, A. R., and Kravtsov, A. V. (2008). Effects of Baryons and Dissipation on the Matter Power Spectrum. *ApJ*, 672:19–32.
- Salucci, P., Wilkinson, M. I., Walker, M. G., Gilmore, G. F., Grebel, E. K., Koch, A., Frigerio Martins, C., and Wyse, R. F. G. (2012). Dwarf spheroidal galaxy kinematics and spiral galaxy scaling laws. *MNRAS*, 420:2034–2041.
- Santini, P., Fontana, A., Grazian, A., Salimbeni, S., Fontanot, F., Paris, D., Boutsia, K., Castellano, M., Fiore, F., Gallozzi, S., Giallongo, E., Koekemoer, A. M., Menci, N., Pentericci, L., and Somerville, R. S. (2012). The evolving slope of the stellar mass function at  $0.6 < z < 4.5$  from deep WFC3 data. *A&A*, 538:A33.
- Sawala, T., Frenk, C. S., Fattahi, A., Navarro, J. F., Bower, R. G., Crain, R. A., Dalla Vecchia, C., Furlong, M., Jenkins, A., McCarthy, I. G., Qu, Y., Schaller, M., Schaye, J., and Theuns, T. (2014a). Bent by baryons: the low mass galaxy-halo relation. *ArXiv e-prints*.
- Sawala, T., Frenk, C. S., Fattahi, A., Navarro, J. F., Theuns, T., Bower, R. G., Crain, R. A., Furlong, M., Jenkins, A., Schaller, M., and Schaye, J. (2014b). The chosen few: the low mass halos that host faint galaxies. *ArXiv e-prints*.
- Scannapieco, C., Wadepuhl, M., Parry, O. H., Navarro, J. F., Jenkins, A., Springel, V., Teyssier, R., Carlson, E., Couchman, H. M. P., Crain, R. A., Dalla Vecchia, C., Frenk, C. S., Kobayashi, C., Monaco, P., Murante, G., Okamoto, T., Quinn, T., Schaye, J., Stinson, G. S., Theuns, T., Wadsley, J., White, S. D. M., and Woods, R. (2012). The Aquila comparison project: the effects of feedback and numerical methods on simulations of galaxy formation. *MNRAS*, 423:1726–1749.
- Schmidt, M. (1959). The Rate of Star Formation. *ApJ*, 129:243.
- Shen, S., Wadsley, J., and Stinson, G. (2010). The enrichment of the intergalactic medium with adiabatic feedback - I. Metal cooling and metal diffusion. *MNRAS*, 407:1581–1596.

- 
- Sheth, R. K., Mo, H. J., and Tormen, G. (2001). Ellipsoidal collapse and an improved model for the number and spatial distribution of dark matter haloes. *MNRAS*, 323:1–12.
- Simon, J. D., Bolatto, A. D., Leroy, A., Blitz, L., and Gates, E. L. (2005). High-Resolution Measurements of the Halos of Four Dark Matter-Dominated Galaxies: Deviations from a Universal Density Profile. *ApJ*, 621:757–776.
- Springel, V. (2005). The cosmological simulation code GADGET-2. *MNRAS*, 364:1105–1134.
- Springel, V. (2010). Smoothed Particle Hydrodynamics in Astrophysics. *ARA&A*, 48:391–430.
- Springel, V., Frenk, C. S., and White, S. D. M. (2006). The large-scale structure of the Universe. *Nature*, 440:1137–1144.
- Springel, V. and Hernquist, L. (2002). Cosmological smoothed particle hydrodynamics simulations: the entropy equation. *MNRAS*, 333:649–664.
- Springel, V., White, S. D. M., Jenkins, A., Frenk, C. S., Yoshida, N., Gao, L., Navarro, J., Thacker, R., Croton, D., Helly, J., Peacock, J. A., Cole, S., Thomas, P., Couchman, H., Evrard, A., Colberg, J., and Pearce, F. (2005). Simulations of the formation, evolution and clustering of galaxies and quasars. *Nature*, 435:629–636.
- Stadel, J. G. (2001). *Cosmological N-body simulations and their analysis*. PhD thesis, University of Washington.
- Stinson, G., Seth, A., Katz, N., Wadsley, J., Governato, F., and Quinn, T. (2006). Star formation and feedback in smoothed particle hydrodynamic simulations - I. Isolated galaxies. *MNRAS*, 373:1074–1090.
- Stinson, G. S., Bovy, J., Rix, H.-W., Brook, C., Roškar, R., Dalcanton, J. J., Macciò, A. V., Wadsley, J., Couchman, H. M. P., and Quinn, T. R. (2013a). MaGICC thick disc - I. Comparing a simulated disc formed with stellar feedback to the Milky Way. *MNRAS*, 436:625–634.
- Stinson, G. S., Brook, C., Macciò, A. V., Wadsley, J., Quinn, T. R., and Couchman, H. M. P. (2013b). Making Galaxies In a Cosmological Context: the need for early stellar feedback. *MNRAS*, 428:129–140.
- Stinson, G. S., Brook, C., Prochaska, J. X., Hennawi, J., Shen, S., Wadsley, J., Pontzen, A., Couchman, H. M. P., Quinn, T., Macciò, A. V., and Gibson, B. K. (2012). MAGICC haloes: confronting simulations with observations of the circumgalactic medium at  $z=0$ . *MNRAS*, 425:1270–1277.

- Stone, J. M. and Norman, M. L. (1992). ZEUS-2D: A radiation magnetohydrodynamics code for astrophysical flows in two space dimensions. I - The hydrodynamic algorithms and tests. *ApJS*, 80:753–790.
- Swaters, R. A., Madore, B. F., van den Bosch, F. C., and Balcells, M. (2003). The Central Mass Distribution in Dwarf and Low Surface Brightness Galaxies. *ApJ*, 583:732–751.
- Tegmark, M., Eisenstein, D. J., Strauss, M. A., Weinberg, D. H., Blanton, M. R., Frieman, J. A., Fukugita, M., Gunn, J. E., Hamilton, A. J. S., Knapp, G. R., Nichol, R. C., Ostriker, J. P., Padmanabhan, N., Percival, W. J., Schlegel, D. J., Schneider, D. P., Scoccimarro, R., Seljak, U., Seo, H.-J., Swanson, M., Szalay, A. S., Vogeley, M. S., Yoo, J., Zehavi, I., Abazajian, K., Anderson, S. F., Annis, J., Bahcall, N. A., Bassett, B., Berlind, A., Brinkmann, J., Budavari, T., Castander, F., Connolly, A., Csabai, I., Doi, M., Finkbeiner, D. P., Gillespie, B., Glazebrook, K., Hennessy, G. S., Hogg, D. W., Ivezić, Ž., Jain, B., Johnston, D., Kent, S., Lamb, D. Q., Lee, B. C., Lin, H., Loveday, J., Lupton, R. H., Munn, J. A., Pan, K., Park, C., Peoples, J., Pier, J. R., Pope, A., Richmond, M., Rockosi, C., Scranton, R., Sheth, R. K., Stebbins, A., Stoughton, C., Szapudi, I., Tucker, D. L., vanden Berk, D. E., Yanny, B., and York, D. G. (2006). Cosmological constraints from the SDSS luminous red galaxies. *Phys. Rev. D*, 74(12):123507.
- Teyssier, R. (2002). Cosmological hydrodynamics with adaptive mesh refinement. A new high resolution code called RAMSES. *A&A*, 385:337–364.
- Thielemann, F.-K., Nomoto, K., and Yokoi, K. (1986). Explosive nucleosynthesis in carbon deflagration models of Type I supernovae. *A&A*, 158:17–33.
- Tollerud, E. J., Beaton, R. L., Geha, M., Guhathakurta, P., Bullock, J. S., Kalirai, J. S., Kirby, E. N., and Boylan-Kolchin, M. (2012). Kinematics Of M31 dSphs And Implications For LCDM. In *American Astronomical Society Meeting Abstracts 219*, volume 219 of *American Astronomical Society Meeting Abstracts*, page 201.04.
- Toomre, A. and Toomre, J. (1972). Galactic Bridges and Tails. *ApJ*, 178:623–666.
- Trujillo-Gomez, S., Klypin, A., Colín, P., Ceverino, D., Arraki, K. S., and Primack, J. (2015). Low-mass galaxy assembly in simulations: regulation of early star formation by radiation from massive stars. *MNRAS*, 446:1140–1162.

- van Daalen, M. P., Schaye, J., Booth, C. M., and Dalla Vecchia, C. (2011). The effects of galaxy formation on the matter power spectrum: a challenge for precision cosmology. *MNRAS*, 415:3649–3665.
- van den Bosch, F. C. and Swaters, R. A. (2001). Dwarf galaxy rotation curves and the core problem of dark matter haloes. *MNRAS*, 325:1017–1038.
- Vera-Ciro, C. A., Helmi, A., Starkeburg, E., and Breddels, M. A. (2013). Not too big, not too small: the dark haloes of the dwarf spheroidals in the Milky Way. *MNRAS*, 428:1696–1703.
- Vogelsberger, M., Zavala, J., and Loeb, A. (2012). Subhaloes in self-interacting galactic dark matter haloes. *MNRAS*, 423:3740–3752.
- Wadsley, J. W., Stadel, J., and Quinn, T. (2004). Gasoline: a flexible, parallel implementation of TreeSPH. *New Astronomy*, 9:137–158.
- Walker, M. G. and Peñarrubia, J. (2011). A Method for Measuring (Slopes of) the Mass Profiles of Dwarf Spheroidal Galaxies. *ApJ*, 742:20.
- Wang, L., Dutton, A. A., Stinson, G. S., Macciò, A. V., Penzo, C., Kang, X., Keller, B. W., and Wadsley, J. (2015). NIHAO project I: Reproducing the inefficiency of galaxy formation across cosmic time with a large sample of cosmological hydrodynamical simulations. *ArXiv e-prints*.
- Wechsler, R. H., Bullock, J. S., Primack, J. R., Kravtsov, A. V., and Dekel, A. (2002). Concentrations of Dark Halos from Their Assembly Histories. *ApJ*, 568:52–70.
- Weinberg, S. (1989). The cosmological constant problem. *Reviews of Modern Physics*, 61:1–23.
- Wetterich, C. (1988). Cosmology and the fate of dilatation symmetry. *Nuclear Physics B*, 302:668–696.
- White, S. D. M. (1976). The dynamics of rich clusters of galaxies. *MNRAS*, 177:717–733.
- Wolf, J., Martinez, G. D., Bullock, J. S., Kaplinghat, M., Geha, M., Muñoz, R. R., Simon, J. D., and Avedo, F. F. (2010). Accurate masses for dispersion-supported galaxies. *MNRAS*, 406:1220–1237.
- Zel’dovich, Y. B. (1970). Gravitational instability: An approximate theory for large density perturbations. *A&A*, 5:84–89.
- Zhan, H. and Knox, L. (2004). Effect of Hot Baryons on the Weak-Lensing Shear Power Spectrum. *ApJ*, 616:L75–L78.
- Zwicky, F. (1933). Die Rotverschiebung von extragalaktischen Nebeln. *Helvetica Physica Acta*, 6:110–127.

# Acknowledgements

I would like to thank my supervisor Andrea Macciò for his advices and guidance that made this work possible. Despite his numerous students, he has always been patient and understanding and found time to help and answer all my questions. Thank you for giving me the chance to see what “science” is really like and also for trying to find solutions where there seemed to be none.

Additionally, I would like to thank the collaborators that have significantly contributed to this work, Marco Baldi, Luciano Casarini and Greg Stinson. Each of them have spent time explaining and clarifying and had useful suggestions and comments.

I am thankful to Andrea Macciò and Björn Schäfer for agreeing to referee my thesis and also to Luca Amendola and Henrik Beuther for being part of my thesis committee.

An heart-felt thank you to Christian Fendt, the coordinator of the IMPRS program. He has been there for me in moments of need, helped to find solutions and always gives caring advices.

I would like to thank my master thesis supervisor, Lauro Moscardini. If it had not been for you, I would not even have applied for a Ph.D. position. Thank you for making me rediscover my interest for cosmology and for smiling when I would show up with colorful hair and a longboard.

In particular, I would like to add that, despite this field often being a cradle for heteronormativity, no one has ever made me regret being open and being myself. I greatly appreciated your open-mindedness, every single bit.

I would also like to thank all friends who helped to make of Heidelberg a welcoming place where I could spend most of the last three years. It has been a pleasure to share laughs and down moments, to share the office, lunches and the numerous falafel.

An enormous thank you to my parents, who have always supported me in all my decisions and who keep doing it today. Thank you for having been able to find an impressive combination of being there for me and giving me space to make my own choices and mistakes. *I Roberti* are the strongest pillar I have, one that I can lean against. *Un enorme grazie ai miei genitori, che mi hanno sempre appoggiato in tutte le mie scelte e che continuano a farlo ancora oggi. Grazie per essere stati in grado di trovare un'eccezionale combinazione tra il darmi supporto e lasciarmi lo spazio per fare scelte ed errori. I Roberti sono la colonna portante su cui so di potermi appoggiare.*

Finally, I would like to deeply thank Xenia for all she has done for me. I thank you with all my love for having stood by me during the ups and downs of these last two years. Thank you for being my better half.

*I'm in love with your brother  
What's his name?  
I thought I'd come by  
to see him again  
when you two dance  
oh, what a dance  
when you two laughed  
oh, what a laugh  
[...]*

*Pass This On, The Knife*